

## **Master thesis : Experimental and numerical analysis of the aerodynamics of the A&M Shell Eco-marathon vehicle prototype**

**Auteur :** Calleja Vazquez, Juan Manuel

**Promoteur(s) :** Terrapon, Vincent

**Faculté :** Faculté des Sciences appliquées

**Diplôme :** Master en ingénieur civil en aérospatiale, à finalité spécialisée en "aerospace engineering"

**Année académique :** 2017-2018

**URI/URL :** <http://hdl.handle.net/2268.2/4671>

---

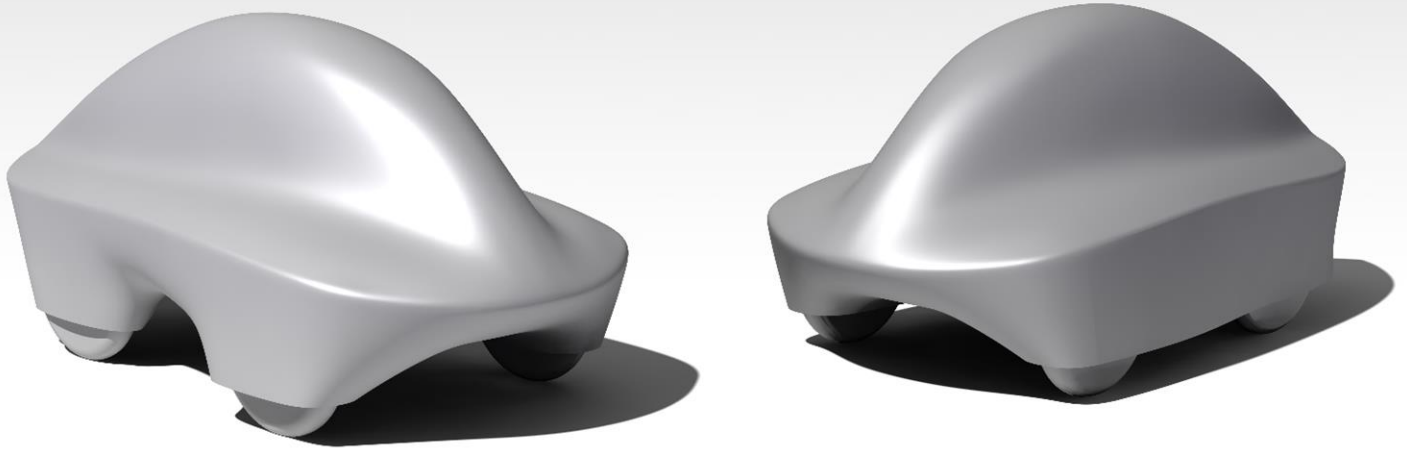
### *Avertissement à l'attention des usagers :*

*Tous les documents placés en accès ouvert sur le site le site MatheO sont protégés par le droit d'auteur. Conformément aux principes énoncés par la "Budapest Open Access Initiative"(BOAI, 2002), l'utilisateur du site peut lire, télécharger, copier, transmettre, imprimer, chercher ou faire un lien vers le texte intégral de ces documents, les disséquer pour les indexer, s'en servir de données pour un logiciel, ou s'en servir à toute autre fin légale (ou prévue par la réglementation relative au droit d'auteur). Toute utilisation du document à des fins commerciales est strictement interdite.*

*Par ailleurs, l'utilisateur s'engage à respecter les droits moraux de l'auteur, principalement le droit à l'intégrité de l'oeuvre et le droit de paternité et ce dans toute utilisation que l'utilisateur entreprend. Ainsi, à titre d'exemple, lorsqu'il reproduira un document par extrait ou dans son intégralité, l'utilisateur citera de manière complète les sources telles que mentionnées ci-dessus. Toute utilisation non explicitement autorisée ci-avant (telle que par exemple, la modification du document ou son résumé) nécessite l'autorisation préalable et expresse des auteurs ou de leurs ayants droit.*

---

# Experimental and numerical analysis of the aerodynamics of the A&M Shell Eco-marathon vehicle prototype



**Juan Manuel Calleja**

University of **Liège** - Faculty of Applied **Sciences**

Academic Year **2017-2018**

Graduation Studies conducted for obtaining the Master's degree in  
Aerospace Engineering **by Juan Manuel Calleja Vázquez**

# Contents

<b>1</b>	<b>Introduction</b>	<b>1</b>
<b>2</b>	<b>Methodology</b>	<b>8</b>
2.1	Numerical methodology . . . . .	8
2.1.1	Turbulence and transition models . . . . .	10
2.1.2	Boundary conditions . . . . .	14
2.1.3	Cell convergence study . . . . .	18
2.1.4	Domain convergence study . . . . .	20
2.1.5	Sensitivity study . . . . .	22
2.1.6	Solver set up . . . . .	23
2.1.7	Numerical validation: The Ahmed body . . . . .	27
2.2	Experimental methodology . . . . .	30
2.2.1	Wind tunnel facility and wind tunnel model . . . . .	30
2.2.2	Force test . . . . .	31
2.2.3	Pressure test . . . . .	39
<b>3</b>	<b>Experimental validation of numerical simulations</b>	<b>42</b>
3.1	Symmetry and steadiness verification . . . . .	42
3.2	Reynolds effect study . . . . .	45
3.2.1	Force coefficient comparison . . . . .	45
3.2.2	Pressure coefficient comparison . . . . .	53
3.2.3	Boundary layer effect . . . . .	64
3.3	Crosswind effect on Electra . . . . .	66
3.3.1	Force Tests . . . . .	67
3.3.2	Pressure Tests . . . . .	68
<b>4</b>	<b>Advanced aerodynamic studies of Electra</b>	<b>71</b>
4.1	Moving car aerodynamics . . . . .	71
4.1.1	Zero yaw angle . . . . .	71
4.1.2	Crosswind conditions . . . . .	79
4.2	Effect of simplifications and surface irregularities . . . . .	82
4.2.1	Wheel and well simplification . . . . .	82
4.2.2	Rear-view mirrors . . . . .	86

4.2.3	Surface imperfections . . . . .	88
<b>5</b>	<b>Aerodynamic modifications of the Electra</b>	<b>92</b>
5.1	Improving performance . . . . .	92
5.1.1	Height effect . . . . .	92
5.1.2	Shape modifications . . . . .	94
5.2	New concept . . . . .	100
<b>6</b>	<b>Conclusion</b>	<b>106</b>
6.1	Results and critical overview . . . . .	106
6.2	Future work . . . . .	108
6.2.1	Numerical simulations . . . . .	108
6.2.2	Experimental tests . . . . .	109
<b>Annex I:</b>	<b>Thesis workflow diagram</b>	<b>110</b>



# List of Figures

1.1	La Jamais Contente 1899. . . . .	2
1.2	Stanley Steamer Rocket 1906. . . . .	2
1.3	A.L.F.A. 40/60 HP Aerodinamica. . . . .	3
1.4	Rumpler Tropfenwagen. . . . .	3
1.5	Volkswagen Scirocco I. . . . .	3
1.6	Audi 100 III. . . . .	3
1.7	Mercedes CLA 180 BlueEFFICIENCY Edition. . . . .	4
1.8	Tesla Model S. . . . .	4
1.9	Electra participating at the 2015 Shell Eco Marathon Europe competition. . . . .	4
1.10	Catia CAD model used to perform the numerical simulations. . . . .	5
1.11	Detail of the wheel well simplification in the CAD model. . . . .	5
1.12	Graphical representation of the projection plane in which the frontal area of the car is calculated and definition of the axes of reference. . . . .	6
2.1	Subregions of the inner layer. . . . .	10
2.2	Frictional resistance in pipes. $Re_D$ is defined as the diameter based Reynolds number, and $\lambda$ is the frictional resistance . . . . .	13
2.3	Kinetic energy [J/Kg] over the airfoil at an angle of attack $\alpha = 0^\circ$ and a height equal to the airfoil chord with moving floor. Simulation performed using the $\gamma Re_\theta$ transition model. . . . .	14
2.4	Kinetic energy [J/Kg] over the airfoil at an angle of attack $\alpha = 0^\circ$ and a height equal to the airfoil chord with moving floor using the $k - \omega$ SST turbulence model. . . . .	14
2.5	Velocity profile detail for the still road condition. . . . .	15
2.6	Velocity profile detail for the rolling car condition. . . . .	15
2.7	Different named sections of computational domain. . . . .	16
2.8	Unstructured tetrahedral mesh. . . . .	17
2.9	Structured hexahedral mesh. . . . .	17
2.10	Inflation layer mesh detail with visualization of the boundary layer velocity profile ( $u(y)$ ). . . . .	18
2.11	Drag coefficient ( $c_D$ ) cell convergence study. . . . .	19
2.12	Lift coefficient ( $c_L$ ) cell convergence study. . . . .	19
2.13	Computational time per 100 iterations for different number of cells. . . . .	19

2.14	Computational fluid domain size. Domain mesh partitioning in black, refinement boxes in orange. . . . .	20
2.15	Blockage effect of the streamlines with walls surrounding the car. . . . .	21
2.16	Natural streamlines around the car in a non-restricted domain. . . . .	21
2.17	Half domain final mesh seen from the symmetry side. . . . .	22
2.18	Refinement box and Electra detail of the half domain final mesh seen from the symmetry side. . . . .	22
2.19	Detail of the inflation layer at the top surface of the Electra in half domain final mesh seen from the symmetry side. . . . .	22
2.20	Flowchart comparison of a coupled and a segregated pressure-based algorithm. . . . .	24
2.21	Largest local residual of the second order central finite difference discretized 1D Poisson equation with boundary conditions solved by using Gauss Seidel. . . . .	25
2.22	Comparison of two different spatial discretizations of a sinusoidal function and the value seen by by each discretization point. . . . .	26
2.23	Graphic representation of the multigrid V and W cycles. (Adapted from [1]) . . . . .	26
2.24	Graphic representation of the multigrid F cycle. . . . .	27
2.25	Geometry definition of the Ahmed Body. Dimensions in mm. . . . .	28
2.26	Experimental and numerical comparison of the Ahmed Body total and pressure drag using the $k - \epsilon$ realizable turbulent model with non-equilibrium wall function modelling. . . . .	28
2.27	Experimental and numerical comparison of the Ahmed Body total and pressure drag using the low Reynolds $\gamma Re_\theta$ transition model. . . . .	28
2.28	Streamlines and pressure contour plot of the Ahmed Body at 60 m/s and a slant angle of $\phi = 20^\circ$ . Numerical simulation performed with the $k - \epsilon$ realizable model with non equilibrium wall functions. . . . .	29
2.29	Detail of the wake horseshoe vortex and recirculation bubbles depicted by S.R. Ahmed et al. in their paper [2]. . . . .	29
2.30	ULiège's subsonic wind tunnel drawing for the used close loop configuration. (Adapted from [3]) . . . . .	30
2.31	Polyamide 3D printed scale model and the Electra car. . . . .	31
2.32	Schematic view of the initial wind tunnel set up. . . . .	32
2.33	Drag force measured by the ATI Omega 160 at 200 Hz with the initial wind tunnel set-up at 30 m/s and a yaw angle of $0^\circ$ . . . . .	33
2.34	Lift force measured by the ATI Omega 160 at 200 Hz with the initial wind tunnel set-up at 30 m/s and an angle of yaw of $0^\circ$ . . . . .	33
2.35	Graphic representation of the parasitic horizontal force that appears when decentralising the calibration mass. . . . .	34
2.36	Parasitic force appearing in the x axis as a function of the applied moment on the y axis. Test carried out by moving a calibration mass of 0.5 kg on the x axis. . . . .	35

2.37	Parasitic force appearing in the y axis as a function of the applied moment on the x axis. Test carried out by moving a calibration mass of 0.5 kg on the y axis. . . . .	35
2.38	Photo of the tuft visualization over the first wind tunnel set up at a speed of 20 m/s. Green squares mark stream-wise pointing tufts, while red circles highlight upstream facing tufts. . . . .	36
2.39	Schematic view of the recirculation bubble present at the first wind tunnel set up. . . . .	37
2.40	Graphic representation of the averaged and normalized velocity profiles obtained with the digital anemometer at a free stream velocity of 15, 20 and 25 m/s. . . . .	37
2.41	Comparison of the averaged and normalized velocity profiles at 25 cm from the car front for multiple heights and speeds. The first set-up measurements were carried out with a digital anemometer while the second set-up measurements were performed with a Cobra probe. . . . .	38
2.42	Turbulent intensity comparison at 25 cm from the car front for multiple heights and speeds. Measurements taken with a Cobra probe. . . . .	38
2.43	Schematic view of the initial wind tunnel set up. . . . .	39
2.44	Drawing of the upper side of the Electra with pressure taps position. . . . .	39
2.45	Drawing of the lower side of the Electra with pressure taps position. . . . .	39
2.46	Drawing of the left side of the Electra with pressure taps position. . . . .	40
2.47	Drawing of the right side of the Electra with pressure taps position. . . . .	40
2.48	Wind tunnel pressure test set-up. Model and tubing detail. . . . .	40
2.49	Wind tunnel pressure test set-up. Model, tubing and Pressure Sensor detail. . . . .	40
2.50	Wind tunnel pressure test set-up. Tubing exit detail. . . . .	41
2.51	Wind tunnel pressure test set-up. Model, tubing and pressure taps detail. . . . .	41
3.1	Drag and lift coefficients as a function of the number of iterations. Each 25 iterations represent a time step of 0.05 s. Simulation performed using full domain, URANS equations with a time step of 0.05 s and $\gamma Re_\theta$ model. . . . .	43
3.2	Single sided amplitude spectrum of the experimental $F_x(t)$ at multiple $Re_L$ . Measurements performed at 200 Hz. . . . .	44
3.3	Comparison of the single sided amplitude spectrum of the experimental $F_x(t)$ at $Re_L = 13 \times 10^5$ and wind-off results. Measurements performed at 200 Hz for the wind test and 1000 Hz for the wind-off test. Wind off amplitude multiplied by 15 for better comparison. . . . .	44
3.4	Drag coefficient at different length based Reynolds numbers obtained experimentally and with the wall function version of the $k - \varepsilon$ and $k - \omega$ SST models. . . . .	46
3.5	Lift coefficient at different length based Reynolds numbers obtained with the wall function version of the $k - \varepsilon$ and $k - \omega$ SST models. . . . .	46

3.6	Comparison of wind tunnel and numerical boundary layer at 0.5 car lengths in front of the car. Velocity normalized by dividing by the free-stream velocity and the height normalized in such a way that 1 represents the car height. . . . .	47
3.7	Velocity field contour plot at the symmetry plane of the car. Simulation performed with the wall function version of the $k - \omega$ SST model, still road conditions and a $Re_L = 13 \times 10^5$ . . . . .	48
3.8	Velocity field contour plot at the symmetry plane of the car. Simulation performed with the wall function version of the realizable $k - \varepsilon$ model, still road conditions and a $Re_L = 13 \times 10^5$ . . . . .	48
3.9	Drag coefficient at different length based Reynolds numbers obtained experimentally and with the low-Reynolds version of the $k - \omega$ SST model and the $\gamma Re_\theta$ transition model, still road conditions and a $Re_L = 13 \times 10^5$ . . . . .	49
3.10	Lift coefficient at different length based Reynolds numbers obtained with the low-Reynolds version of the $k - \omega$ SST model and the $\gamma Re_\theta$ transition model, still road conditions and a $Re_L = 13 \times 10^5$ . . . . .	49
3.11	Velocity field contour plot at the symmetry plane of the car. Simulation performed with the low Reynolds version of the $k - \omega$ SST model, still road conditions and a $Re_L = 13 \times 10^5$ . . . . .	50
3.12	Velocity field contour plot at the symmetry plane of the car. Simulation performed with the $\gamma Re_\theta$ transition model, still road conditions and a $Re_L = 13 \times 10^5$ . . . . .	50
3.13	Drag coefficient at different length based Reynolds numbers obtained experimentally and with the wall function and low-Reynolds version of the $k - \omega$ SST model, still road conditions and a $Re_L = 13 \times 10^5$ . . . . .	51
3.14	Lift coefficient at different length based Reynolds numbers obtained with the wall function and low-Reynolds version of the $k - \omega$ SST model, still road conditions and a $Re_L = 13 \times 10^5$ . . . . .	51
3.15	Velocity field contour plot at the symmetry plane of the car. Simulation performed with the low Reynolds version of the $k - \omega$ SST model, still road conditions and a $Re_L = 6.5 \times 10^5$ . . . . .	52
3.16	Velocity field contour plot at the symmetry plane of the car. Simulation performed with the wall function version of the $k - \omega$ SST model, still road conditions and a $Re_L = 6.5 \times 10^5$ . . . . .	52
3.17	$c_D$ of different basic bodies. (Adapted from [4]). References in which each basic shape appears (from top to bottom): [5], [6], [7] and [8]. . . . .	52
3.18	$c_P$ plot at the symmetry plane of the car using wall function models. W-F stands for wall function. Upper surface of the car in orange, lower surface in blue. Simulation performed with still road conditions and a $Re_L = 3.5 \times 10^5$ . Position normalized such that 1 equals the car length. . . . .	54

3.19	$c_P$ plot at the symmetry plane of the car using wall function models. W-F stands for wall function. Upper surface of the car in orange, lower surface in blue. Simulation performed with still road conditions and a $Re_L = 6.6 \times 10^5$ . Position normalized such that 1 equals the car length. . . . .	54
3.20	$c_P$ plot at the symmetry plane of the car using wall function models. W-F stands for wall function model. Upper surface of the car in orange, lower surface in blue. Simulation performed with still road conditions and a $Re_L = 9.8 \times 10^5$ . Position normalized such that 1 equals the car length. . .	54
3.21	$c_P$ plot at the symmetry plane of the car using wall function models. W-F stands for wall function model. Upper surface of the car in orange, lower surface in blue. Simulation performed with still road conditions and a $Re_L = 13 \times 10^5$ . Position normalized such that 1 equals the car length. . .	54
3.22	$c_P$ plot at the symmetry plane of the car comparing experimental and CFD results. W-F stands for wall function model. Upper surface of the car in orange, lower surface in blue. Simulation performed with still road conditions and a $Re_L = 13 \times 10^5$ . Position normalized such that 1 equals the car length. . . . .	55
3.23	$c_P$ plot at the symmetry plane of the car comparing experimental and CFD results. Upper surface of the car in orange, lower surface in blue. Simulation performed with still road conditions and a $Re_L = 13 \times 10^5$ . Position normalized such that 1 equals the car length. . . . .	55
3.24	Schematic $c_p$ behaviour when transition from laminar to turbulent occurs. (Adapted from [9]) . . . . .	57
3.25	Flow in the vicinity of a transitional separation bubble. (Adapted from [10])	57
3.26	$c_P$ plot at the symmetry plane of the car. L-R stands for low Reynolds. Upper surface of the car in orange, lower surface in blue. Simulation performed with still road conditions and a $Re_L = 3.5 \times 10^5$ . Position normalized, 1 equals the car length. . . . .	58
3.27	$c_P$ plot at the symmetry plane of the car. L-R stands for low Reynolds. Upper surface of the car in orange, lower surface in blue. Simulation performed with still road conditions and a $Re_L = 6.6 \times 10^5$ . Position normalized, 1 equals the car length. . . . .	58
3.28	$c_P$ plot at the symmetry plane of the car using low Reynolds models. L-R stands for low Reynolds model. Upper surface of the car in orange, lower surface in blue. Simulation performed with still road conditions and a $Re_L = 9.8 \times 10^5$ . Position normalized such that 1 equals the car length. . .	58
3.29	$c_P$ plot at the symmetry plane of the car using low Reynolds models. L-R stands for low Reynolds model. Upper surface of the car in orange, lower surface in blue. Simulation performed with still road conditions and a $Re_L = 13 \times 10^5$ . Position normalized such that 1 equals the car length. . .	58
3.30	Intermittency contour plot over the Electra. Simulation performed with the $\gamma Re_\theta$ model, still road conditions and a $Re_L = 13 \times 10^5$ . . . . .	59

3.31	Intermittency contour plot over the Electra. Simulation performed with the $\gamma Re_\theta$ model, still road conditions and a $Re_L = 13 \times 10^5$ . . . . .	59
3.32	$c_P$ plot at the symmetry plane of the car comparing experimental and low Reynolds results. Upper surface of the car in orange, lower surface in blue. Simulation performed with still road conditions and a $Re_L = 3.5 \times 10^5$ . Position normalized, 1 equals the car length. . . . .	60
3.33	$c_P$ plot at the symmetry plane of the car comparing experimental and low Reynolds results. Upper surface of the car in orange, lower surface in blue. Simulation performed with still road conditions and a $Re_L = 6.6 \times 10^5$ . Position normalized, 1 equals the car length. . . . .	60
3.34	$c_P$ plot at the symmetry plane of the car comparing experimental and CFD results. Upper surface of the car in orange, lower surface in blue. Simulation performed with still road conditions and a $Re_L = 9.8 \times 10^5$ . Position normalized such that 1 equals the car length. . . . .	60
3.35	$c_P$ plot at the symmetry plane of the car comparing experimental and CFD results. Upper surface of the car in orange, lower surface in blue. Simulation performed with still road conditions and a $Re_L = 13 \times 10^5$ . Position normalized such that 1 equals the car length. . . . .	60
3.36	$c_P$ plot at the cross section plane of the car passing through its highest point comparing experimental and CFD results. Simulation performed with still road conditions and a $Re_L = 3.5 \times 10^5$ . Position normalized such that 1 equals the car height. . . . .	61
3.37	$c_P$ plot at the cross section plane of the car passing through its highest point comparing experimental and CFD results. Simulation performed with still road conditions and a $Re_L = 6.6 \times 10^5$ . Position normalized such that 1 equals the car height. . . . .	61
3.38	$c_P$ plot at the cross section plane of the car passing through its highest point comparing experimental and CFD results. Simulation performed with still road conditions and a $Re_L = 9.8 \times 10^5$ . Position normalized such that 1 equals the car height. . . . .	62
3.39	$c_P$ plot at the cross section plane of the car passing through its highest point comparing experimental and CFD results. Simulation performed with still road conditions and a $Re_L = 13 \times 10^5$ . Position normalized such that 1 equals the car height. . . . .	62
3.40	$c_P$ plot at the symmetry plane of the car. W-F stands for wall function model and L-R stands for low Reynolds model. Upper surface of the car in orange, lower surface in blue. Still road conditions and a $Re_L = 3.5 \times 10^5$ . Position normalized: 1 equals the car length. . . . .	63
3.41	$c_P$ plot at the symmetry plane of the car. W-F stands for wall function model and L-R stands for low Reynolds model. Upper surface of the car in orange, lower surface in blue. Still road conditions and a $Re_L = 6.6 \times 10^5$ . Position normalized: 1 equals the car length. . . . .	63

3.42	$c_P$ at the symmetry plane comparing low Reynolds and wall function models. W-F stands for wall function and L-R stands for low Reynolds. Upper surface of the car in orange, lower surface in blue. Simulation performed with still road conditions and a $Re_L = 9.8 \times 10^5$ . Position normalized, 1 equals the car length. . . . .	63
3.43	$c_P$ at the symmetry plane comparing low Reynolds and wall function models. W-F stands for wall function and L-R stands for low Reynolds. Upper surface of the car in orange, lower surface in blue. Simulation performed with still road conditions and a $Re_L = 13 \times 10^5$ . Position normalized such that 1 equals the car length. . . . .	63
3.44	Comparison of the obtained numerical boundary layers at 0.5 car lengths in front of the car. Velocity normalized by dividing by the free-stream velocity and the height normalized in such a way that 1 represents the car height. . . . .	65
3.45	$c_P$ plot comparing boundary layer effect. Simulations performed using the $\gamma Re_\theta$ model at a $Re_L = 13 \times 10^5$ with three of the different studied cases. Orange stands for upper surface and blue for lower surface. . . . .	66
3.46	Resulting effective Reynolds seen by Electra and its respective flow incidence angle for different wind directions ranging from $0^\circ$ to $360^\circ$ at a speed of 15 km/h and a car rolling speed of 25 km/h. . . . .	67
3.47	Experimental and numerical drag coefficient as a function of the wind angle of incidence for a $Re_L = 8.2 \times 10^5$ . Simulations performed with the $\gamma Re_\theta$ model at still conditions. . . . .	68
3.48	Experimental and numerical $y$ force coefficient as a function of the wind angle of incidence for a $Re_L = 8.2 \times 10^5$ . Simulations performed with the $\gamma Re_\theta$ model at still conditions. . . . .	68
3.49	Experimental and numerical pressure coefficient distribution measured at Electra's symmetry plane at an angle of incidence of $30^\circ$ for a $Re_L = 8.2 \times 10^5$ . Simulations performed with the $\gamma Re_\theta$ model at still conditions. Lower surface in blue, upper surface in orange. . . . .	69
3.50	Experimental and numerical pressure coefficient distribution measured at Electra's symmetry plane at an angle of incidence of $15^\circ$ for a $Re_L = 8.2 \times 10^5$ . Simulations performed with the $\gamma Re_\theta$ model at still conditions. Lower surface in blue, upper surface in orange. . . . .	69
3.51	Experimental and numerical pressure coefficient distribution measured at Electra's flow facing side of the cross section plane at an angle of incidence of $30^\circ$ for a $Re_L = 8.2 \times 10^5$ . Simulations performed with the $\gamma Re_\theta$ model at still conditions. . . . .	70
3.52	Experimental and numerical pressure coefficient distribution measured at Electra's wake facing side of the cross section plane at an angle of incidence of $30^\circ$ for a $Re_L = 8.2 \times 10^5$ . Simulations performed with the $\gamma Re_\theta$ model at still conditions. . . . .	70

4.1	Pressure plot wheel detail for moving road conditions. Simulation performed using the $\gamma Re_\theta$ model at a $Re_L = 13 \times 10^5$ . . . . .	72
4.2	Pressure plot wheel detail for moving road conditions. Simulation performed using the $\gamma Re_\theta$ model at a $Re_L = 13 \times 10^5$ . . . . .	72
4.3	Velocity contour plot at the car symmetry plane with moving road conditions. Simulation performed using the $\gamma Re_\theta$ model at a $Re_L = 13 \times 10^5$ . . . . .	73
4.4	Velocity contour plot at the car symmetry plane with still road conditions. Simulation performed using the $\gamma Re_\theta$ model at a $Re_L = 13 \times 10^5$ . . . . .	73
4.5	Turbulent kinetic energy contour plot at the car symmetry plane with moving road conditions. Simulation performed using the $\gamma Re_\theta$ model at a $Re_L = 13 \times 10^5$ . . . . .	73
4.6	Turbulent kinetic energy contour plot at the car symmetry plane with still road conditions. Simulation performed using the $\gamma Re_\theta$ model at a $Re_L = 13 \times 10^5$ . . . . .	73
4.7	Intermittency contour plot at the car lower surface with moving road conditions. Simulation performed using the $\gamma Re_\theta$ model at a $Re_L = 13 \times 10^5$ . . . . .	74
4.8	Intermittency contour plot at the car lower surface with still road conditions. Simulation performed using the $\gamma Re_\theta$ model at a $Re_L = 13 \times 10^5$ . . . . .	74
4.9	Histogram showing the distribution of pressure and friction drag on the different sections of Electra at still road conditions. Simulation performed using the $\gamma Re_\theta$ model at a $Re_L = 13 \times 10^5$ . . . . .	75
4.10	Histogram showing the distribution of pressure and friction drag on the different sections of Electra at moving road conditions. Simulation performed using the $\gamma Re_\theta$ model at a $Re_L = 13 \times 10^5$ . . . . .	75
4.11	Pressure contour plot with moving road conditions. Simulation performed using the $\gamma Re_\theta$ model at a $Re_L = 13 \times 10^5$ . . . . .	76
4.12	Pressure contour plot at Electra top surface with moving road conditions. Simulation performed using the $\gamma Re_\theta$ model at a $Re_L = 13 \times 10^5$ . . . . .	76
4.13	Pressure contour plot at Electra lower surface with moving road conditions. Simulation performed using the $\gamma Re_\theta$ model at a $Re_L = 13 \times 10^5$ . . . . .	76
4.14	Pressure contour plot at Electra side surface with moving road conditions. Simulation performed using the $\gamma Re_\theta$ model at a $Re_L = 13 \times 10^5$ . . . . .	76
4.15	Flow streamlines over the Electra upper surface. Streamlines coloured by velocity magnitude. Simulation performed with moving road conditions using the $\gamma Re_\theta$ model at a $Re_L = 13 \times 10^5$ . . . . .	77
4.16	Flow streamlines over the Electra upper surface. Streamlines coloured by velocity magnitude. Simulation performed with moving road conditions using the $\gamma Re_\theta$ model at a $Re_L = 13 \times 10^5$ . . . . .	77
4.17	Flow streamlines over the Electra lower section. Streamlines coloured by velocity magnitude. Simulation performed with moving road conditions using the $\gamma Re_\theta$ model at a $Re_L = 13 \times 10^5$ . . . . .	78



4.18	Turbulent kinetic energy contour plot at a $x = 0.15$ m $y - z$ plane. Simulation performed with moving road conditions using the $\gamma Re_\theta$ model at a $Re_L = 13 \times 10^5$ . . . . .	78
4.19	Velocity magnitude contour plot at a $x = 0.15$ m $y-z$ plane. Simulation performed with moving road conditions using the $\gamma Re_\theta$ model at a $Re_L = 13 \times 10^5$ . . . . .	78
4.20	Velocity magnitude contour plot at a $x = 0.15$ m $y-z$ plane. Simulation performed with still road conditions using the $\gamma Re_\theta$ model at a $Re_L = 13 \times 10^5$ . . . . .	78
4.21	Velocity contour plot at the $x$ plane passing through Electra's highest point. Moving road simulation performed with $\gamma Re_\theta$ model at $30^\circ$ crosswind and a $Re_L = 8.2 \times 10^5$ . . . . .	79
4.22	Turbulent kinetic energy contour plot at the $x$ plane passing through Electra's highest point. Moving road simulation performed with $\gamma Re_\theta$ model at $30^\circ$ crosswind and a $Re_L = 8.2 \times 10^5$ . . . . .	79
4.23	Flow streamlines over Electra lower section. Streamlines coloured by velocity magnitude. Moving road simulation performed with $\gamma Re_\theta$ model at $30^\circ$ crosswind and a $Re_L = 8.2 \times 10^5$ . . . . .	80
4.24	Flow streamlines over Electra lower section. Streamlines coloured by velocity magnitude. Moving road simulation performed with $\gamma Re_\theta$ model at $30^\circ$ crosswind and a $Re_L = 8.2 \times 10^5$ . . . . .	80
4.25	Flow streamlines over Electra upper section. Streamlines coloured by velocity magnitude. Moving road simulation performed with $\gamma Re_\theta$ model at $30^\circ$ crosswind and a $Re_L = 8.2 \times 10^5$ . . . . .	80
4.26	Flow streamlines over Electra upper section. Streamlines coloured by velocity magnitude. Moving road simulation performed with $\gamma Re_\theta$ model at $30^\circ$ crosswind and a $Re_L = 8.2 \times 10^5$ . . . . .	80
4.27	Intermittency contour plot at Electra's upper surface. Moving road simulation performed with $\gamma Re_\theta$ model at $30^\circ$ crosswind and a $Re_L = 8.2 \times 10^5$ . . . . .	81
4.28	Intermittency contour plot at Electra's lower surface. Moving road simulation performed with $\gamma Re_\theta$ model at $30^\circ$ crosswind and a $Re_L = 8.2 \times 10^5$ . . . . .	81
4.29	Drag, lift and $y$ force coefficient as a function of the angle of yaw. Simulation performed with the $\gamma Re_\theta$ model with moving conditions at a $Re_L = 8.2 \times 10^5$ . . . . .	82
4.30	$x$ , $y$ and $z$ moment coefficient as a function of the angle of yaw. Simulation performed with the $\gamma Re_\theta$ model with moving conditions at a $Re_L = 8.2 \times 10^5$ . . . . .	82
4.31	Effect of vertical position $h$ on the wheel lift and drag coefficients. Adapted from [11] . . . . .	83
4.32	Pressure contour plot over a still wheel. Simulation performed with $\gamma Re_\theta$ model and still road conditions with a $Re_L = 13 \times 10^5$ . . . . .	84
4.33	Pressure contour plot over a rotating wheel. Simulation performed with $\gamma Re_\theta$ model and moving road conditions with a $Re_L = 13 \times 10^5$ . . . . .	84

4.34	Velocity magnitude contour plot over a still wheel. Simulation performed with $\gamma Re_\theta$ model and still road conditions with a $Re_L = 13 \times 10^5$ . . . . .	84
4.35	Velocity magnitude contour plot over a rotating wheel. Simulation performed with $\gamma Re_\theta$ model and moving road conditions with a $Re_L = 13 \times 10^5$ . . . . .	84
4.36	3D flow structures induced by a rotating wheel. . . . .	85
4.37	Catia 3D model of the rear-view mirror. . . . .	86
4.38	Catia 3D model of the rear-view mirror. . . . .	86
4.39	Velocity magnitude contour plot in a $z$ plane crossing the rear-view mirror (Upper side seen). Simulation performed with the $\gamma Re_\theta$ model with a free-stream velocity of 8.2 m/s. . . . .	87
4.40	Turbulent kinetic energy contour plot in a $z$ plane crossing the rear-view mirror (Upper side seen). Simulation performed with the $\gamma Re_\theta$ model with a free-stream velocity of 8.2 m/s. . . . .	87
4.41	Independent drag coefficient of various joints configurations based on thickness “h”. Adapted from [12]. . . . .	88
4.42	Independent drag coefficient of surface bolts and rivets. Adapted from [12]. . . . .	89
4.43	Rivet independent drag coefficient as a function of its relative elevation with respect to the surface. Adapted from [12]. . . . .	90
4.44	Electra drag coefficient and effect of the different simplifications. Simulation performed with the $\gamma Re_\theta$ model at moving road conditions and a $Re_L = 13 \times 10^5$ . . . . .	91
5.1	Velocity contour plot at the car symmetry plane with moving road conditions. Simulation performed using the original geometry and the $\gamma Re_\theta$ model at a $Re_L = 13 \times 10^5$ . . . . .	93
5.2	Velocity contour plot at the car symmetry plane with moving road conditions. Simulation performed using the original geometry with increased height of 45 mm and the $\gamma Re_\theta$ model at a $Re_L = 13 \times 10^5$ . . . . .	93
5.3	3D model of the first modification based on performance. . . . .	94
5.4	3D model of the first modification based on performance. . . . .	94
5.5	Velocity magnitude contour plot at a $x = 0.15$ m $y$ - $z$ plane. Simulation performed with Electra at moving road conditions using the $\gamma Re_\theta$ model at a $Re_L = 13 \times 10^5$ . . . . .	95
5.6	Velocity magnitude contour plot at a $x = 0.15$ m $y$ - $z$ plane. Simulation performed with the first performance modification at moving road conditions using the $\gamma Re_\theta$ model at a $Re_L = 13 \times 10^5$ . . . . .	95
5.7	Turbulent kinetic energy contour plot at a $x = 0.15$ m $y - z$ plane. Simulation performed with Electra at moving road conditions using the $\gamma Re_\theta$ model at a $Re_L = 13 \times 10^5$ . . . . .	95
5.8	Turbulent kinetic energy contour plot at a $x = 0.15$ m $y - z$ plane. Simulation performed with the first performance modification at moving road conditions using the $\gamma Re_\theta$ model at a $Re_L = 13 \times 10^5$ . . . . .	95
5.9	Skirt comparison between the first and second performance modifications. . . . .	96

5.10	Velocity magnitude contour plot at a $x = 0.15$ m $y$ - $z$ plane. Simulation performed with the first performance modification at moving road conditions using the $\gamma Re_\theta$ model at a $Re_L = 13 \times 10^5$ . . . . .	97
5.11	Velocity magnitude contour plot at a $x = 0.15$ m $y$ - $z$ plane. Simulation performed with the second performance modification at moving road conditions using the $\gamma Re_\theta$ model at a $Re_L = 13 \times 10^5$ . . . . .	97
5.12	Turbulent kinetic energy contour plot at a $x = 0.15$ m $y - z$ plane. Simulation performed with the first performance modification at moving road conditions using the $\gamma Re_\theta$ model at a $Re_L = 13 \times 10^5$ . . . . .	97
5.13	Turbulent kinetic energy contour plot at a $x = 0.15$ m $y - z$ plane. Simulation performed with the second performance modification at moving road conditions using the $\gamma Re_\theta$ model at a $Re_L = 13 \times 10^5$ . . . . .	97
5.14	3D model of the third modification based on performance. . . . .	98
5.15	Skirt comparison between the second and third performance modifications. . . . .	98
5.16	Velocity magnitude contour plot at a $x = 0.15$ m $y$ - $z$ plane. Simulation performed with the second performance modification at moving road conditions using the $\gamma Re_\theta$ model at a $Re_L = 13 \times 10^5$ . . . . .	99
5.17	Velocity magnitude contour plot at a $x = 0.15$ m $y$ - $z$ plane. Simulation performed with the third performance modification at moving road conditions using the $\gamma Re_\theta$ model at a $Re_L = 13 \times 10^5$ . . . . .	99
5.18	Turbulent kinetic energy contour plot at a $x = 0.15$ m $y - z$ plane. Simulation performed with the second performance modification at moving road conditions using the $\gamma Re_\theta$ model at a $Re_L = 13 \times 10^5$ . . . . .	99
5.19	Turbulent kinetic energy contour plot at a $x = 0.15$ m $y - z$ plane. Simulation performed with the third performance modification at moving road conditions using the $\gamma Re_\theta$ model at a $Re_L = 13 \times 10^5$ . . . . .	99
5.20	Flow streamlines over the third performance modification. Streamlines coloured by velocity magnitude. Simulation performed with moving road conditions using the $\gamma Re_\theta$ model at a $Re_L = 13 \times 10^5$ . . . . .	100
5.21	Flow streamlines over the third performance modification. Streamlines coloured by velocity magnitude. Simulation performed with moving road conditions using the $\gamma Re_\theta$ model at a $Re_L = 13 \times 10^5$ . . . . .	100
5.22	3D model of the first modification based on new concept. . . . .	101
5.23	3D model of the first modification based on new concept. . . . .	101
5.24	Velocity magnitude contour plot at a $x = 0.15$ m $y$ - $z$ plane. Simulation performed with the first new concept modification at moving road conditions using the $\gamma Re_\theta$ model at a $Re_L = 13 \times 10^5$ . . . . .	102
5.25	Velocity magnitude contour plot at the car middle plane. Simulation performed with the first new concept modification at moving road conditions using the $\gamma Re_\theta$ model at a $Re_L = 13 \times 10^5$ . . . . .	102

5.26	Turbulent kinetic energy contour plot at a $x = 0.15$ m $y - z$ plane. Simulation performed with first new concept modification at moving road conditions using the $\gamma Re_\theta$ model at a $Re_L = 13 \times 10^5$ . . . . .	102
5.27	Turbulent kinetic energy contour plot at middle car plane. Simulation performed with first new concept modification at moving road conditions using the $\gamma Re_\theta$ model at a $Re_L = 13 \times 10^5$ . . . . .	102
5.28	3D model of the second modification based on new concept. . . . .	103
5.29	3D model of the second modification based on new concept. . . . .	103
5.30	Velocity magnitude contour plot at a $x = 0.15$ m $y-z$ plane. Simulation performed with the second new concept modification at moving road conditions using the $\gamma Re_\theta$ model at a $Re_L = 13 \times 10^5$ . . . . .	104
5.31	Velocity magnitude contour plot at the car middle plane. Simulation performed with the secondnew concept modification at moving road conditions using the $\gamma Re_\theta$ model at a $Re_L = 13 \times 10^5$ . . . . .	104
5.32	Turbulent kinetic energy contour plot at a $x = 0.15$ m $y - z$ plane. Simulation performed with second new concept modification at moving road conditions using the $\gamma Re_\theta$ model at a $Re_L = 13 \times 10^5$ . . . . .	104
5.33	Turbulent kinetic energy contour plot at middle car plane. Simulation performed with second new concept modification at moving road conditions using the $\gamma Re_\theta$ model at a $Re_L = 13 \times 10^5$ . . . . .	104
5.34	Turbulent kinetic energy contour plot at a $x = 0.15$ m $y - z$ plane. Simulation performed with second new concept modification at moving road conditions using the $\gamma Re_\theta$ model at a $Re_L = 13 \times 10^5$ . . . . .	105
5.35	Turbulent kinetic energy contour plot at middle car plane. Simulation performed with second new concept modification at moving road conditions using the $\gamma Re_\theta$ model at a $Re_L = 13 \times 10^5$ . . . . .	105

# List of Tables

- 2.1 Configuration:  $\alpha = 0^\circ$  and  $h = 100\% c$  . . . . . 13
- 2.2 Configuration:  $\alpha = 4^\circ$  and  $h = 100\% c$  . . . . . 13
- 2.3 Comparison between the experimental normalized location on the upper surface ( $x/chord$ ) where boundary layer transition was detected [13] and location obtained by the  $\gamma Re_\theta$  simulation. . . . . 14
  
- 3.1 Nomenclature for each of the tested cases and non-slip floor distance in front of the car. . . . . 64
- 3.2 Aerodynamic coefficients for each of the test cases at the specified length based Reynolds number. . . . . 65
  
- 4.1 Electra exposed wheel drag and lift coefficient for different combinations of road and wheel conditions. Simulations performed with the  $\gamma Re_\theta$  model and a  $Re_L = 13 \times 10^5$ . . . . . 84
- 4.2 Effect of wheels on the drag and lift coefficients of the car. Simulation performed with  $\gamma Re_\theta$  model and a  $Re_L = 13 \times 10^5$ . . . . . 86
  
- 5.1 Electra drag coefficient comparison between still and moving road conditions for different car heights. Simulations performed with  $\gamma Re_\theta$  model and a  $Re_L = 13 \times 10^5$ . . . . . 93
- 5.2 Drag coefficient comparison between Electra and the first performance modification at still and moving road conditions. Simulations performed with  $\gamma Re_\theta$  model and a  $Re_L = 13 \times 10^5$ . . . . . 94
- 5.3 Drag coefficient comparison between Electra and the second performance modification at still and moving road conditions. Simulations performed with  $\gamma Re_\theta$  model and a  $Re_L = 13 \times 10^5$ . . . . . 96
- 5.4 Drag coefficient comparison between Electra and the third performance modification at still and moving road conditions. Simulations performed with  $\gamma Re_\theta$  model and a  $Re_L = 13 \times 10^5$ . . . . . 98
- 5.5 Drag coefficient comparison between Electra and the first new concept modification at still and moving road conditions. Simulations performed with  $\gamma Re_\theta$  model and a  $Re_L = 13 \times 10^5$ . . . . . 101

5.6	Drag coefficient comparison between Electra and the second new concept modification at still and moving road conditions. Simulations performed with $\gamma Re_\theta$ model and a $Re_L = 13 \times 10^5$ . . . . .	103
-----	--	-----

## Abstract

The search for better performance is an actual challenge in the automotive industry. This is the reason why Shell proposes students from the entire globe to participate in its eco-marathon, a competition in which the maximum efficiency is searched. This thesis presents a numerical and experimental study of the *A&M UrbanConcept* vehicle: *Electra*. Wind tunnel conditions are simulated using RANS and URANS simulations in ANSYS FLUENT and compared to wind tunnel experimental data, allowing to validate numerical results. Once the numerical set-up is validated, a more in-depth study of *Electra*'s aerodynamic properties is performed. In this study, track conditions are simulated and compared to wind tunnel conditions. This comparison allows to see the ground effect phenomenon and how it affects the aerodynamic properties of the car. Bearing in mind all simplifications made on the numerical model, aerodynamic corrections are applied to the obtained results. Then, a thorough discussion on surface imperfections and protuberances is made, being possible to estimate the drag value of the real car. Using this study, it is possible to modify the car geometry in order to improve its performance, achieving a drag decrease of 38% with respect to the original geometry. Finally, the aerodynamic effect that the introduction of a new platform chassis type could have on *Electra*'s aerodynamics is tested and optimized.

## Acknowledgements

The university is a gear that, together with others, creates the perfect machine that is the society we live in. We are unique, unrepeatable pieces that fit like numbers that add up and form a whole.

Not long ago I began to be a new piece of the wonderful gear that is the university, where thanks to the teachers, I felt how their wisdom was transmitted to me while I acquired mine. Where, thanks to my colleagues, I learned to be part of a team. To lead at times. To stand as one in others. Where thanks to my friends, who shared their experiences with me and who were always willing to listen to me, I learned to be generous with others.

Besides being part of the university gear, I am also part of another important gear: my wonderful family, without which I would not be who I am. They made me love music, art, museums, travelling, ... and taught me something essential like loving my neighbour, feeling empathy, being strong and never giving up. They were also always there to help me by transmitting serenity and temperance, giving me beautiful advice.

That's why I want to try to give back, to all those who supported and believed in me, a little bit of that love through some words of gratitude. I apologize in advance to all of those that I forgot to mention. You know that you are also in my heart.

I thank all the sponsors who have directly or indirectly helped me to carry out this master's thesis through their financial contribution. I really appreciate their willingness to be part of the advancement of society, and how they believe and invest in us.

I thank Prof. V. E. Terrapon, Dr. T. Andriane and Prof. P. Duysinx for their advice and for their time. For giving me guidelines that allowed me to continue on the right direction. Without them I would not have achieved the elaboration of this thesis. Their contribution of experience and knowledge has made of my work an enriching experience.

Thanks to the entire university team for giving me their unconditional support encouraging and supporting me. In particular, thanks to Adrien Crovato, François Rigo, Sébastien Niessen and Hüseyin Güner.

Thanks to the Shell Eco Marathon team for always being willing to listen me and help me when I needed them. Special mention to Simon Bauduin, Maxime Collet, Pablo Alarcón, Antonio Martinez and Antoine Désiron.

Thanks to my friends for their exquisite education, good personal treatment, poise and for their unconditional friendship. They gave everything without expecting anything in return. Thanks to them all, I was able to go on without giving up.



To my family, who with their effort inculcated me good habits and values. With their support they have helped me to move forward even in the most difficult times.

This has been for me my time at the university, that gear where I deposited all my dreams and hopes.

*"Scientist discover the world that exists; engineers create the world that never was."*

*Theodore von Kármán*

# Chapter 1

## Introduction

### Motivation

Scientists argue that even though Earth has gone through different climatic cycles which have been attributed to small changes in the orbit of our planet, the current unprecedented warming trend is largely attributable to the human being. Some of the facts that show this change are the increase in global temperature, glacial retreat, or the presence of increasingly frequent extreme climate events [14].

Transport accounts for around 30% of global  $C0_2$  emissions and contributes to about 14% of greenhouse gas emissions, as well as the emission of other gases highly harmful to humans [15]. For this reason, energy efficiency on the roads has become paramount.

Looking for energy efficiency on the roads, Shell has created an annual competition that tests students from all over the world. It is a challenge in which students have to design, build and test their proposals, giving way to creativity, camaraderie and leadership.

This challenge is celebrated worldwide in three areas: Europe, America and Asia. Many categories make up this event such as prototypes and UrbanConcept. This year, the competition will be updated by introducing a new category, the Autonomous UrbanConcept, where Shell will allow students to focus on one of the biggest challenges of the future of the transport industry. This new category will make students concentrate not only on efficiency, but also in the development of new software that will allow these driver-less cars to complete different challenges successfully.

Living in a world in which autonomous cars seem to be the future for most automobile manufacturers, ULiège's team does not want to lose the opportunity to enter this new category, and therefore it is preparing a new autonomous compatible project.

## History of car aerodynamics

From the dawn of the automotive industry in 1886, one of the main challenges that engineers have faced has been aerodynamics. This fluid-car interaction inserts forces and moments that directly affect the performance of a vehicle.

One of the most important aerodynamic forces in commercial vehicles is drag. Aerodynamic drag being defined as the force that the fluid surrounding a vehicle exerts in opposite direction to the vehicle motion, is one of the main impediments that prevent humans from travelling from point A to point B faster and more efficiently. As soon as the automobile industry started developing, the quest for faster cars made obvious the importance of drag reduction. Its dependence on the square of the velocity makes it a critical parameter for vehicle design.

The first attempts to reduce drag were carried out by record-braking cars such as Camille Jenatzy's La Jamais Contente (100 km/h barrier beaker in 1899) (fig. 1.1) or the Stanley Steamer Rocket (200 km/h barrier breaker in 1906) (fig. 1.2) by making use of basic shapes.



Figure 1.1: La Jamais Contente 1899.

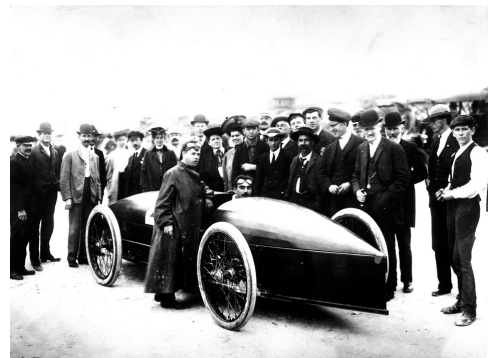


Figure 1.2: Stanley Steamer Rocket 1906.

It was Alfa in 1914 with its 40/60 HP Aerodinamica (figure 1.3) the first manufacturer who tried, unsuccessfully, to apply an aerodynamic-based design shape to a commercial car. It was not until the end of WWI that Rumpler commercialized the known as the first streamlined production car<sup>1</sup>. With a drag coefficient of 0.28, the Rumpler Tropfenwagen (figure 1.4) was by a large margin the most aerodynamic car of its time, being this a competitive value even for today's standards.

---

<sup>1</sup>The term "streamlined car" makes its first appearance in *The streamlined Car, a New Shape for Automobile Bodies*, by P. Jaray.

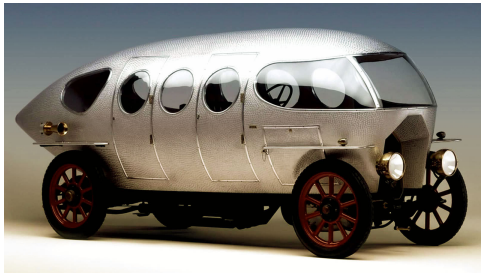


Figure 1.3: A.L.F.A. 40/60 HP Aerodinamica.

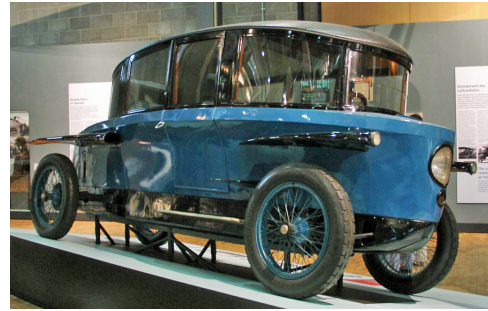


Figure 1.4: Rumpler Tropfenwagen.

In the 70's, detail optimization became a standard in car design. This method allowed to reduce drag adapting the car shape to other demands such as styling or manufacturing. However, even though this method allowed to reduce drag, going beyond a drag coefficient of 0.4 was found to be almost impossible. A good example of the potential of this method is the Volkswagen Scirocco I ( $c_D = 0.41$ ) shown in figure 1.5.

In the 80's, in order to break this "barrier", engineers began to design cars following the opposite process to the one followed in the 70's. Instead of applying aerodynamic improvements to a design based on non-aerodynamic parameters, engineers start from a low drag configuration and modify its bodywork until reaching the final design. A good example of the first cars designed under this process is the Audi 100 III from 1982 ( $c_D = 0.3$ ) shown in figure 1.6.



Figure 1.5: Volkswagen Scirocco I.



Figure 1.6: Audi 100 III.

Nowadays, thanks to the development of computer performance and CFD techniques, the drag coefficient of passenger cars has been further reduced. Great examples are the currently commercialized Mercedes CLA 180 BlueEFFICIENCY Edition ( $c_D = 0.23$ ) or the Tesla Model S ( $c_D = 0.24$ ). Both are shown in figures 1.7 and 1.8 respectively.

Thanks to competitions such as the Shell Eco Marathon, students are capable of pushing these boundaries even further showing that obtaining incredibly low values such as 0.048 is possible with extreme designs such as the Eco-Runner VI from Team Delft.



Figure 1.7: Mercedes CLA 180 BlueEF-FICIENCY Edition.



Figure 1.8: Tesla Model S.

Other aerodynamic forces such as lift, lateral force or moments can affect the stability of the vehicle, making them also key parameters to study.

## Objectives and problem definition

The objective of this thesis is to fully characterize the main aerodynamic properties of the *A&M Shell Eco Marathon Urban Concept* in order to optimize its shape and prepare the team for a future concept. The proposal of the University of Liège is the *Electra*. The *Electra* has been ULiège's contender since 2014. As can be seen in figure 1.9 the *Electra* presents a streamlined body trying to find the maximum energetic efficiency. This is also reflected in its attention to details such as materials or construction. Its semi monocoque construction coupled with the use of light materials such as carbon fibre or aluminium allows to obtain a weight below 120 kg.



Figure 1.9: *Electra* participating at the 2015 Shell Eco Marathon Europe competition.

The *Electra* is designed to travel at a target average speed of 25 km/h. The flow around the car is characterized by a length based reference Reynolds number ( $Re_{L_{ref}}$ ) of 1,306,591. The Reynolds number is defined as

$$Re = \frac{\rho V L}{\mu}, \quad (1.0.1)$$

where  $\rho$  is the air density,  $V$  is the free stream velocity,  $L$  the characteristic length and  $\mu$  the air viscosity. This is a non-dimensional parameter that represents the ratio of inertial to viscous forces. Taking into account the same shape, all flows with the same  $Re$  will yield the same flow characteristics, making the  $Re$  a very powerful tool for engineers. Due to this similarity rule, it is possible to scale the geometry and obtain the same flow characteristics as in the real model just by modifying the three other variables.

Catia V5 is used to build the 3D model of the Electra. The studied CAD geometry (figure 1.10) represents a simplified model of the real car in which external details such as surface imperfections, rear-view mirrors or screw heads are not taken into account. The wheels and the wheel well are simplified as shown in figure 1.11. As can be seen the cavity of the wheel well is closed and therefore the part of the wheel that remains inside the well is not modelled. Morelli [16] and Scibor-Rylski [11] arrived to the conclusion that the drag coefficient of a car wheel could be approximated as the drag coefficient of the exposed wheel, as this coefficient does not change in a significant manner even if the wheel is partially covered by the wheel well. It will be therefore possible to easily correct the error introduced by this simplification.

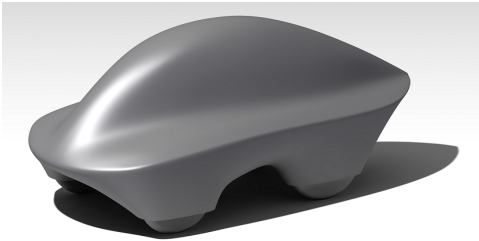


Figure 1.10: Catia CAD model used to perform the numerical simulations.

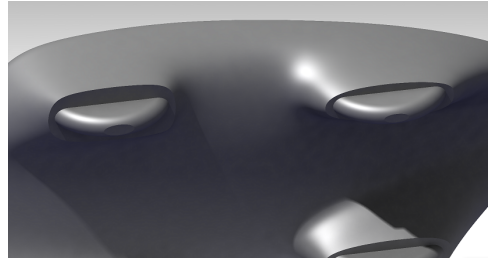


Figure 1.11: Detail of the wheel well simplification in the CAD model.

The mentioned simplifications were accomplished in order to lower the mesh complexity and therefore be able to refine the mesh in a more effective manner. A clean up process of the CAD model was also necessary before the generation of the mesh in order to obtain successful results.

The area of reference that will be used in all non-dimensional variables such as the drag or lift coefficient is calculated by projecting the contour of the car over a projection plane as shown in figure 1.12 yielding a reference area ( $A_{ref}$ ) of  $0.957 \text{ m}^2$ . For the moment coefficients where a reference length is also needed, the length of the car is taken as reference, having a  $L_{ref}$  of 2.75 m.



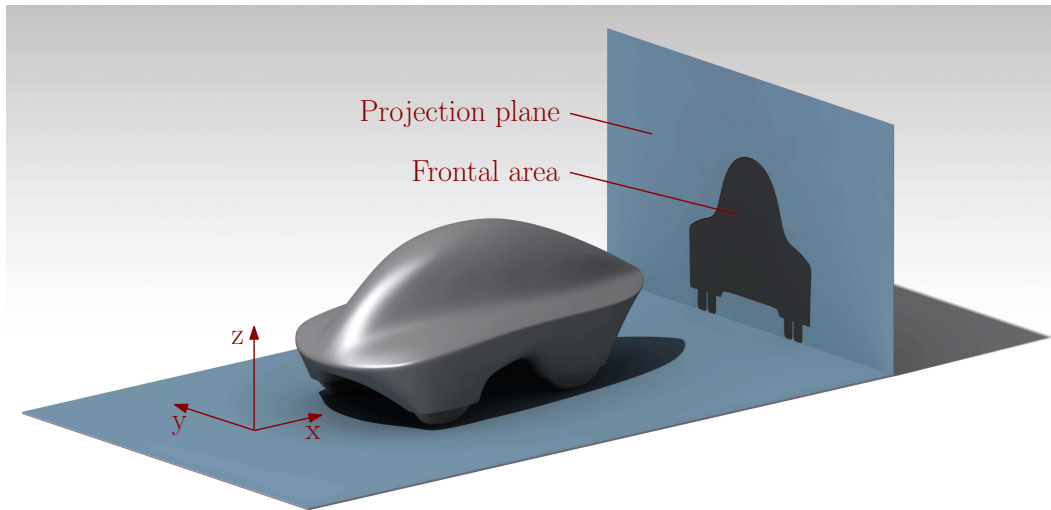


Figure 1.12: Graphical representation of the projection plane in which the frontal area of the car is calculated and definition of the axes of reference.

The direction of the axes of reference will be defined as the ones shown in figure 1.12, in such a way that drag force is defined as the force acting in the  $x$  axis and the lift as the force acting in the  $z$  axis.

## Structure of this thesis

This thesis is divided into 5 parts. The first part will present the numerical and experimental methodologies, and a first validation of the numerical set-up will be made with the benchmark case of the Ahmed body.

In the second part, the numerical simulations will be validated through force and pressure tests carried out at the ULiège's wind tunnel facilities. Zero angle of yaw and crosswind conditions will be considered.

The third part, will consider some advanced aerodynamic studies where moving conditions at zero angle of yaw and crosswind will be studied, being possible to briefly observe the impact that wind direction could have on the vehicle stability. This part will also contain a correction for the wheel and rear-view mirror simplifications and a discussion of the effect that surface imperfections and protuberances can have on Electra's aerodynamics.

In the fourth part, the effect of modifications on the Electra geometry will be studied. Two kinds of modifications were developed:



- Purely performance-based modifications, in which the height effect on the coefficient values will be studied and the high drag regions of Electra will be modified in order to optimize its resistance to air, and hence its efficiency.
- New concept modifications, in which the impact that a potential new platform type chassis would have in Electra's aerodynamics will be analysed, preparing the team for the future project.

Finally, all results and a critical overview will be presented in the conclusion, allowing to prepare the guidelines for future aerodynamic studies of the *A&M Shell Eco-marathon* vehicle prototype. The workflow diagram of this thesis is presented in Annex *I*.

# Chapter 2

## Methodology

In order to fully describe the aerodynamic characteristics of the UrbanConcept car, this work will base its foundations into two pillars: experimental and numerical studies.

While the experimental study allows to obtain real world data, numerical investigation allows to have a clear view of the overall flow around the car. The combination of both allows to quickly study the aerodynamic characteristics of multiple configurations thanks to the numerical simulations, once these are validated through experimental testing. In this section, the methodology followed to perform both types of studies is detailed.

### 2.1 Numerical methodology

Numerical simulations is one of the main pillars in which today's aerodynamic studies are based. The three dimensional nature of the flow around a car necessitates from large computational capabilities, reason why engineers around the world make use of Reynolds averaged (RANS) or detached eddy (DES) simulations to develop car aerodynamics. In this work, RANS simulations were used. RANS is a much cheaper approach than direct numerical simulation (DNS) that presents an approximation of the complete complex solution. In this thesis, all numerical simulations were performed using ANSYS Fluent 19.0.

The Navier-Stokes equations <sup>1</sup> present a chaotic complex solution that varies in time and space. For a viscous incompressible flow one has:

$$\begin{aligned}\partial_t \tilde{u}_i + \tilde{u}_j \partial_j \tilde{u}_i &= -\frac{1}{\rho} \partial_i \tilde{p} + \nu \nabla^2 \tilde{u}_i, \\ \partial_i \tilde{u}_i &= 0,\end{aligned}\tag{2.1.1}$$

where  $\tilde{u}$  represents the total velocity of the flow.

---

<sup>1</sup>The following explanations are based on the ones presented by P.A Durbin and B.A Patterson-Reif [17]

Taking this chaotic nature into account is avoidable when only the main characteristics of the averaged flow are needed. In order to reduce the complexity of the solution, the total velocity ( $\tilde{u}$ ) can be decomposed into the sum of the mean velocity ( $U(\mathbf{x}, t) = \overline{\tilde{u}^2}$ ) and its fluctuations ( $u(\mathbf{x}, t)$ ) as follows:  $\tilde{u} = U(\mathbf{x}, t) + u(\mathbf{x}, t)$ . Introducing this decomposition into the Navier-Stokes equations and computing their average one obtains the so called RANS equations:

$$\begin{aligned} \partial_i U_i + U_j \partial_j U_i &= -\frac{1}{\rho} \partial_i P + \nu \nabla^2 U_i - \underbrace{\partial_j \overline{u_j u_i}}_{R.S.}, \\ \partial_i U_i &= 0. \end{aligned} \tag{2.1.2}$$

The term named as R.S. in eq. 2.1.2 is called the Reynolds stress. This term adds six unknowns to the system of four equations, yielding a closure problem of the system. In order to solve this problem, a modelling of the turbulence is necessary.

Depending on the level of modelling of the boundary layer, turbulence models could be divided into two groups:

- Low Reynolds models
- Wall function models

As can be observed in figure 2.1, when the velocity profile of the turbulent boundary layer is plotted using the wall units  $U^+$  and  $y^+$ , where  $y^+$  is the dimensionless wall coordinate defined as  $y^+ = \frac{y u^*}{\nu}$  (being  $u^*$  the friction velocity), and  $U^+$  is the dimensionless velocity defined as  $U^+ = \frac{1}{\kappa} \ln y^+ + C^+$  (where  $C^+$  is a constant), the velocity profile follows a universal profile valid for all kinds of flows. This fact is exploited, as it allows to model the inner region of the boundary layer without directly computing it. While low Reynolds models only model the viscous sub-layer, wall function models model up to the log layer. Certainly, low Reynolds models require of a finer mesh at the boundary layer and hence are more CPU intensive than the latter. However, this not without showing more deficiencies than the low Reynolds models as will be seen in this report. In order to stave off the multiple shortcomings that each model could present, multiple models are analysed in this thesis.

---

<sup>2</sup>The  $\bar{j}$  notation represents the average of variable j.

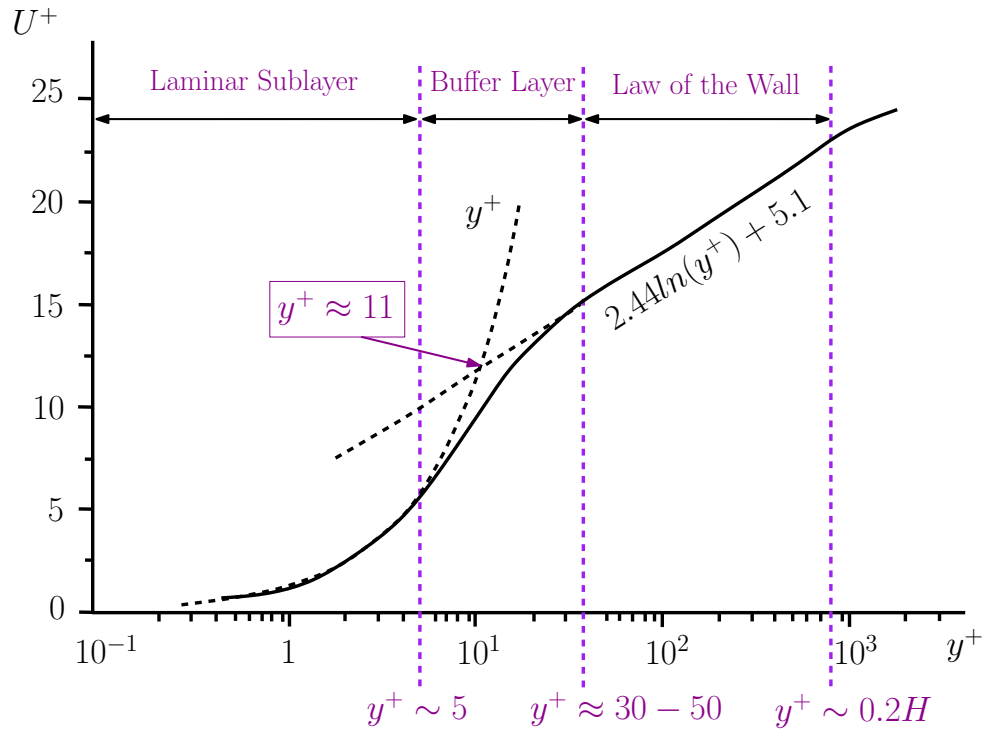


Figure 2.1: Subregions of the inner layer.

### 2.1.1 Turbulence and transition models

As already stated, depending on the level of modelling of the boundary layer, two types of models can be distinguished, but, what is the real influence of this modelling on the solution when treating with a real case? In order to answer this question and try to find the order of magnitude of the error that this modelling could introduce, both types of models are studied in this thesis.

#### Wall Function Models

The wall function version of the reliable  $k - \varepsilon$  and the  $k - \omega$  SST model will be used to study the effect of this boundary layer modelling.

- $k - \varepsilon$  realizable

The "standard"  $k - \varepsilon$  was the first two-equation model used in applied CFD (Published by Jones and Launder in 1972 [18]), reason for its widespread popularity. The  $k - \varepsilon$  model determine the local turbulent viscosity from two equations: the turbulence kinetic energy and the energy dissipation rate transport equations [18].

The standard  $k - \varepsilon$  model presented many deficiencies which were attempted to be resolved over the years, giving way to multiple versions this model. The realizable  $k - \varepsilon$

model, proposed by Shih et al. [19], tries to solve some of these deficiencies by introducing a new eddy-viscosity formula and a new modelling of the dissipation based on the dynamic equation of the mean square vorticity fluctuation

Non-equilibrium wall functions are used in order to model the near wall region. These wall functions are suggested by M. Lanfrit [20] for external aerodynamics studies. The non-equilibrium wall functions were designed to overcome some of the traditional wall function drawbacks by being sensitized to the effects of pressure gradients and taking into account the variation thickness of the viscous sublayer for turbulent kinetic energy budget calculations [20] [21].

- k -  $\omega$  SST

This model, presented by Menter in 1994, is a variant of the basic k- $\omega$  turbulent model, which is known for having many shortcomings such as over-prediction of shear stress in adverse pressure gradient boundary layers or for having a spurious sensitivity to free-stream conditions. Menter introduced a bound on the eddy viscosity ( $\nu_T$ ) to prevent an increase on the stress intensity ratio.

This last bound, also called limiter, is undesirable in free-shear flow. In order to confine these constraints to the boundary layer, the SST variant is capable of using the k- $\omega$  scheme near the wall while making use of the k- $\varepsilon$  model in the rest of the flow with the use of the called blending function [17]. This model is known for being quite effective when studying external flows, and therefore will be interesting to observe how it behaves in the studied case.

This model presents a near wall treatment capable of automatically shifting from the wall function to the low-Reynolds formulation depending on the near-wall grid-spacing [22]. However, in order to measure the impact that the formulation of this model has on the obtained results, the  $y^+$  values at the surface will be checked to remain inside the log-law layer ( $30 < y^+ < 300$ ), assuring the use of the wall function formulation over the entire surface.

## Low Reynolds Models

- k -  $\omega$  SST

As already stated, the clever formulation of the model allows to directly switch from the wall function formulation to the low-Reynolds one. As for the wall function formulation, the  $y^+$  values will be checked to remain inside the viscous sublayer ( $y^+ \simeq 1$  and  $y^+ < 5$ ).

All these models model the flow field as fully turbulent, which could introduce large errors depending on the studied case as will be seen hereafter. It was therefore interesting to study the effect of the laminar to turbulent transition. The transition model used to study this phenomenon is the  $\gamma Re_\theta$ .

- $\gamma - Re_\theta$

The  $\gamma - Re_\theta$  is a correlation-based transition model. The main advantage of a transition model is its capability of predicting the transition point at which the laminar boundary layer becomes turbulent. This transition model couples the  $k-\omega$  SST transport equations with two other transport equations for the intermittency and for the transition momentum thickness Reynolds number [23].

ANSYS Fluent uses an empirical correlation developed by Robin B. Langtry and Florian R. Menter in 2009, in which different test cases were used in order to calibrate the model [24]. Due to the ability to let the intermittency vary across the boundary layer, this transition model allows to capture the turbulent to laminar transition generated due to a laminar separation bubble without further correction.[25]

As for the  $k - \omega$  SST model, the  $y^+$  values will be checked to remain inside the viscous sublayer ( $y^+ \simeq 1$  and  $y^+ < 5$ ).

In commercial passenger cars, the approximation of the flow as being fully turbulent does not account as a big source of errors. High percentage of pressure drag compared to skin friction drag coupled with the presence of surface artefacts, such as air intakes or junctions between different pieces, which triggers the appearance of turbulence, makes this a good approximation. However in cases where skin friction is of capital importance, this approximation could become a large source of errors due to the difference in shear stress of a laminar and turbulent flow. This difference can be observed in figure 2.2, where the frictional resistance in pipes as a function of the Reynolds number is shown.

In order to observe this effect, the example of a NACA 4412 in ground effect at a height value equal to the airfoil chord is taken into account <sup>3</sup>. The obtained results are shown in tables 2.1 and 2.2.

---

<sup>3</sup>These 2D simulations were performed after an exhaustive study in order to assure the best possible solution for each of the turbulence/transition models. A structured C-H Multiblock grid was used.

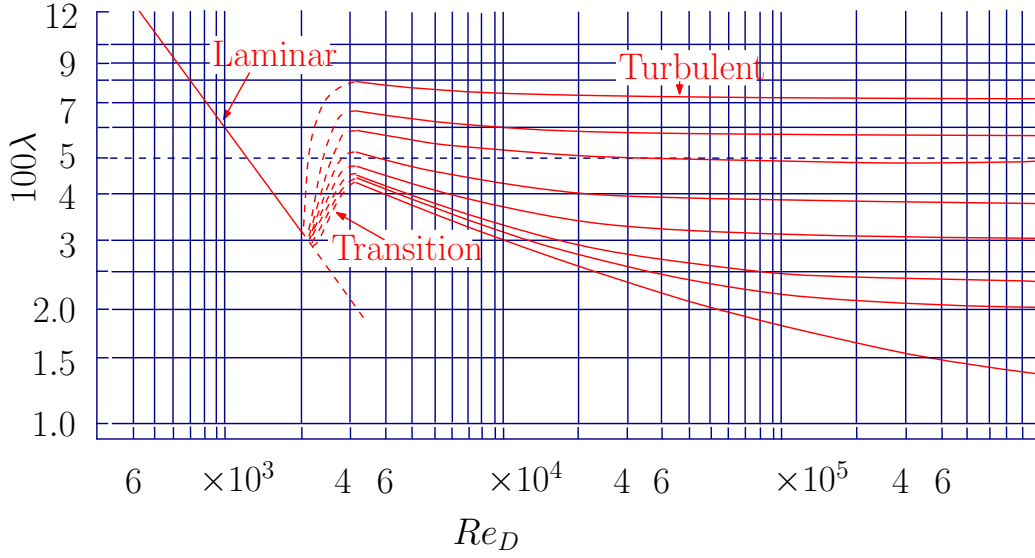


Figure 2.2: Frictional resistance in pipes.  $Re_D$  is defined as the diameter based Reynolds number, and  $\lambda$  is the frictional resistance

	Experiment	$\gamma Re_\theta$	$k - \omega$
$C_d$	7.98E-3	8.41E-3	1.36E-2
$C_l$	4.64E-1	4.65E-1	4.09E-1
Error% $C_d$	-	5.389	70.426
Error% $C_l$	-	0.2155	-11.8534

Table 2.1: Configuration:  $\alpha = 0^\circ$  and  $h = 100\% c$

	Experiment	$\gamma Re_\theta$	$k - \omega$
$C_d$	1.03E-2	1.04E-2	1.55E-2
$C_l$	8.75E-1	8.27E-1	7.63E-1
Error% $C_d$	-	0.775	50.194
Error% $C_l$	-	-5.486	-12.800

Table 2.2: Configuration:  $\alpha = 4^\circ$  and  $h = 100\% c$

Comparing the CFD results to the experimental results obtained by M.R. Ahmed et al. [13], it is observed how the transition model yields much accurate results compared to the turbulence model due to the presence of laminar boundary layer. As can be observed in figures 2.3 and 2.4, where a contour plot of the kinetic energy computed by the transition ( $\gamma Re_\theta$ ) and the turbulent model ( $k - \omega$  SST) is shown, it is possible to observe how the modelling of the transition yields a dramatic difference.

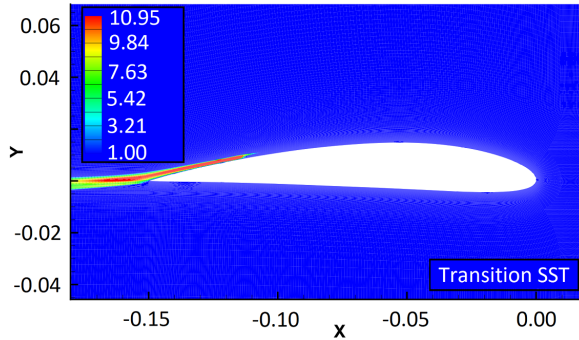


Figure 2.3: Kinetic energy [J/Kg] over the airfoil at an angle of attack  $\alpha = 0^\circ$  and a height equal to the airfoil chord with moving floor. Simulation performed using the  $\gamma Re_\theta$  transition model.

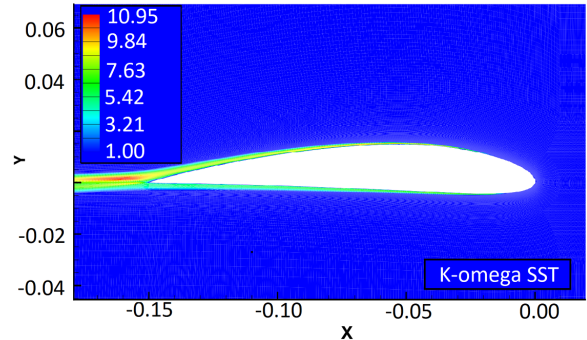


Figure 2.4: Kinetic energy [J/Kg] over the airfoil at an angle of attack  $\alpha = 0^\circ$  and a height equal to the airfoil chord with moving floor using the  $k - \omega$  SST turbulence model.

It is worth mentioning that the transition point in these simulations<sup>4</sup> was accurately captured by the transition model as can be seen in table 2.3.

$\alpha$	Exp [-]	Sim [-]	Error [%]
0 deg	0.73	0.74	0.91
4 deg	0.55	0.57	4.22

Table 2.3: Comparison between the experimental normalized location on the upper surface ( $x/chord$ ) where boundary layer transition was detected [13] and location obtained by the  $\gamma Re_\theta$  simulation.

The case of a Shell Eco Marathon UrbanConcept is in between both cases. While it is not as skin drag dependent as an airfoil, its percentage of pressure drag is much lower when compared to a passenger car. The use of a transition model will allow to reduce this source of error, as well as to obtain an approximation of the point at which transition from a laminar to a turbulent boundary layer is occurring.

<sup>4</sup>The laminar to turbulent transition point was obtained by joint observation of the intermittency graphs and the kinetic energy plots.



## 2.1.2 Boundary conditions

The simulations performed in this work could be grouped into two kinds of simulations:

- Still road conditions
- Rolling car

On the one hand, the still road conditions present a wind tunnel-like situation in which the track is represented by a fixed wall, and the wheels do not turn. Due to the non-slip condition of the floor, a boundary layer is built up before reaching the car and will affect the flow characteristics as shown in figure 2.5. On the other hand, the rolling car simulations presents moving track and wheels. Due to the relative speed of the road to the car, no boundary layer is present in the flow before reaching the car. As can be seen in figure 2.6, this kind of simulation presents a more realistic approach, and therefore will have a capital importance in the development of this work.

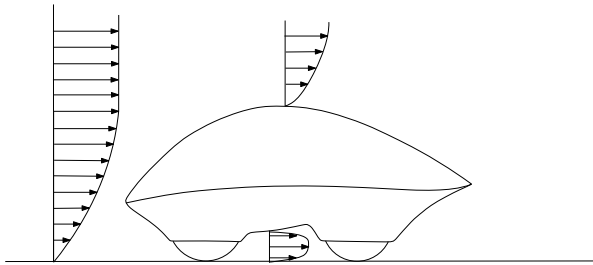


Figure 2.5: Velocity profile detail for the still road condition.

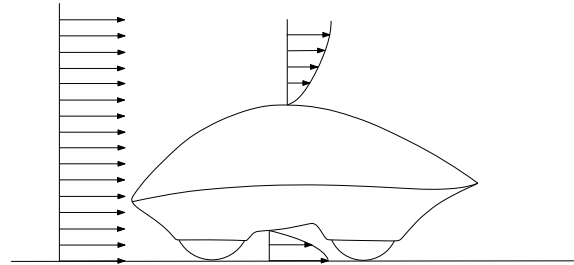


Figure 2.6: Velocity profile detail for the rolling car condition.

These two kind of simulations will allow not only to compare real world to wind tunnel conditions, but also to study the interesting effect of the ground effect and its impact on car aerodynamics.

The studied domain is divided into different named sections. These sections are shown in figure 2.7.

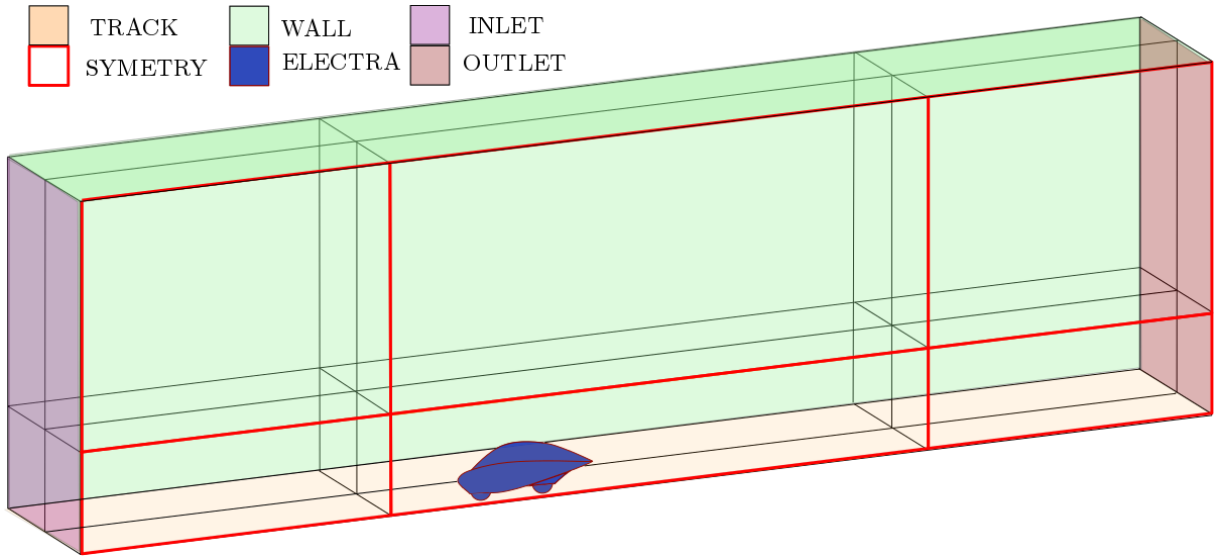


Figure 2.7: Different named sections of computational domain.

For both kind of simulations, a Dirichlet boundary condition is applied to the velocity at the inlet. This allows to fix the velocity inlet. In order to reach this prescribed value of the velocity, the stagnation pressure is recalculated until attaining the desired result.

At the outlet section, the Dirichlet condition is applied to the gauge pressure. It is important to maintain this boundary far from the studied body, as the fixing of the pressure value at this point could modify the flow properties upstream.

For the wall section, a slip wall boundary condition is applied. This boundary condition blocks the air from entering or leaving the study domain by applying a null normal velocity. Due to the slip condition, no shear is caused at these walls.

At the symmetry region, a symmetry condition is applied. This condition has the same effect on the flow as the slip wall, fixing a null normal velocity and removing all shear effects.

Finally, a non-slip wall condition is applied to the Electra and track sections. This boundary condition forces impermeability and zero velocity at the wall. All walls remain stationary for the still road conditions, however, a translational velocity and a rotational velocity are applied to the track and the wheel faces respectively when simulating moving road conditions.

As can be seen in figure 2.7, the domain is subdivided into twelve sub-domains or boxes (eighteen in the case of a full domain simulation). This subdivision of the domain allows the control and use of different mesh types. The central box in which the car is contained,

is discretized through a tetrahedral unstructured mesh (figure 2.8). This type of mesh allows to easily adapt it to multiple geometries in an automatized manner. This type of mesh is automatically created by the meshing software in which the desired restrictions are introduced in order to specify the desired refinement parameters. Although this type of mesh presents multiple benefits, it is necessary to pay attention to its quality. Parameters such as skewness or aspect ratio must be supervised, as high values of these parameters could derive convergence problems.

In the remaining boxes, structured hexahedral mesh was used (figure 2.9). This kind of mesh needs less computations to be constructed than the unstructured one, lowering considerably the time for mesh construction. Also, due to its hexahedral composition, it allows to optimize the number of cells when discretizing a geometry. This structured mesh is directly defined by the number of divisions fixed by the user at the edges of the different sub-domains.

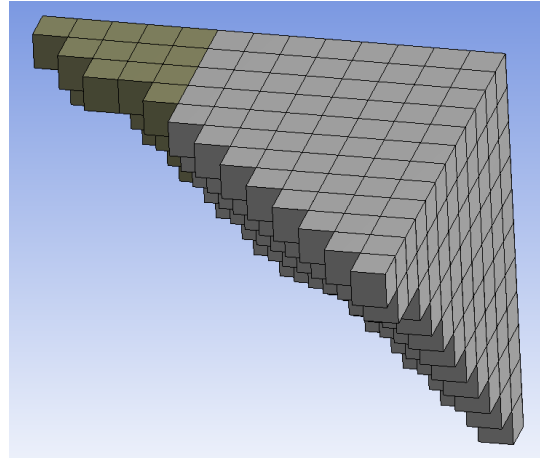
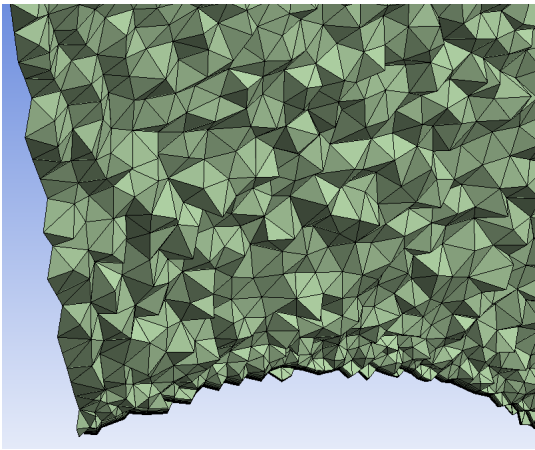


Figure 2.8: Unstructured tetrahedral mesh.      Figure 2.9: Structured hexahedral mesh.

Both types of mesh are connected through a conformal interface, meaning that adjacent cells match their nodes at both sides of the interface. This avoids the need to average data across the interface allowing for a faster and more accurate computation. The conformal connection between the tetrahedral and the hexahedral meshes is performed with the use of pyramids of square base at the unstructured side of the interface.

As already stated before, the modelling of the boundary layer is of major importance, being therefore necessary to refine the mesh at the non-slip wall elements, elements at which a boundary layer will appear. In this study these sections are the Electra and the track. Taking a look at the shape of a boundary layer (figure 2.10), it is possible to observe how the flow speed does not change in a significant manner in the axis parallel to the wall, while it sees a big velocity gradient in the normal axis.

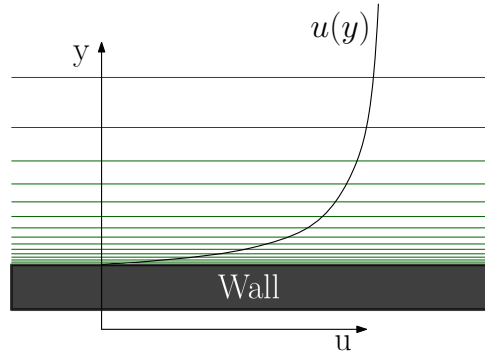


Figure 2.10: Inflation layer mesh detail with visualization of the boundary layer velocity profile ( $u(y)$ ).

In terms of mesh, this is translated as the need of boundary inflation layer. This refinement technique consist on a high refinement in the normal axis in order to capture all variations in the axis normal to the surface while maintaining a coarser discretization in the parallel axis. This yields high aspect ratio elements on the surface of the non-slip wall elements, but due to the low variation of the flow speed in the parallel axis, this technique do not represent a threat in terms of residuals and convergence. This boundary inflation technique was used at the floor and at the Electra’s surface. In order to characterize this inflation layer, the aspect ratio of the first cell, number of inflation cells and growth rate were defined, allowing to accurately control the  $y^+$  at the first cell for each simulation.

### 2.1.3 Cell convergence study

The discretization in cells of the fluid domain can be a source of large errors, it is therefore necessary to verify that its impact on the result is minimum. In order to minimize its influence, a convergence study is performed. The choice of the criterion of convergence is one of the most important steps, as while some parameters may converge quite fast, other more sensitive parameters may show a dependency on the number of cells. In this report, lift and drag coefficients were chosen as convergence reference. Its high sensitivity and major relevance in this report make them the most suitable choice.

The half model with still road condition case at the reference Reynolds number was chosen as starting point for this study. The apparition of the boundary layer in front of the car makes it a more grid dependent simulation than the rolling car conditions. The size of the domain was built following the guidelines given by Marco Lanfrit [20].

As shown in figures 2.11 and 2.12, the  $c_D$  is less grid dependent than the  $c_L$ , which varies around 40% in the studied cell range. Around 7.6 million cells, a fully converged solution is found, being therefore not needed to exceed this number.

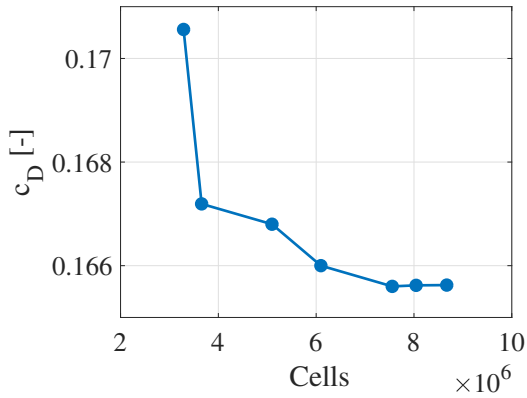


Figure 2.11: Drag coefficient ( $c_D$ ) cell convergence study.

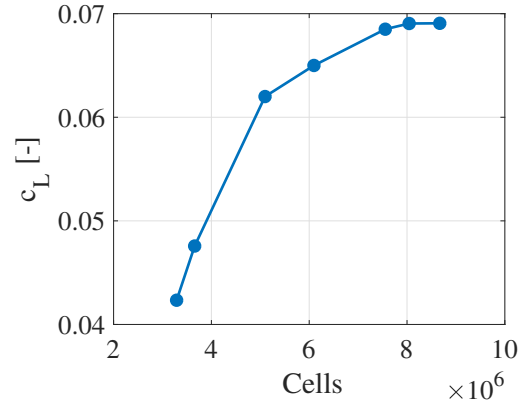


Figure 2.12: Lift coefficient ( $c_L$ ) cell convergence study.

Due to the large number of simulations performed in this work, a good compromise between accuracy and computing time must be done. Each time one simulation is performed, mesh and solution variables information must be stored in such a way they are quickly accessible by the solver. Ansys Fluent stores all this information within the random access memory (RAM) by default. Its high read/write rate allows the software to quickly compute all calculations. However, the large amount of memory needed to store a 3D mesh could yield a larger memory space than the one present in the RAM. In that case, Ansys Fluent swap the heap memory to the defined Window's virtual memory. This means that part of the information previously stored in the RAM, now is stored in the much slower hard disk of the working station. Figure 2.13 shows the time needed by the solver to complete 100 iterations.

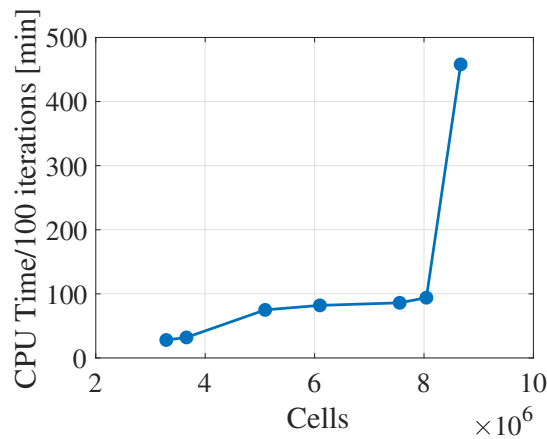


Figure 2.13: Computational time per 100 iterations for different number of cells.

As can be observed in figure 2.13, the increase in CPU time increases smoothly below the 8 million cells mark. Once this point is passed, the effect that the memory swapping has on the performance of the solver is clearly seen, increasing abruptly the computing time. A value between 7.5 and 8 million cells is therefore chosen as reference set up for the simulations performed in this report.

### 2.1.4 Domain convergence study

As the number of cells, the size of the computational domain have a big impact on the obtained results. In order to minimize the impact that the boundary conditions of external walls have on the region of interest (the Electra in this case), these should be as far as possible from it. The increase in the number of cells that this implies, makes it necessary to find the good balance between accuracy and computational demands.

For this study, the rolling car condition was taken as a reference case. In that manner, the influence of the inlet boundary condition will not be masked by the growth of the floor boundary layer, which would be the case for the still road condition. Starting from the guidelines given by Marco Lanfrit [20] and observing the influence in the result of each of the domain parameters, after an extensive study, the domain size was chosen to be  $3.5L$  in front of the Electra and  $6.5L$  behind. The frontal area blockage of the domain (Frontal Domain Area / Electra's Frontal Area) yield a value below 4%. A detailed scheme of the domain size can be seen in figure 2.14.

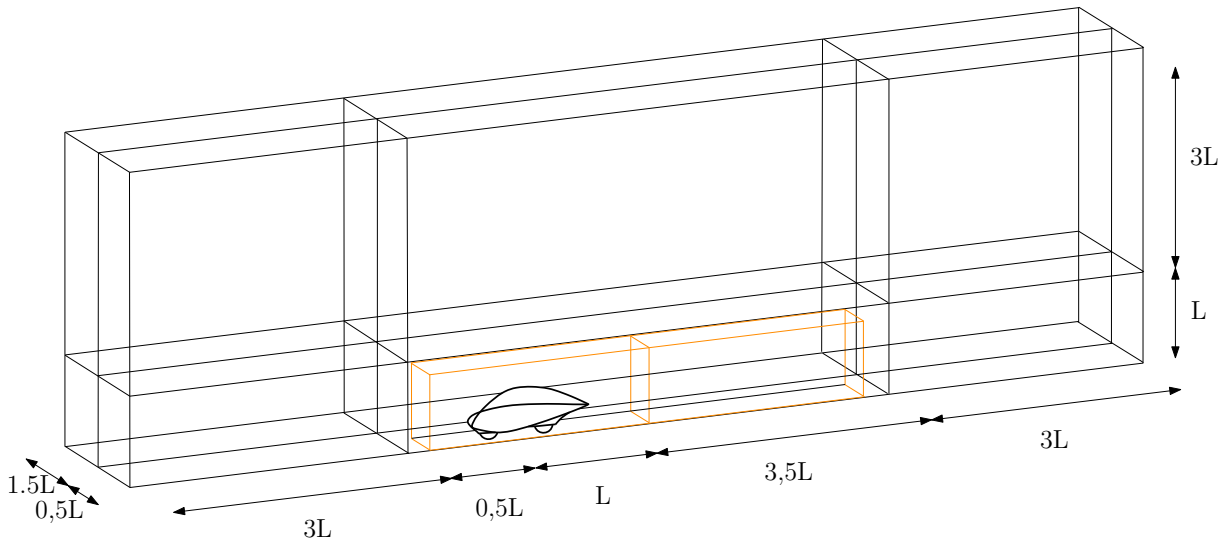


Figure 2.14: Computational fluid domain size. Domain mesh partitioning in black, refinement boxes in orange.

As can be seen the distance from the inlet to the car is much smaller than the distance from the car to the outlet. The same can be derived from the refinement boxes that surround the car. This is due to the effect that the fixed pressure of the outlet boundary condition have on the wake of the car. The car wake is of major importance, as if this is modified, the perturbation could travel upstream and modify the properties of the flow around the car. Another important parameter is the frontal area blockage. Due to the slip wall condition applied to the *Wall* section, an acceleration of the flow is induced due to the reduction in cross sectional area. This phenomenon is graphically explained in figures 2.15 and 2.16.

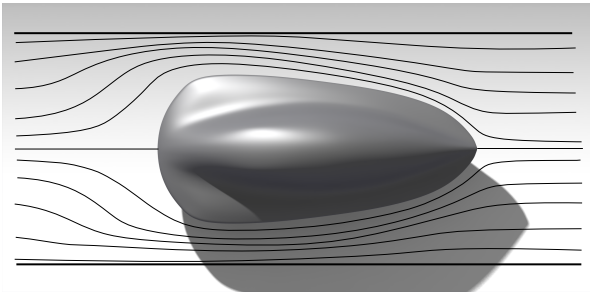


Figure 2.15: Blockage effect of the streamlines with walls surrounding the car.

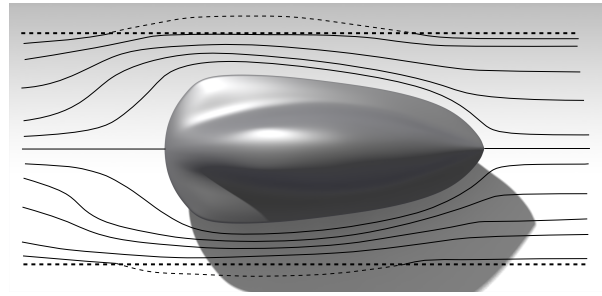


Figure 2.16: Natural streamlines around the car in a non-restricted domain.

As picture 2.15 shows, the flow is not able to quit the fluid domain as it would do in reality (figure 2.16), it is therefore important to maintain these walls far from the region of interest in order to minimize this effect.

The final mesh is shown in figure 2.17. It is possible to observe the use of both types of mesh, the structured in the outer sub-domains and the unstructured one in the car sub-domain. The structured mesh is made up of cubes of 25 cm and an inflation layer near the track section. The unstructured part of the mesh is composed of two refinement boxes (see orange boxes in figure 2.14). The refinement box surrounding the car limits the size of the tetrahedral mesh to 3.7 cm (mesh detail in figure 2.18), and the wake refinement box limits their size to 9 cm. These values allows for a good performance/accuracy ratio. In order to control the accuracy of the solution at the car surface, the size of the tetrahedral elements are limited to a maximum edge size of 1.3 cm, and due to the complexity of the wheels and track inflation layers merging, a maximum edge length of 0.3 cm is imposed at the Electra wheels. Finally it is also possible to observe the inflation layers at the track and Electra sections in figures 2.17 and 2.19.

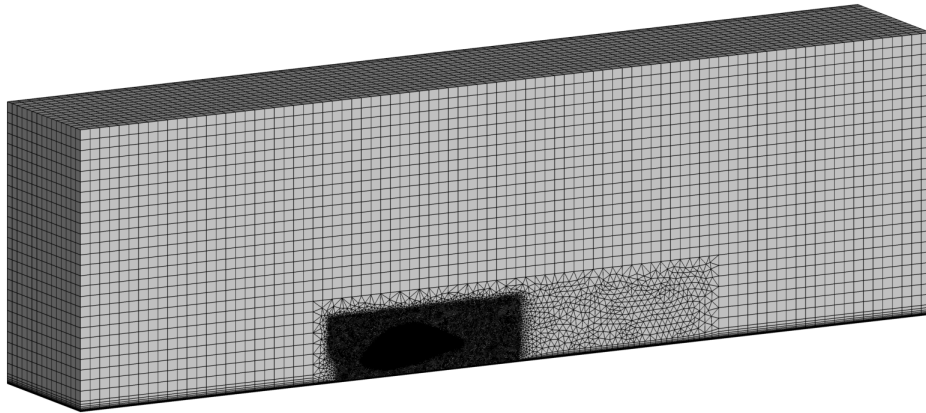


Figure 2.17: Half domain final mesh seen from the symmetry side.

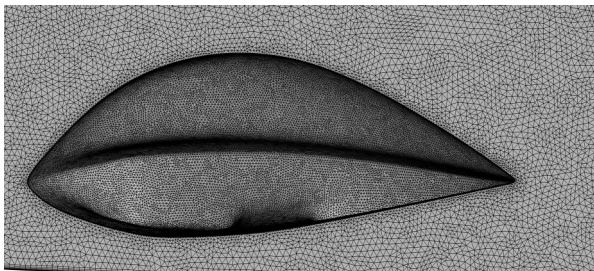


Figure 2.18: Refinement box and Electra detail of the half domain final mesh seen from the symmetry side.

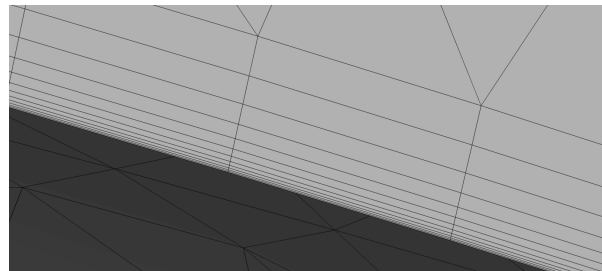


Figure 2.19: Detail of the inflation layer at the top surface of the Electra in half domain final mesh seen from the symmetry side.

### 2.1.5 Sensitivity study

In a CFD simulation, parameters such as the turbulent intensity, viscosity ratio and intermittency must be defined. The order of magnitude of these parameters can be known from literature, but knowing the exact values that would allow to accurately model the studied application is some times impossible or difficult to obtain. Therefore, it is always important to understand the impact of the variation of each of these parameters.

These parameters characterize the flow at the boundaries of the performed simulation, allowing to replicate different kind of flows. External flows, internal flows or flows inside a wind tunnel present different properties which are defined within the CFD model through these parameters.



- Intermittency

The intermittency  $\gamma$  is a parameter with values ranging between 0 and 1 (being 0 fully laminar and 1 fully turbulent), used to monitor if the flow is laminar, turbulent or transitional. As one could notice, this parameter only applies to the  $\gamma Re_\theta$  model, as the other used models only model turbulent flows.

Even though the flow inside a wind tunnel normally shows a low turbulent intensity, the flow must be treated as fully turbulent at the inlet [26]. Therefore, a value of 1 is used both at the inlet and the outlet.

- Turbulent viscosity ratio

The turbulent viscosity  $\beta$  shows the ratio between the turbulent viscosity,  $\nu_t$ , and the molecular dynamic viscosity  $\nu$ . For the case of a wind tunnel,  $\beta$  usually has values between 1 and 10. The impact of this variable on the final result is minimal (a change in drag below 0.5% and a change of 1.6% in lift). A value of 2.5 is chosen at the inlet and the outlet to perform the simulations of this report.

- Turbulence intensity

The turbulent intensity  $I_t$  is defined as the ratio of the root mean square perturbation of the flow and its average velocity. As its name indicates, this parameter shows the intensity of the turbulence present in the flow. The values found in wind tunnels are much lower than those found in internal flows being possible to reach even an intensity of 0.05%. Values between 0.05% and 5% were tested, yielding less than 1% variation in drag and less than 2% in lift. Due to beforehand estimations performed at the wind tunnel, a value of 1% is used.

As shown in this study, the result of these simulations is stable with respect to these parameters, permitting to perform the simulations with confidence in the results even before obtaining the experimental value of the parameters.

### 2.1.6 Solver set up

For this work, a pressure-based solver with an absolute velocity formulation was used. The aforementioned solver works by solving a pressure correction equation. This equation is derived from the mass conservation and the momentum equation, so that the velocity field satisfies continuity. All this is performed with the use of a projection method-type algorithm. Due to the non linear and coupled nature of the governing equations, the solution is found iteratively until convergence is reached [21].

In the scope of this thesis, the use of a coupled solver was preferred to the use of a segregated solver. As can be seen at the flowcharts shown in figure 2.20, the coupled

solver solves the momentum and pressure-based continuity equations together instead of solving the momentum equation and pressure correction equations separately as it would be the case for a pressure-based segregated algorithm [21]. Due to this coupling, the memory requirement of this solver increases by nearly 2 times compared to the segregated algorithm, since all pressure-based continuity and momentum equations must be accessible in memory when solving for the velocity and pressure fields [21]. However, this procedure increases the robustness of the simulation by completely eliminating the approximations associated with a segregated solution, which can highly perturbate the convergence rate [27].

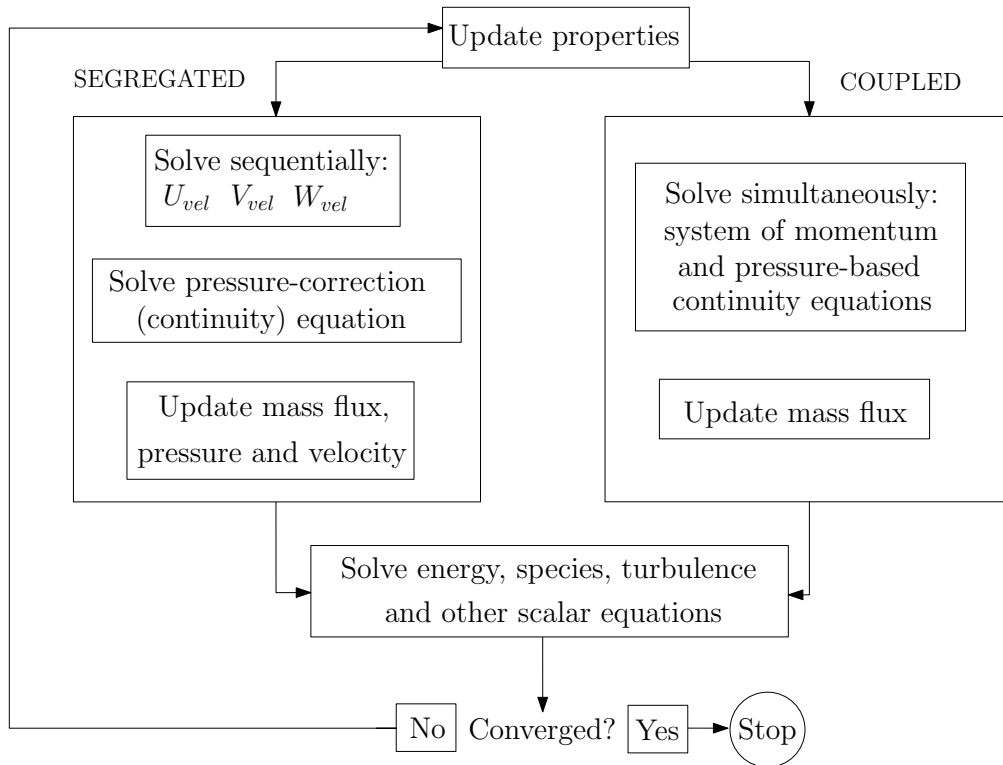


Figure 2.20: Flowchart comparison of a coupled and a segregated pressure-based algorithm.

In order to improve the performance of the solver, ANSYS Fluent uses its coupled Algebraic Multigrid (AMG) to solve the linear systems obtained from the implicit discretization.

To understand how this method works, we will commence by a simple example<sup>5</sup>. Taking the 1D Poisson equation with boundary conditions:

<sup>5</sup>Example taken from [28]

$$\frac{d^2u}{dx^2} = \sin(ki\pi x) \ ; \ u(0) = u(1) = 0 \tag{2.1.3}$$

and solving of  $u(x)$ , one obtains:

$$u(x) = -\frac{\sin(k\pi x)}{k^2\pi^2}. \tag{2.1.4}$$

As can be observed,  $k$  plays the role of a wave number. Discretizing with a second order central finite difference on a 1 dimensional mesh with a uniform spatial discretization with a size  $h$ :

$$u_{i+1} - 2u_i + u_{i-1} = h^2 \sin(k\pi x_i) \ ; \ u_0 = u_N = 0 \tag{2.1.5}$$

and solving by Gauss-Seidel, it is possible to observe how the value of the  $k$  affect the rate of convergence (figure 2.21).

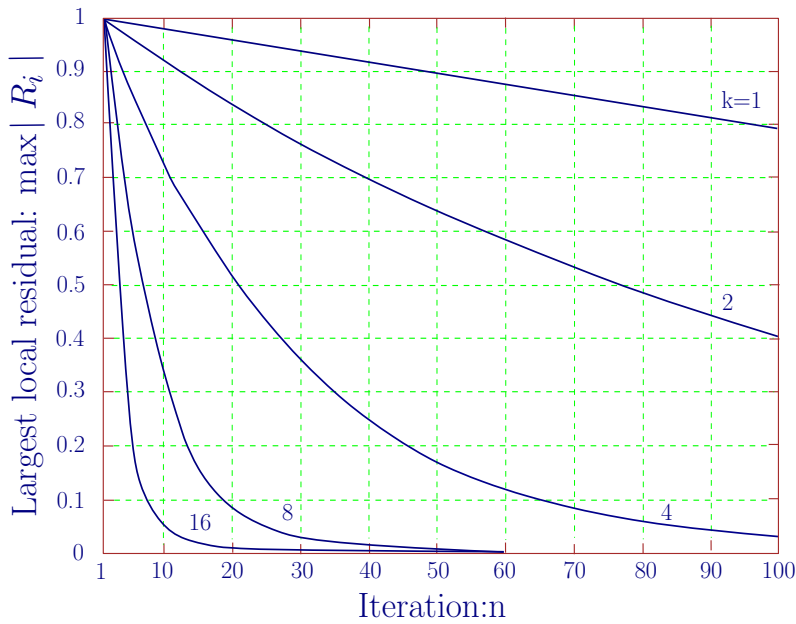


Figure 2.21: Largest local residual of the second order central finite difference discretized 1D Poisson equation with boundary conditions solved by using Gauss Seidel.

This is a simple example at which the frequency can be directly modified by the user. This is not the case for real life CFD applications, where solutions are constituted out of multiple sources of diverse frequencies, causing a quick convergence of the high frequency part of the solution, but a slow decay of the low frequency source. This causes what could be named as a stall of convergence. In order to avoid this, it is possible to vary the grid refinement. Varying the refinement of the mesh, one could change the perception of this variation from one point to another as shown in figure 2.22.

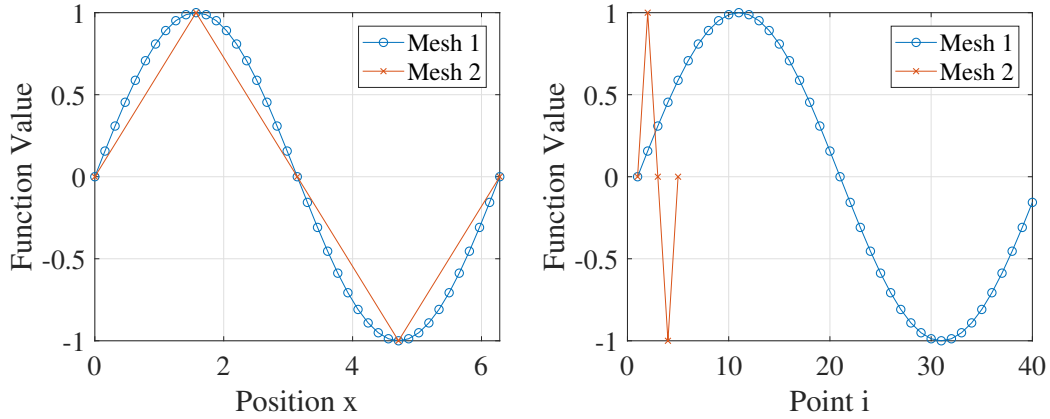


Figure 2.22: Comparison of two different spatial discretizations of a sinusoidal function and the value seen by each discretization point.

As shown in figure 2.22, by changing the resolution of the grid, the rate of change from one mesh node to another can be hugely changed, turning a slowly varying function into a fast varying function. It is therefore possible to reduce the convergence stall by transferring the problem to a coarser grid [1].

Instead of performing this computation with only one fine mesh and one coarse mesh, this method is optimized by using a hierarchy of coarser grids and different cycles. Two basic examples of existing cycles are the V-cycle and the W-cycle, shown in figure 2.23. The V cycle requires less computations than the W cycle, however it shows worst convergence properties.

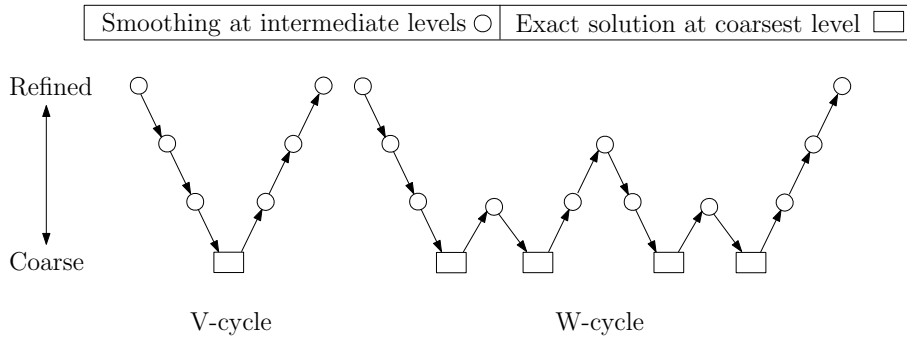


Figure 2.23: Graphic representation of the multigrid V and W cycles. (Adapted from [1])

Unlike a normal multi-grid method, the AMG generates the coarse levels by directly modifying the coefficient matrix without the need to modify the mesh used to discretize the model [21]. In order to optimize the performance of the AMG, an F cycle (figure 2.24)

is used. This cycle is a combination of the previously presented V and W cycles. This cycle presents roughly the same convergence properties as the W cycle but with a lower computation demand [21].

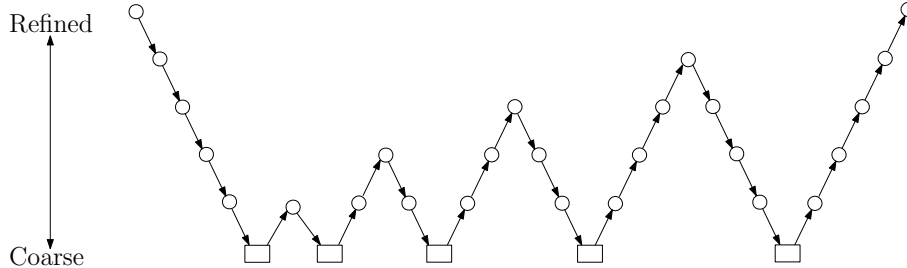


Figure 2.24: Graphic representation of the multigrid F cycle.

### 2.1.7 Numerical validation: The Ahmed body

Until now all variables involved in the numerical simulation were studied and optimized to the available computational capabilities, but how does it perform when compared to a well documented case? In order to answer this question, the Ahmed Body was taken as verification case.

The Ahmed Body is a simplified car geometry that allows to study common flow structures present in ground vehicle aerodynamics. Due to the large amount of available studies on this geometry, it has become a benchmark for automotive CFD.

The geometry of the Ahmed body is depicted in figure 2.25. As can be seen, the rear slant angle of the wind tunnel model is variable, being possible to observe different flow behaviours and validate CFD simulations for different study cases.

For these simulations, the same parameters as the already stated for the Electra have been used, and the mesh and domain parameters have been scaled consequently in length, width and height to the size of the Ahmed Body. For this validation, the experimental results obtained by S.R. Ahmed et al.[2] for different slant angles at a free-stream velocity of 60 m/s have been used.

Two validation studies have been performed, one with a wall function model, and another with the low Reynolds transition model. The tested wall function model have been the  $k - \varepsilon$  realizable model. This is the model advised by M. Lanfrit [20] when using wall functions due to its stability, fast convergence and good results in industry. For the near wall modelling, non equilibrium wall functions are used. For the low Reynolds model, the  $\gamma Re_\theta$  transition model have been chosen as validation model. The obtained results are shown in figures 2.26 and 2.27. As in the paper by S.R Ahmed et al. [2], the total drag is shown as the decomposition of pressure and skin friction drag.

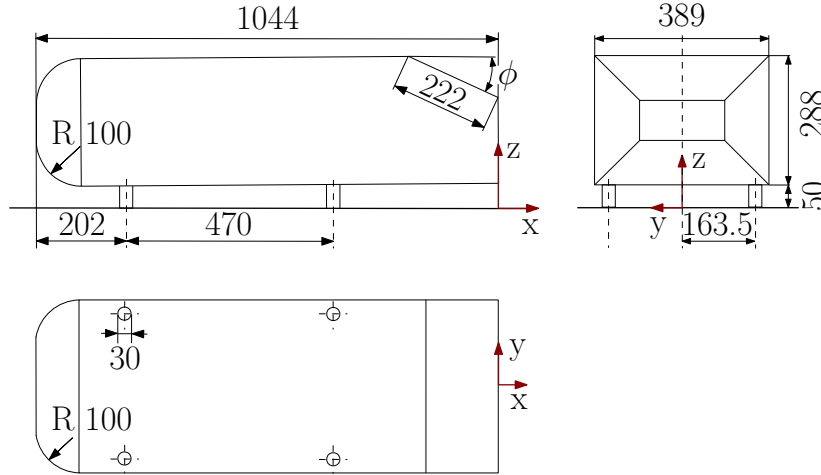


Figure 2.25: Geometry definition of the Ahmed Body. Dimensions in mm.

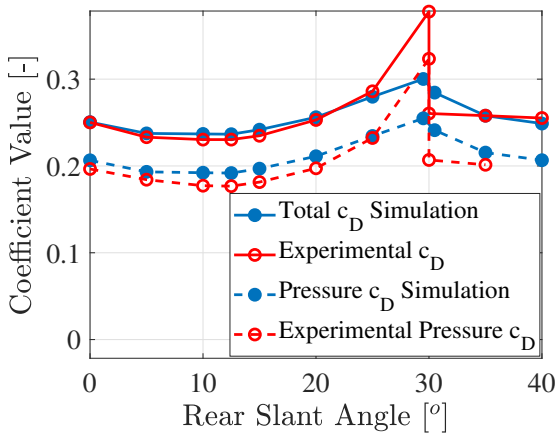


Figure 2.26: Experimental and numerical comparison of the Ahmed Body total and pressure drag using the  $k - \epsilon$  realizable turbulent model with non-equilibrium wall function modelling.

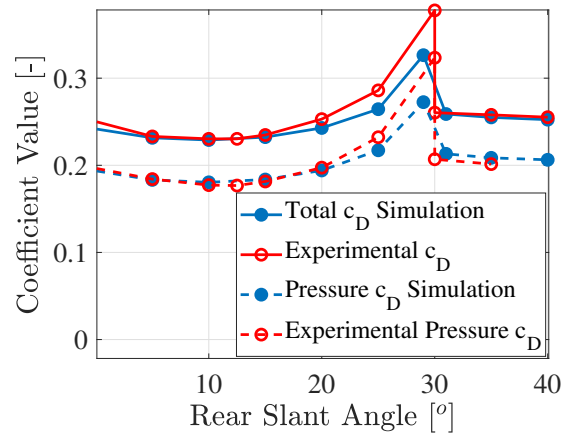


Figure 2.27: Experimental and numerical comparison of the Ahmed Body total and pressure drag using the low Reynolds  $\gamma Re_\theta$  transition model.

As can be seen in figure 2.26, the wall function version of the  $k - \epsilon$  model does performs well for most of the tested cases. However it is worth noticing the overestimation of the pressure drag coefficient and the noticeable problems to capture the drag crisis observed at  $30^\circ$ . These results show how the overall trend of the drag behaviour is captured, however, this model can have some problems capturing boundary layer properties as could be seen at the simulations near  $30^\circ$ .

Taking a look now at the results obtained with the  $\gamma Re_\theta$  transition model (figure 2.27), it is directly noticeable how the transition model captures the pressure drag in a much more accurate way, as well as the drag crisis present at  $30^\circ$ .

A visual verification of the flow 3D structures was also performed. Both models were capable of representing the same flow characteristics as S.R Ahmed et al. made on their paper. Figures 2.28 and 2.29 show an example of this 3D structure matching.

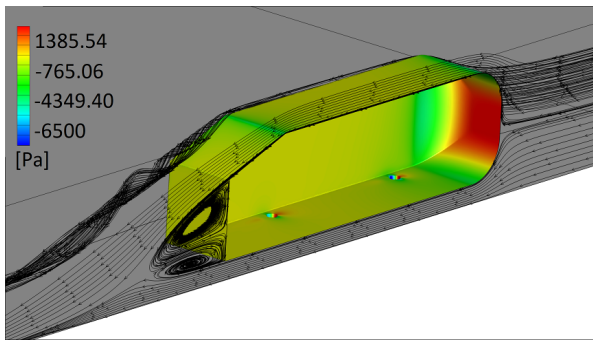


Figure 2.28: Streamlines and pressure contour plot of the Ahmed Body at 60 m/s and a slant angle of  $\phi = 20^\circ$ . Numerical simulation performed with the  $k - \epsilon$  realizable model with non equilibrium wall functions.

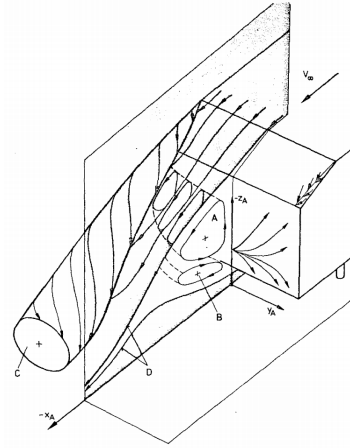


Figure 2.29: Detail of the wake horseshoe vortex and recirculation bubbles depicted by S.R. Ahmed et al. in their paper [2].

On the one hand, these results show how even if the wall function model could capture the overall shape of the 3D structures present at the flow surrounding the car, it had some non-negligible problems when capturing the detachment of the boundary layer or estimating the pressure to friction drag ratio. For a more complex geometry such as the Electra, this could be an important problem, and therefore its results must be attentively studied and checked by the use of other turbulence models. On the other hand, while the low Reynolds turbulence model also had some problems at the angles of 20 and 25 degrees, it presents an accurate representation of the real phenomena, obtaining much precise pressure drag results and capturing the drag crisis present around  $30^\circ$ .

The obtained results are in agreement with other scientific publications. Some examples are the paper by Y. Liu and A. Moser [29], in which multiple turbulence models were used, obtaining similar error magnitudes. In this paper it is also possible to observe the huge influence that the chosen turbulence model can have on the result. Some papers also reference themselves to the problems seen at slant angles near  $30^\circ$  such as the one by Corallo et al. [30]. It is worth mentioning that the drag crisis observed by S.R. Ahmed

et al. [2] is so sensitive to boundary conditions that there is no consensus in the scientific community. While some affirm that this drag crisis takes place at exactly  $30^\circ$  ([2], [31]), others declare that this drag crisis takes place between slant angles of 25 and 35 degrees([32], [33]).

## 2.2 Experimental methodology

Numerical results allow to have a complete vision of the studied flow, however, the modelling of the turbulence can derive into erroneous results. In order to validate these simulations, experimental data is always necessary as it approaches the engineer a step closer to reality.

### 2.2.1 Wind tunnel facility and wind tunnel model

All experimental tests were carried out at the ULiège's wind tunnel lab. This subsonic wind tunnel built at the end of 1999 by the German company TLT allows open and close loop configurations. For the tests performed, the close loop configuration shown in figure 2.30 was used.

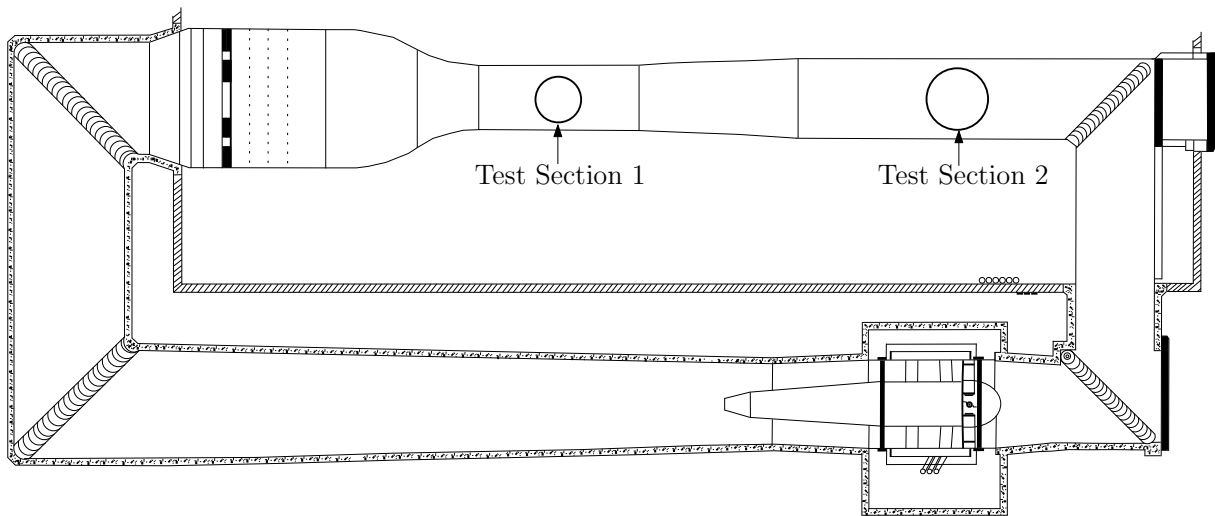


Figure 2.30: ULiège's subsonic wind tunnel drawing for the used close loop configuration. (Adapted from [3])

Test section 1, or Aeronautic/Automobile test section, was used for the performed experiments. With its cross section area of  $2 \text{ m} \times 1.5 \text{ m}$ , it allows to test models with a frontal area lower than  $0.3 \text{ m}^2$  with a speed range that goes from 2 to 60 m/s [3] and a turbulence level of 0.15%.



These experiments were carried out with a 1:4.6 scale polyamide car (figure 2.31). This car represents the simplified CAD of the real car in which only its idealized bodywork surface is taken into account and the wheels are simplified as a fixed non-slip wall, where the part of the wheel that remains inside the bodywork is neglected. This simplified configuration allows to focus on the main characteristics of the flow around the car. The scale of the car was chosen as a compromise between 3D printing capabilities and good Reynolds control. A smaller model would also induce larger errors due to the presence of the boundary layer created by the plate below the car as will be later explained. In order to represent the same  $Re_{L_{ref}}$  at the wind tunnel, a speed of 31.8 m/s must be used, which represent an adequate speed for the used test section.

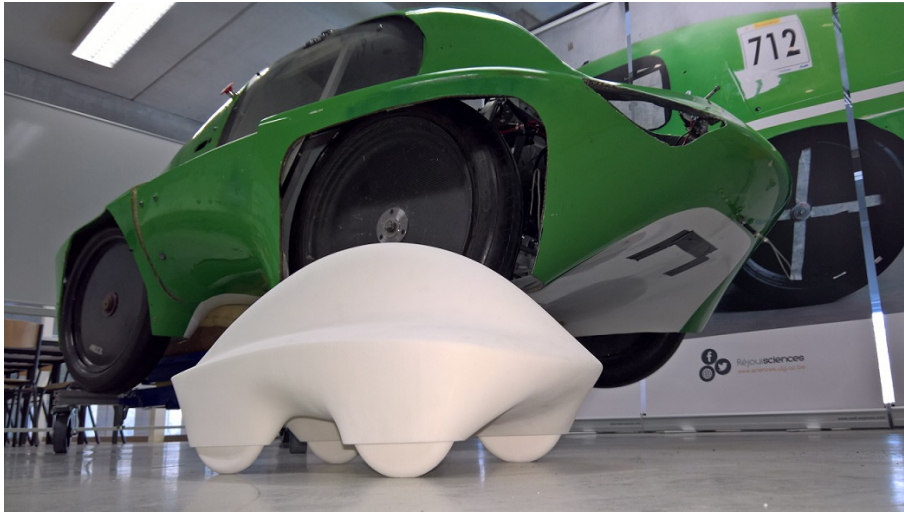


Figure 2.31: Polyamide 3D printed scale model and the Electra car.

In order to eliminate all external imperfections of the 3D printed car, an iterative process of external painting coating and sanding was performed, obtaining a smooth surface. The quality of the surface could play an important role in drag due to the skin friction that could be derived from surface roughness.

## 2.2.2 Force test

The aim of this test was to capture the lateral forces acting on the car at different conditions where speed and angle were changed. In order to get this information the car was mounted on top of an ATI Omega 160 sensor. This sensor allows to obtain three axial measurements for the forces and moments at 200 Hz permitting to obtain good temporal resolution, however, due to the importance of drag in this study, the entire set-up was focused in the obtaining of accurate  $x$  and  $y$  readings, allowing to reduce set-up complexity.

A metal plate of 60 cm in diameter and 1.5 cm thick was used as interface between the force sensor and the car model. The car was attached to the metal plate by four screws mounted on each of the wheels, this simplifies the mounting complexity permitting accurate drag ( $x$  axis) and lateral force ( $y$  axis) measurements. However the lift, and therefore the moments, would yield spurious results due to the plate-car attachment. This entire set up was able to rotate  $\pm 90^\circ$ , enabling the simulation of crosswind conditions. Due to the temporal nature of the measures captured by the sensor, its time consistency was verified on each of the performed tests by computing the variation of the forces average as a function of time. Sometimes a drift in the measurement value was observed, being in that case necessary to repeat the test for optimal results. A duration of 1 min was proven to be enough to obtain accurate results.

In order to protect the metal plate from frontal contact with the flow and avoid the big discontinuity that the metal plate would induce near the scaled model, this set up was surrounded by a fixed mounting made of wood. The fixed set up had a rectangular shape that occupied the entire width of the wind tunnel vane, with a length of 1.3 m and a thickness of 3 cm. This set up was carefully built in order to have upper part of the central structure and the surrounding one at the same level in order to reduce flow perturbations. A schematic representation of the set up can be seen in figure 2.32.

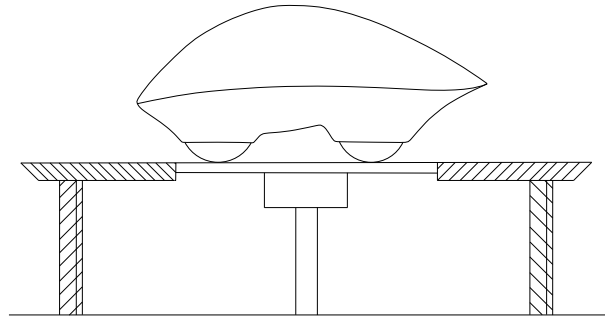


Figure 2.32: Schematic view of the initial wind tunnel set up.

The first tests performed with this set up, which included a Reynolds dependency study at  $0^\circ$  of angle of yaw<sup>6</sup> and an angle dependency study at 25 m/s<sup>7</sup>, showed to be unsatisfactory. High levels of noise and unexpected average coefficient values were obtained as shown in figures 2.33 and 2.34.

<sup>6</sup>The aerodynamic characteristics of the car at an angle of attack of  $0^\circ$  were tested at different speeds ranging from 5 to 35 m/s

<sup>7</sup>The aerodynamic characteristics of the car with a free stream flow velocity of 25 m/s were tested at multiple angles of attack ranging from -30 to 30 degrees.

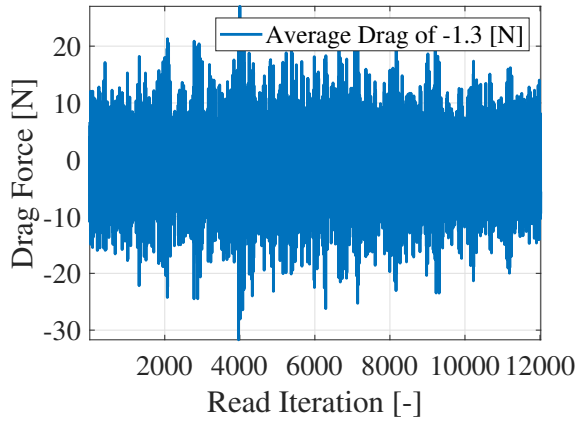


Figure 2.33: Drag force measured by the ATI Omega 160 at 200 Hz with the initial wind tunnel set-up at 30 m/s and a yaw angle of  $0^\circ$ .

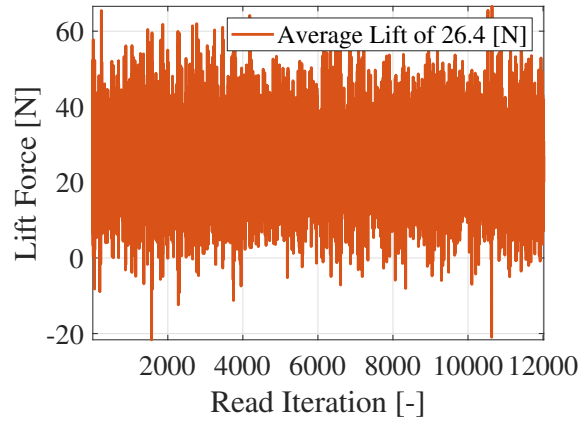


Figure 2.34: Lift force measured by the ATI Omega 160 at 200 Hz with the initial wind tunnel set-up at 30 m/s and an angle of yaw of  $0^\circ$ .

As observed in figures 2.33 and 2.34, extremely large noise was captured by the sensor, and the average values do not match what could be expected in car aerodynamics. The obtained values would yield a  $c_D$  of 0.036, which means 25% less drag than the world record braking Eco-Runner VI.

After these results, the set-up was carefully studied in order to find all the possible sources of errors.

- Metal plate interface: the difference in thickness of the metal plate (1.5 cm) and the surrounding wood plates (3 cm) could induce some aerodynamic instabilities, which mixed with the high inertia introduced by the weight of the metal plate and the difference in radius between the plate (60 cm) and the sensor supporting it (16 cm) could be the cause for some of the high measured level of noise at high speeds.

In order to reduce this effect, the metal plate was replaced by a much lighter wood plate, decreasing the inertial effect that the aforementioned plate could be inducing.

- Turbulence created by lower metal structure: even though the wood structure surrounding the sensor is completely smooth on its upper part, it is not the case for the lower part. The structure made up of metal profiles that attaches the wood structure to the wind tunnel is exposed to the free stream air. The presence of these squared metal profiles could be inducing high energy vortices that would be directly impacting the lower side of the plate sustaining the car model.

To prevent these separation vortices from buffeting the car-sensor mounting, it was enclosed inside a wood box, assuring that no lower aerodynamic disturbance was captured by the Omega 160.

- Instrument calibration: in order to control all the variables playing a role in the measurement, calibration masses were added at different locations at the  $x$  and  $y$  axes in order to observe the effect of different loadings on the resultant measurements. The sensor reported correct values, however it was observed that once the calibration mass was decentralized from the center of the sensor, parasitic force measurements started appearing in the axis in which the mass was being displaced. A graphic representation of this effect can be seen in figure 2.35.

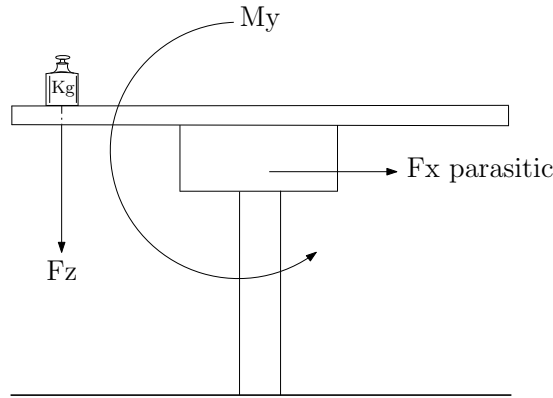


Figure 2.35: Graphic representation of the parasitic horizontal force that appears when decentralising the calibration mass.

This effect was found to be linear ( $F_{induced} = k \cdot M$ , where  $k$  is a constant derived from the mass calibration tests), being possible to easily take this effect into account. Figures 2.36 and 2.37 show the values obtained for different mass positions at the  $x$  and  $y$  axes.

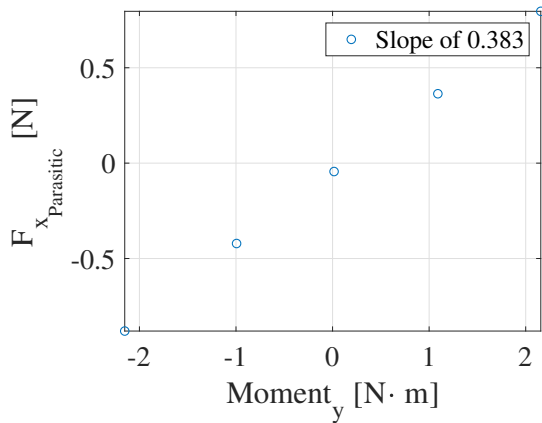


Figure 2.36: Parasitic force appearing in the x axis as a function of the applied moment on the y axis. Test carried out by moving a calibration mass of 0.5 kg on the x axis.

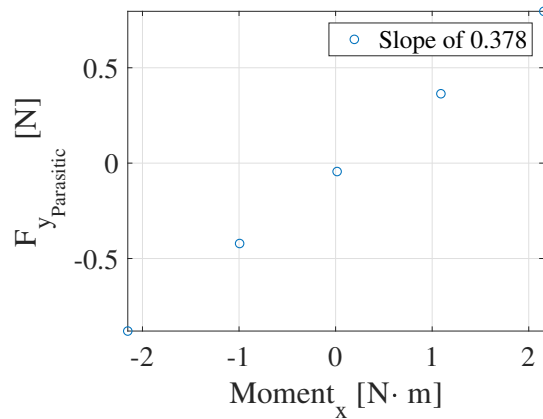


Figure 2.37: Parasitic force appearing in the y axis as a function of the applied moment on the x axis. Test carried out by moving a calibration mass of 0.5 kg on the y axis.

As can be seen the constant  $k$  presents similar values for both horizontal axes yielding 0.383 for  $F_{xParasitic}$  and 0.378 for  $F_{yParasitic}$ .

In order to check the  $F_x$  and  $F_y$  readings of the sensor, the entire sensor + interface plate mounting was fixed horizontally in order to be able to apply the calibration masses in these directions. The sensor readings were satisfactory and no apparent parasitic effect was found.

The aerodynamic properties of the central plate itself also affect the obtained measurements, in order to get rid of this effect, a Reynolds dependency test of the plate alone was carried out, obtaining an approximative value of the aerodynamic forces acting on the plate. This contribution was subtracted from the final force values, being possible to obtain a cleaner image of the aerodynamic properties of the car.

- Wind tunnel blockage: the presence of the entire set-up inside the test vane of the wind tunnel generates a decrease in its cross section area. This blockage effect created by the set up induces an acceleration of the flow around the studied body, introducing a difference in the speed seen by the studied body and the one measured by the Pitot tube upstream. This effect is similar to the wall blockage explained in the numerical methodology (figures 2.15 and 2.16).

In order to take this blockage effect into account, a solid blockage correction [34] will be used. This method estimates the difference in speed and adds this difference to the measured Pitot velocity

$$U = U_{\text{inf},u}(1 + \varepsilon_{sb}), \quad (2.2.1)$$

where  $U_{\text{inf},u}$  is the uncorrected Pitot airspeed, and  $\varepsilon_{sb}$  is a correction factor defined as

$$\varepsilon_{sb} = \frac{K_1 V_B}{S^{3/2}}, \quad (2.2.2)$$

where  $K_1 = 0.74$ ,  $V_B$  is the body volume and  $S$  is the test vane cross section area. For the body volume  $V_B$ , the entire set-up structure and the car model were taken into account.

- Possible upper separation of the flow: even though a  $45^\circ$  chamfer was made at the leading edge of the wood plate in order to smoothly redirect the flow towards the lower part of the structure, the unexpected average values could indicate the presence of a recirculation bubble in front of the car, which would dramatically affect its aerodynamic properties. In order to easily visualize the quality of the flow on the wood plate, tuft visualization was used as shown in figure 2.38.

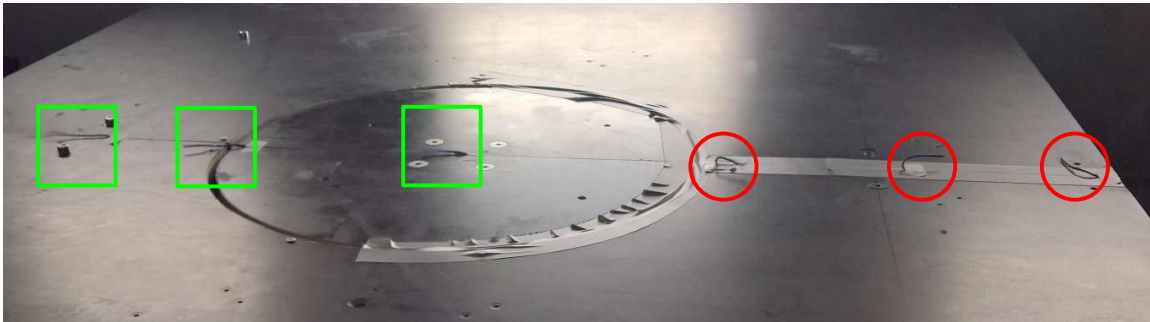


Figure 2.38: Photo of the tuft visualization over the first wind tunnel set up at a speed of 20 m/s. Green squares mark stream-wise pointing tufts, while red circles highlight upstream facing tufts.

As can be seen in figure 2.38, while the rear tufts are directed in the free stream flow direction, the tufts of the frontal part of the plate point in the opposite direction. This confirms the presence of a recirculation bubble in front of the car. This recirculation bubble arrives up to the car position, dramatically changing the properties of the flow passing by the lower part of the Electra (figure 2.39).

In order to reduce this effect in front of the car, a second wood plate of 1 m was added in front of the already existent set-up with the purpose of removing any initial disturbance from the front of the car. In order to mitigate even more the appearance of a recirculation bubble, a new metallic leading edge extension was added.

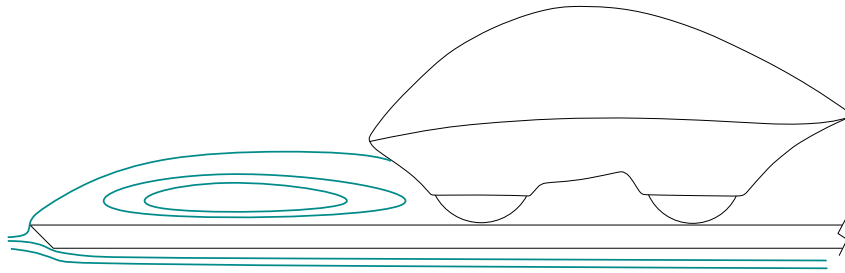


Figure 2.39: Schematic view of the recirculation bubble present at the first wind tunnel set up.

After performing these modifications, new tests were carried out, however still low drag results were obtained. In order to characterize in a more quantitative manner the flow in front of the car, a digital anemometer was placed to measure the flow velocity profile at different locations in front of the car at speeds of 15, 20 and 25 m/s. The velocity profile was normalized for each of the free stream velocities taking the wind tunnel free stream velocity as reference. The obtained results are shown in figure 2.40.

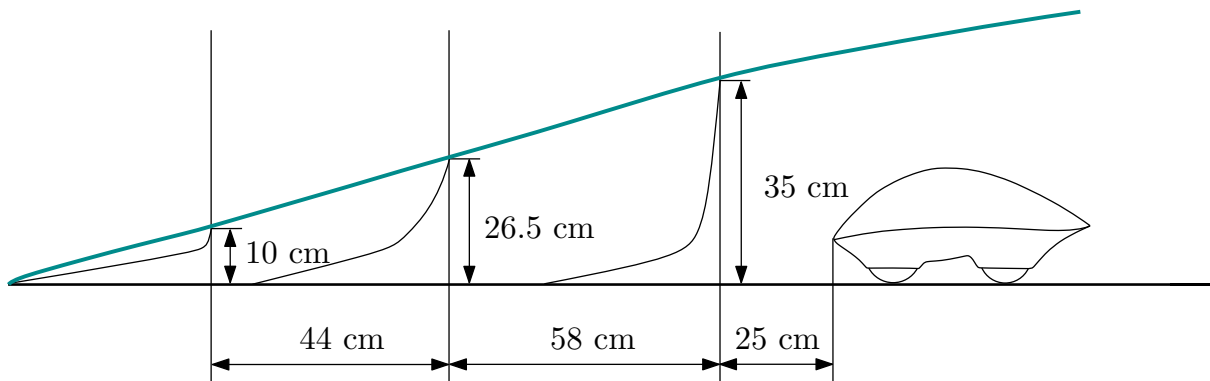


Figure 2.40: Graphic representation of the averaged and normalized velocity profiles obtained with the digital anemometer at a free stream velocity of 15, 20 and 25 m/s.

A boundary layer of 35 cm was present in front of the 3D model, whose height is near 25 cm, reducing considerably the effective flow velocity seen by the car and hence decreasing the drag force. In order to reduce this boundary layer, the added 1 m wood plate was inclined, obtaining an angle of attack of  $-1^\circ$ . This modification helped to decrease the height of the boundary layer and to obtain a fuller velocity profile than the one obtained with the first set-up as shown in figure 2.41. The new velocity profile shows a much more uniform velocity, which even at a height of 1.7 cm, presents a velocity equal to the 80% of the free-stream velocity.

The characterization of the flow in front of the car (figure 2.41) was carried out by the

use of a Turbulent Flow Instrumentation Cobra probe positioned at 25 cm in front of the car at multiple heights . This instrument is a multi-hole pressure probe able to measure the flow velocity in the three axial directions and the local static pressure in real time. Its high accuracy and read speed it is also possible to measure the turbulence intensity. The measured turbulent intensity is shown in figure 2.42.

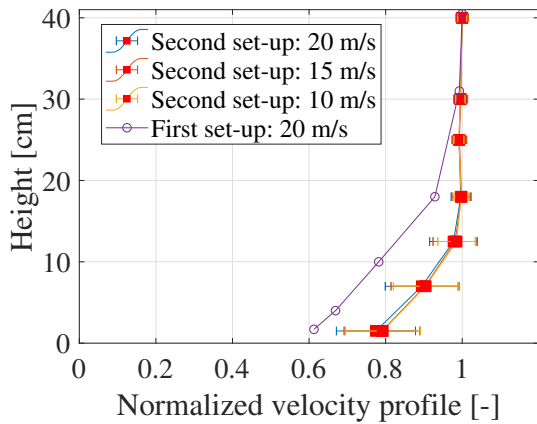


Figure 2.41: Comparison of the averaged and normalized velocity profiles at 25 cm from the car front for multiple heights and speeds. The first set-up measurements were carried out with a digital anemometer while the second set-up measurements were performed with a Cobra probe.

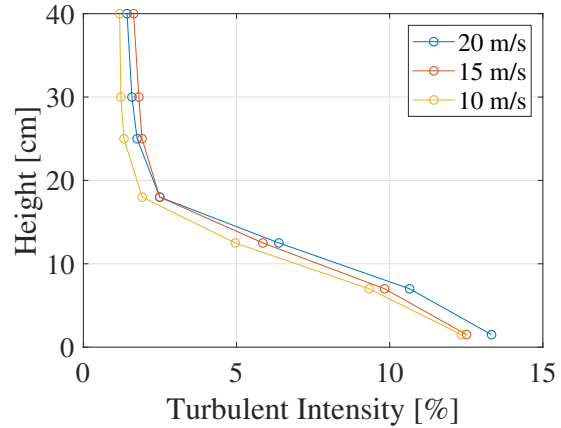


Figure 2.42: Turbulent intensity comparison at 25 cm from the car front for multiple heights and speeds. Measurements taken with a Cobra probe.

Even though the boundary layer has been reduced considerably, its velocity and turbulence effect is still non negligible. In this thesis, its influence will be briefly studied via CFD simulations in section 3.2.

A graphic representation of the final wind tunnel set up is shown in figure 2.43.



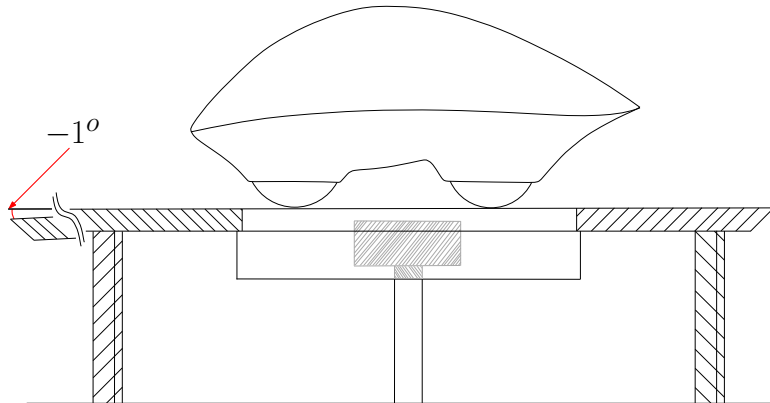


Figure 2.43: Schematic view of the initial wind tunnel set up.

### 2.2.3 Pressure test

Through the force tests, the overall aerodynamic properties of the Electra will be obtained, however, the pressure tests will allow to have a deeper understanding of the flow characteristics around the car.

The pressure distribution over the car was measured by introducing 57 pressure tubes inside the car, which sends the information from the pressure taps to the Dynamic Pressure Measurement System 3101 by Turbulent Flow Instrumentation. This system computes the difference in pressure between each of the pressure taps and a reference pressure. The stagnation pressure measured by a Pitot tube mounted upstream was taken as reference value, obtaining a clean and reliable reference measurement.

Based on preliminary numerical simulations, it was decided to focus on the central part of the car due to its richness in pressure changes and easiness of numerical verification and on the cross section cut which contains the highest vehicle point. This cross section plane also presents high variation of the pressure value, being optimal for numerical verification and flow understanding, as well as particularly interesting for crosswind flow properties. The location of the pressure taps can be seen in figures 2.44, 2.45, 2.46 and 2.47.

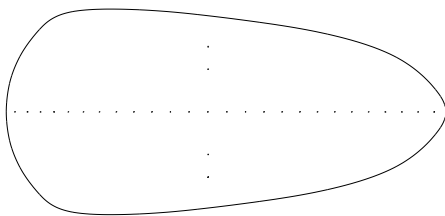


Figure 2.44: Drawing of the upper side of the Electra with pressure taps position.

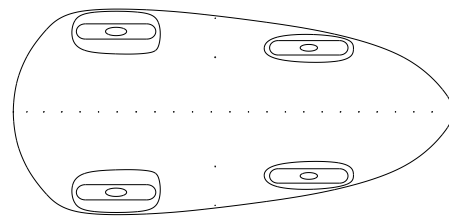


Figure 2.45: Drawing of the lower side of the Electra with pressure taps position.

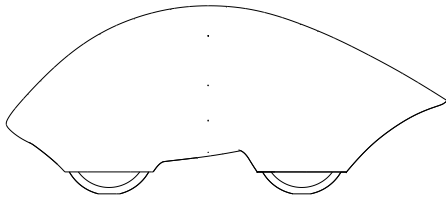


Figure 2.46: Drawing of the left side of the Electra with pressure taps position.

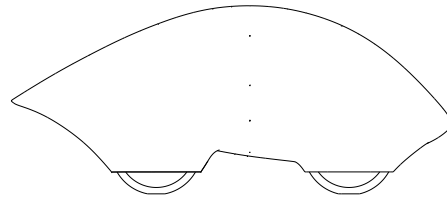


Figure 2.47: Drawing of the right side of the Electra with pressure taps position.

49 pressure taps were located in the middle section of the car. This choice allows for a good resolution, which is needed due to the large amount of interesting data that is captured in this region. One of the pressure taps is located at the stagnation point of the car, serving as a good reference point. 24 pressure taps were located at the top and the bottom part of this middle cut, allowing to capture interesting phenomena such as laminar to turbulent transition, or separation of the boundary layer.

4 pressure taps were located at each side of the cross section cut. These pressure taps together with the 2 pressure taps present at the middle section allows to have 10 reference points at this cut section. This allow not only to better understand the flow around the car and compare it to numerical simulations, but also to capture the asymmetry created on the car surface due to cross-wind.

In order to reduce the aerodynamic effect that the pressure tubes could have on the flow properties of the car, these were evacuated from wheel well closing surface of the four wheels. By doing so, its impact on the flow characteristics at the measurement points was minimal. The wind tunnel pressure test set up is shown in figures 2.48, 2.49, 2.50 and 2.51.



Figure 2.48: Wind tunnel pressure test set-up. Model and tubing detail.

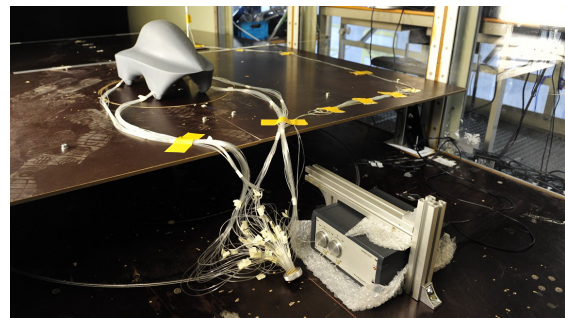


Figure 2.49: Wind tunnel pressure test set-up. Model, tubing and Pressure Sensor detail.

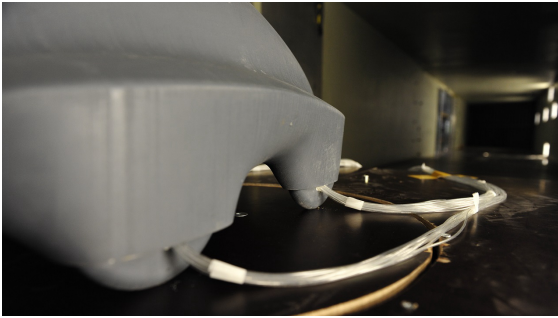


Figure 2.50: Wind tunnel pressure test set-up. Tubing exit detail.

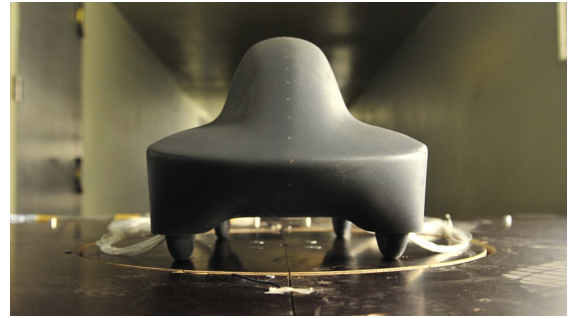


Figure 2.51: Wind tunnel pressure test set-up. Model, tubing and pressure taps detail.

# Chapter 3

## Experimental validation of numerical simulations

Until now, the numerical set up was validated through convergence and sensitivity studies (which allows to reduce the error induced by the discretization of the studied case), as well as comparing its results with a benchmark case (allowing to compare the performance of the numerical set up to the ones used in other studies). With the Ahmed body benchmark geometry, it was possible to observe how even with a good numerical set up, some problems were found at specific cases. Some questions arises: is the tested case well represented by the numerical simulation? Can these results be trusted? These questions will be answered in this chapter through direct comparison between numerical and experimental results. As the goal of this chapter is to compare wind tunnel and numerical results, only still road condition simulations are shown in this section.

### 3.1 Symmetry and steadiness verification

In the methodology section, the symmetry and steadiness of the studied problem were taken for granted, however, would be this the case of the Electra? A symmetric body inside a fluid can induce non-symmetric and unsteady behaviours. Two of the most known examples are the cases of the flow over a sphere and over a cylinder which induces a von Kármán street pattern behind them once a critical Reynolds number is reached.

In car aerodynamics it is not common to find unsteady behaviours for zero angle of yaw conditions, however certain vehicle shapes show these behaviours. Hatchback configuration cars such as the 1996 Ford Ka, the 1997 Mercedes A-Class or the 1999 Audi A2 are known for showing strong unsteady effects [20]. Well known geometries such as the Ahmed body can also eventually show a non-symmetric wake mode as the one studied by J.M. Lucas et al. [35].

In order to verify that the Electra do not present any unsteady or non-symmetric flow pattern, and therefore confirm that the use of RANS equations and half domain

simulations do not introduce any significant error, an URANS<sup>1</sup> simulation is performed making use of a full domain<sup>2</sup>. The use of URANS simulations instead of RANS will allow to take the variations in time into account, and the full domain avoids the zero normal velocity that the symmetry boundary condition imposes at the symmetry plane, allowing for non-symmetric behaviours.

The same mesh parameters as the ones for the half domain mesh were used in the construction of the full domain mesh, yielding a 14 million cells mesh. This cell quantity affected the performance of the simulation, however it was necessary in order to obtain relevant results. In order to help the simulation to trigger any non-symmetric or unsteady behaviour, a non symmetric mesh was used. For the time step, 0.05 s was chosen and a limit of 30 iterations per time step was imposed. This number of iterations per time step allowed for a good convergence of the residuals and the coefficients. A lower time step or higher iteration limit did not show significant variation in the obtained solution.  $\gamma Re_\theta$  model is used. Figure 3.1 shows the convergence of the aerodynamic coefficients.

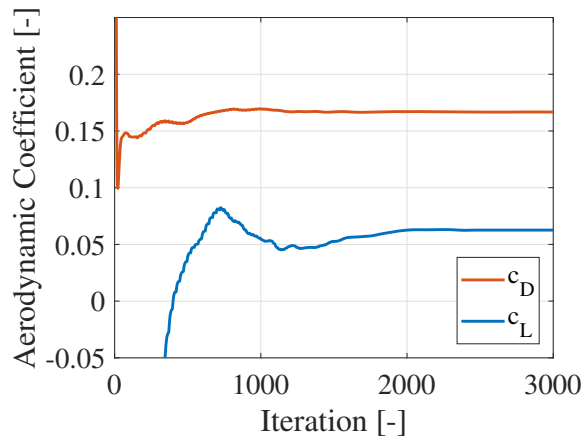


Figure 3.1: Drag and lift coefficients as a function of the number of iterations. Each 25 iterations represent a time step of 0.05 s. Simulation performed using full domain, URANS equations with a time step of 0.05 s and  $\gamma Re_\theta$  model.

As can be seen in figure 3.1, both aerodynamic coefficients end up converging to a steady value. The final coefficient values match perfectly with the ones obtained through the use of a RANS simulation in a half domain.

The steadiness of the studied case was also verified at the wind tunnel. The high sampling ratio of the force sensor allows to obtain a good temporal resolution of the signal, allowing to fully characterize the time component of the problem. A fast Fourier

<sup>1</sup>Unsteady Reynolds Averaged Navier-Stokes

<sup>2</sup>In this simulation the symmetry of the problem is not exploited.

transform is performed with the  $x$  axis force signal in order to capture the frequencies that are hidden within the measurements. In figures 3.2 and 3.3, the single-sided amplitude spectrum of this signal at different  $Re_L$  is shown, as well as a wind-off test<sup>3</sup> carried out in order to obtain the natural frequencies of the structure itself.

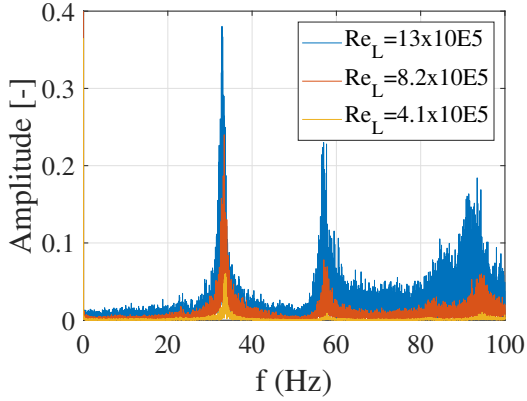


Figure 3.2: Single sided amplitude spectrum of the experimental  $F_x(t)$  at multiple  $Re_L$ . Measurements performed at 200 Hz.

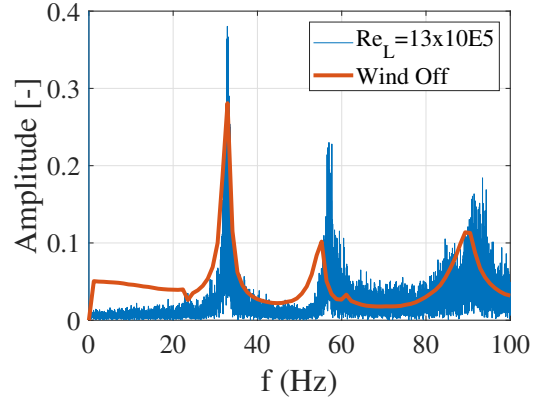


Figure 3.3: Comparison of the single sided amplitude spectrum of the experimental  $F_x(t)$  at  $Re_L = 13 \times 10^5$  and wind-off results. Measurements performed at 200 Hz for the wind test and 1000 Hz for the wind-off test. Wind off amplitude multiplied by 15 for better comparison.

Figure 3.2 shows how the amplitude of the peaks decrease with decreasing  $Re_L$ , however its frequency does not change. When these results are compared to the ones obtained at the wind-off test (figure 3.3), it is possible to observe how the obtained frequencies correspond to the mode frequencies of the structure. The slight shift observed in the middle and right peaks can be caused by small non-linearities present in the structure. This leads to the conclusion that these peaks represent the modes of the set-up structure and not flow unsteadiness, confirming that the flow around the car is steady.

It is possible to conclude that the flow around the Electra is steady, being therefore possible to use RANS equations without losing information, and the use of symmetry does not represent a source of error, being possible to perform half domain simulation. This two assumptions: steadiness and symmetry, allow to dramatically decrease the calculation time.

<sup>3</sup>Test at which the structure is knocked in order to extract its natural frequencies.

## 3.2 Reynolds effect study

Even though an average of 25 km/h is searched by the team, it is impossible to maintain a constant velocity. Corners, traffic and a mandatory stop at the finish line each time the car completes a lap, makes the ideal 25 km/h mark an utopia. What is the effect of that change in the Reynolds number on the aerodynamic properties of the car? The Reynolds effect study will allow to understand this effect, as well as permit to validate the CFD simulations for multiple test cases. The results will be studied via force measurements as well as with pressure distribution plots.

### 3.2.1 Force coefficient comparison

In this section, the force coefficients obtained with the different turbulent and transition models will be compared to experimental results. The total forces acting on a body are one of the best ways to validate a numerical simulation, as the large amount of contributions involved in these values makes them an ideal parameter to validate a numerical simulation.

In this section, the force results will be non-dimensionalized in order to be able to directly compare simulations, which takes into account the real size of the car, and wind tunnel results, which uses the scaled model. The non-dimensional force coefficients are defined as

$$c_F = \frac{2F}{\rho v^2 A_{ref}}. \quad (3.2.1)$$

Remember that the real car  $A_{ref}$  is of  $0.957 \text{ m}^2$ , but for the wind tunnel tests, this value must be multiplied by the scaling of the model squared, yielding a value of  $0.0455 \text{ m}^2$  for the wind tunnel  $A_{ref}$ .

### Wall function models

The first simulations to be studied are the wall function version of the  $k - \varepsilon$  and  $k - \omega$  models. The obtained results, as well as a direct comparison with the obtained experimental drag coefficient can be seen in figure 3.4. In figure 3.5, the numerical results for the lift coefficient are shown.

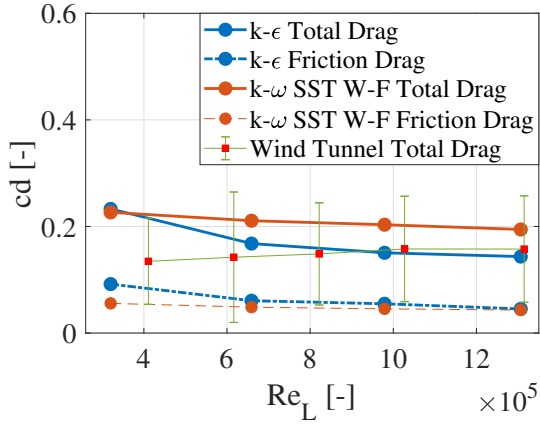


Figure 3.4: Drag coefficient at different length based Reynolds numbers obtained experimentally and with the wall function version of the  $k - \epsilon$  and  $k - \omega$  SST models.

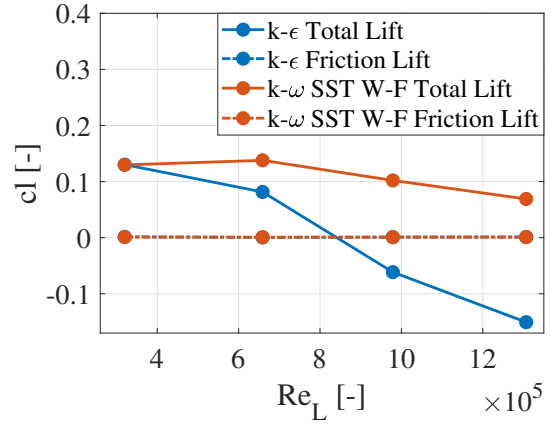


Figure 3.5: Lift coefficient at different length based Reynolds numbers obtained with the wall function version of the  $k - \epsilon$  and  $k - \omega$  SST models.

As can be observed in figure 3.4, both turbulence models failed to capture the trend shown by the experimental tests. While the experimental results show a gentle increase in the drag coefficient with increasing Reynolds number, both numerical simulations predicted a decrease of the drag coefficient. Both simulations present results inside the error bars<sup>4</sup> of the experimental measurements except for the lowest Reynolds simulations. At higher Reynolds numbers, the agreement between experimental and numerical results must be highlighted. Overall, the  $k - \epsilon$  model gives closer values to the experiments, but this does not mean the  $k - \epsilon$  model is the best out of the two. A more exhaustive study of the studied conditions and assumptions must be done in order to fully understand these values.

The first thing to keep in mind is the modelling of the boundary layer created at the floor. A comparison between the boundary layer present at the wind tunnel and at the numerical simulations is shown in figure 3.6.

<sup>4</sup>The error bars were computed as the standard deviation of the drag coefficient.



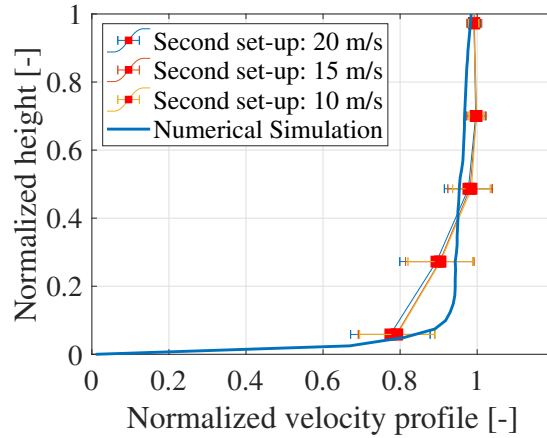


Figure 3.6: Comparison of wind tunnel and numerical boundary layer at 0.5 car lengths in front of the car. Velocity normalized by dividing by the free-stream velocity and the height normalized in such a way that 1 represents the car height.

As can be observed in figure 3.6, both boundary layers present a quite different profile. The numerical boundary layer is fuller than the one present at the wind tunnel. This means that while the upper part of the car sees the same equivalent flow velocity<sup>5</sup>, it is not the case on the lower one, in which the wind tunnel model sees a considerably lower equivalent velocity. In terms of force, this would mean that lower drag force must be measured at the wind tunnel when compared to the numerical simulations.

Another effect that must be taken into account is the laminar to turbulent transition. While the wind tunnel model surface is perfectly smooth (therefore the transition from a laminar to a turbulent boundary layer will be triggered faster than in the case of an ideally smooth surface), a laminar boundary layer at the frontal part of the car will be present. This laminar boundary layer, which is not modelled by the turbulent models, will also reduce the total drag measured at the wind tunnel tests.

After taking a look at these two considerations, it is expected to obtain higher drag values with the numerical simulations. The smoother trend presented by the  $k - \omega$  simulations coupled with the fact that a higher drag coefficient is obtained could lead to the conclusion that the  $k - \omega$  model is the most accurate model of the two.

This conclusion is further reinforced when the lift coefficient is analysed. While the  $k - \omega$  simulation shows a slowly varying lift coefficient, the lift coefficient obtained with the  $k - \varepsilon$  model presents a large variation becoming even negative at the highest Reynolds numbers. How is this possible?

<sup>5</sup>Flow velocity that allows to reach a desired Reynolds number.

As already mentioned in chapter 2, the wall function models can have serious problems detecting and modelling boundary layer separation. This is the case with the  $k - \varepsilon$  model as can be observed in figures 3.7 and 3.8 where a comparison of the velocity field at the symmetry plane of the car is made.

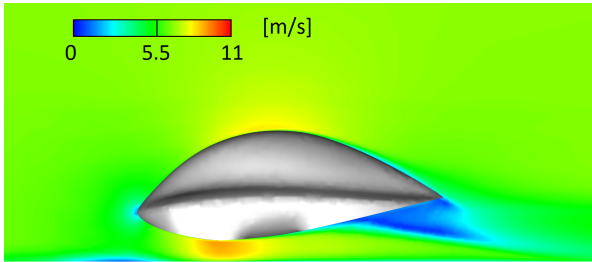


Figure 3.7: Velocity field contour plot at the symmetry plane of the car. Simulation performed with the wall function version of the  $k - \omega$  SST model, still road conditions and a  $Re_L = 13 \times 10^5$ .

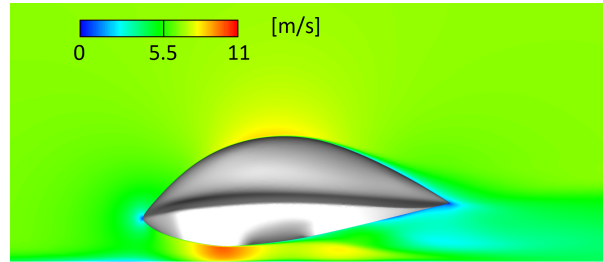


Figure 3.8: Velocity field contour plot at the symmetry plane of the car. Simulation performed with the wall function version of the realizable  $k - \varepsilon$  model, still road conditions and a  $Re_L = 13 \times 10^5$ .

Figures 3.7 and 3.8 show how both models present a completely different solution. While a big separation of the boundary layer on the lower part of the car can be seen on the  $k - \omega$  simulation, this is not the case on the  $k - \varepsilon$  model. This absence of rear separation also augments the quantity of air passing through Electra's lower surface, causing the flow to be more accelerated than in the  $k - \omega$  simulation on the narrower section between the car and the floor.

Finally it is possible to conclude that while both models present low Reynolds dependency on the drag coefficient values and the coefficient values stay inside the error bars of the experimental measurements, the analysis of the studied conditions and the lift coefficient analysis lead to the deduction that the wall function version of the  $k - \omega$  SST turbulent model present a more robust and accurate solution.

### Low Reynolds models

After studying the wall function models, the results obtained with the low Reynolds version of the  $k - \omega$  SST and the transition model  $\gamma Re_\theta$  will be analysed and compared to the experimental results.

Before examining the obtained results, it is important to bear in mind the main difference between these two models. While both are based on the same turbulence

model (the  $k - \omega$  SST), the  $\gamma Re_\theta$  model is capable of modelling the transition from laminar to turbulent boundary layer. Keeping in mind that the skin friction force that inserts a laminar boundary layer is lower than the one inserted by a turbulent boundary layer, therefore lower drag coefficient values are expected from the transition model. As stated before, the surface roughness of the wind tunnel model would trigger the transition from laminar to turbulent boundary layer faster than in the  $\gamma Re_\theta$  simulation (where the surface roughness is not modelled). This should yield slightly higher  $c_D$  values at the wind tunnel than in the transition model simulations, but lower values than in the  $k - \omega$  SST simulations. However, it will be necessary to take into account the effect of the boundary layer, which would lower the  $c_D$  coefficient of the wind tunnel simulations.

Figures 3.9 and 3.10 show the obtained results for both models and the experimental tests.

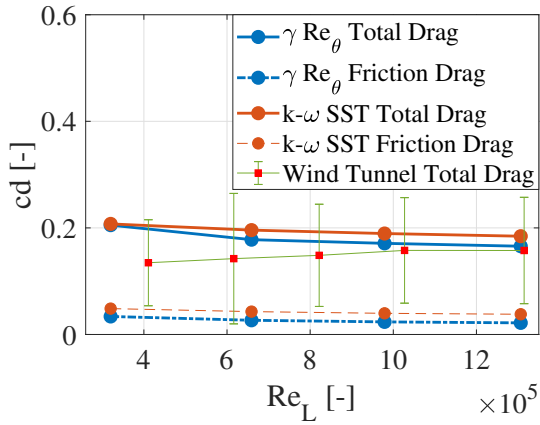


Figure 3.9: Drag coefficient at different length based Reynolds numbers obtained experimentally and with the low-Reynolds version of the  $k - \omega$  SST model and the  $\gamma Re_\theta$  transition model, still road conditions and a  $Re_L = 13 \times 10^5$ .

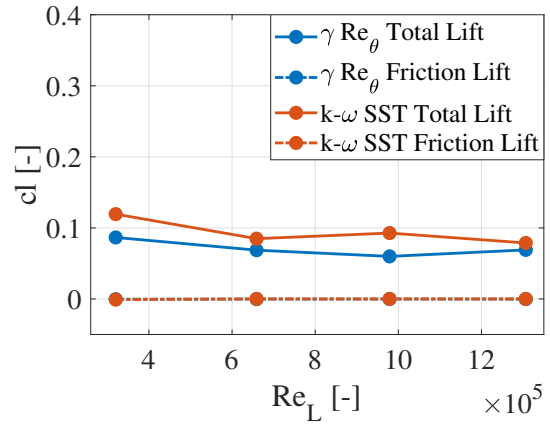


Figure 3.10: Lift coefficient at different length based Reynolds numbers obtained with the low-Reynolds version of the  $k - \omega$  SST model and the  $\gamma Re_\theta$  transition model, still road conditions and a  $Re_L = 13 \times 10^5$ .

Albeit not being as accentuated as for the case of the realizable  $k - \varepsilon$  model with non-equilibrium wall functions, the numerical simulations presents a gentle decreasing trend in opposition to the experimental drag coefficient which increases as the Reynolds number increases. It is worth mentioning the high level of agreement between numerical and experimental  $c_D$  at the  $Re_{L_{ref}}$ .

As already discussed, the transition model presents lower  $c_D$  values than the turbulent model. As can be observed, most of this difference is due to the pressure/friction drag ratio.

Analysing the lift coefficient values presented in figure 3.10, positive lift is predicted by both models, and no abrupt changes in the are observed. A comparison of the velocity field obtained with both models can be seen in figures 3.11 and 3.12.

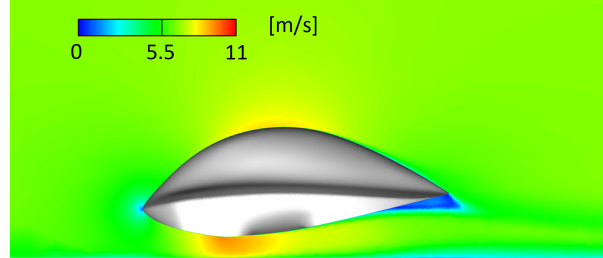
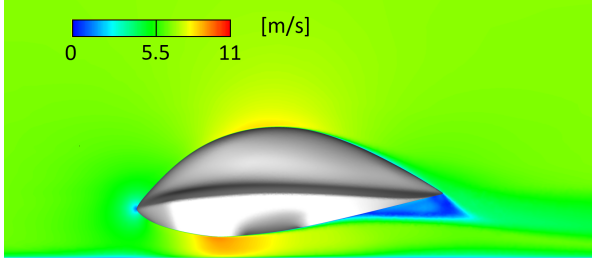


Figure 3.11: Velocity field contour plot at the symmetry plane of the car. Simulation performed with the low Reynolds version of the  $k - \omega$  SST model, still road conditions and a  $Re_L = 13 \times 10^5$ .

Figure 3.12: Velocity field contour plot at the symmetry plane of the car. Simulation performed with the  $\gamma Re_\theta$  transition model, still road conditions and a  $Re_L = 13 \times 10^5$ .

It is possible to observe how both models predicts a similar velocity field, being noticeable the separation of the boundary layer at Electra's tail. This time, this separation of the flow does not represent a problem to the numerical models, proving the higher reliability of the low Reynolds models.

As a conclusion, it was possible to observe low Reynolds dependency from the simulations and the wind tunnel tests. Both methods yielded similar results, obtaining higher discrepancies at lower Reynolds numbers than at higher ones, where the agreement between numerical and experimental results was remarkable.

### Low Reynolds vs wall function models

Once low Reynolds and wall function models were compared with their alike, it is then interesting to compare the differences between a low Reynolds and a wall function version of the same model. Figures 3.13 and 3.14 present a comparison between the two versions of the  $k - \omega$  SST model.

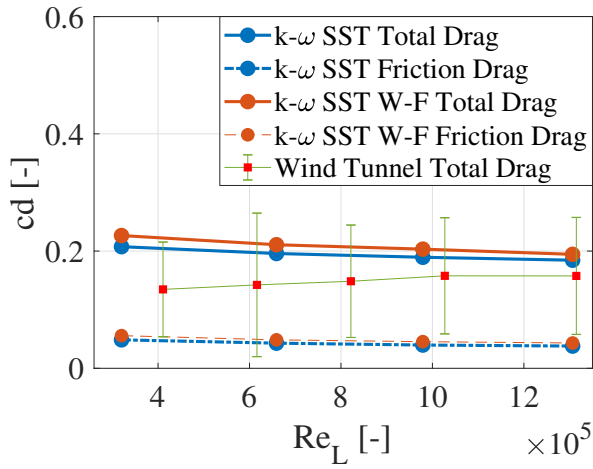


Figure 3.13: Drag coefficient at different length based Reynolds numbers obtained experimentally and with the wall function and low-Reynolds version of the  $k - \omega$  SST model, still road conditions and a  $Re_L = 13 \times 10^5$ .

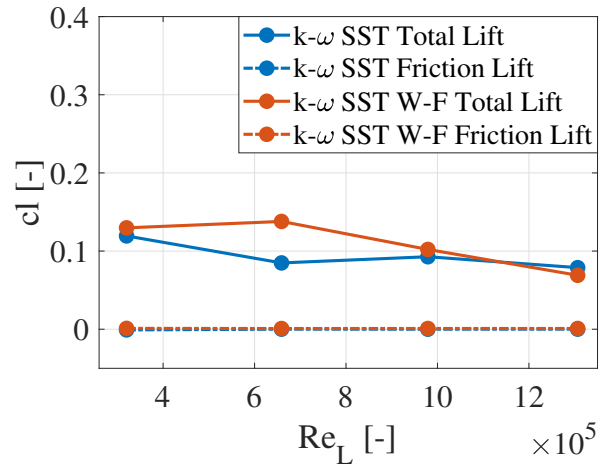


Figure 3.14: Lift coefficient at different length based Reynolds numbers obtained with the wall function and low-Reynolds version of the  $k - \omega$  SST model, still road conditions and a  $Re_L = 13 \times 10^5$ .

It is possible to observe how both versions present very similar drag coefficient results, being the coefficients of the low Reynolds version slightly lower than the ones from its counterpart version. The same can be concluded from figure 3.14, where similar results are obtained for both models, with the exception of the case  $Re = 6.5 \times 10^5$ , where a higher discrepancy can be observed.

In order to understand the cause of this discrepancy, the velocity field at a Reynolds number  $Re = 6.5 \times 10^5$  for both versions is shown in figures 3.15 and 3.16.

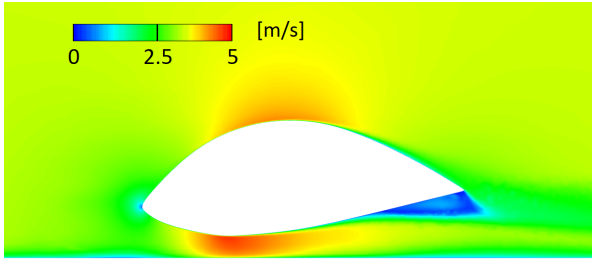


Figure 3.15: Velocity field contour plot at the symmetry plane of the car. Simulation performed with the low Reynolds version of the  $k - \omega$  SST model, still road conditions and a  $Re_L = 6.5 \times 10^5$ .

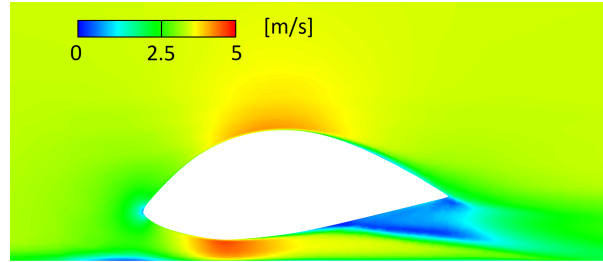


Figure 3.16: Velocity field contour plot at the symmetry plane of the car. Simulation performed with the wall function version of the  $k - \omega$  SST model, still road conditions and a  $Re_L = 6.5 \times 10^5$ .

Figure 3.16 shows how the wall function version of the  $k - \omega$  model can also present some deficiencies when separation of the boundary layer is involved, causing the difference in lift coefficient.

After this study, it is possible to conclude that  $c_D$  values around 0.16 are obtained for the Electra in still road conditions. How does this value compare to other low drag configurations appearing in literature? Figure 3.17 shows some well known basic shapes and their respective drag coefficient.

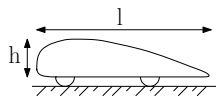
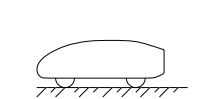
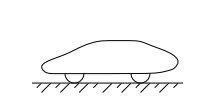
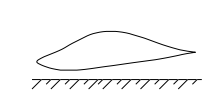
Basic body	$c_D$	l/h	Configuration
	0.15	4.0	With wheels modelled
	0.16	3.0 3.9	With wheels modelled
	0.07 0.18	3.1	Without wheels With wheels
	0.05		Without wheels

Figure 3.17:  $c_D$  of different basic bodies. (Adapted from [4]). References in which each basic shape appears (from top to bottom): [5], [6], [7] and [8].

As can be observed in figure 3.17, a  $c_D$  value around 0.16 compares well to other basic shapes, further corroborating the credibility of the obtained drag values. Nevertheless, the low friction/pressure drag ratio (14.5%), leads to the thinking that this shape has a margin to be optimized by reducing the pressure drag contribution.

### 3.2.2 Pressure coefficient comparison

The force validation allowed to blindly verify that the forces seen by the car in the numerical simulation are representative of the real life problem. The pressure tests will further allow to tangibly quantify the agreement between the wind tunnel experiments and the CFD simulations.

Due to the different scaling and wind speed, in order to be able to directly compare experimental and CFD results, the pressure will be studied through its non-dimensional coefficient, which is defined as

$$c_P = \frac{p - p_{\text{inf}}}{\frac{1}{2}\rho_{\text{inf}}V_{\text{inf}}^2}. \quad (3.2.2)$$

As already stated in section 2, this comparison will be performed on two planes: the symmetry plane of the car, and the cross section plane that contains the highest point of the car.

#### Wall function models

The first models to be studied are the wall-function versions of the  $k - \omega$  SST and the realizable  $k - \varepsilon$ . First a direct comparison between both models will be made, and a comparison to experiments will be performed later. Figures 3.18, 3.19, 3.20 and 3.21 show the pressure coefficient distribution obtained with both methods at different Reynolds numbers.

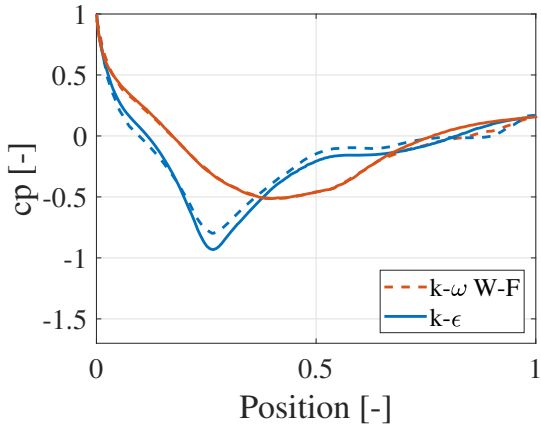


Figure 3.18:  $c_P$  plot at the symmetry plane of the car using wall function models. W-F stands for wall function. Upper surface of the car in orange, lower surface in blue. Simulation performed with still road conditions and a  $Re_L = 3.5 \times 10^5$ . Position normalized such that 1 equals the car length.

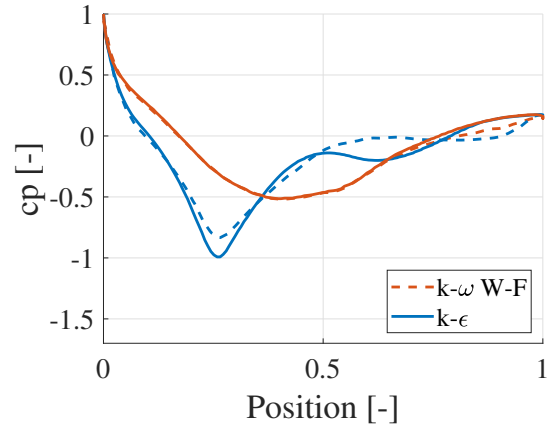


Figure 3.19:  $c_P$  plot at the symmetry plane of the car using wall function models. W-F stands for wall function. Upper surface of the car in orange, lower surface in blue. Simulation performed with still road conditions and a  $Re_L = 6.6 \times 10^5$ . Position normalized such that 1 equals the car length.

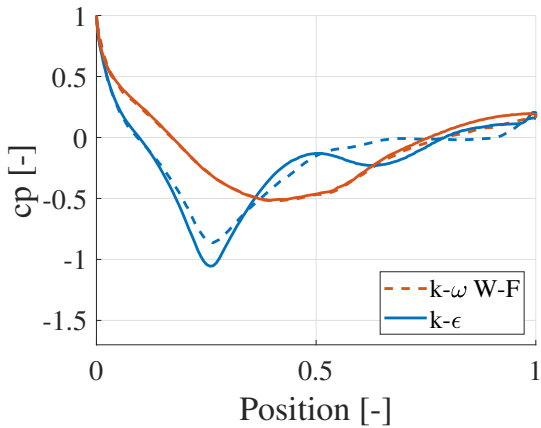


Figure 3.20:  $c_P$  plot at the symmetry plane of the car using wall function models. W-F stands for wall function model. Upper surface of the car in orange, lower surface in blue. Simulation performed with still road conditions and a  $Re_L = 9.8 \times 10^5$ . Position normalized such that 1 equals the car length.

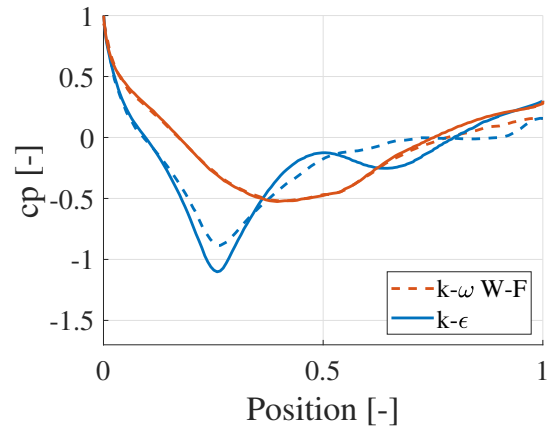


Figure 3.21:  $c_P$  plot at the symmetry plane of the car using wall function models. W-F stands for wall function model. Upper surface of the car in orange, lower surface in blue. Simulation performed with still road conditions and a  $Re_L = 13 \times 10^5$ . Position normalized such that 1 equals the car length.



Both models yields nearly identical results for the upper surface of the car, however, big differences are observed on the lower surface. The first difference yields in the value at the suction peak present around position 0.25. The value obtained at this peak by the  $k - \varepsilon$  model is substantially lower than the one shown by the  $k - \omega$  model. As already pointed out, the difference in the lower passing flow characteristics, changes the speed that passes underneath the car, changing its pressure value. In this case, the lower pressure seen at the  $k - \varepsilon$  model denotes a higher velocity than the computed by the  $k - \omega$ . Once this suction peak is surpassed, it is possible to observe how both models agree at low Reynolds numbers, but start to diverge as the Reynolds increases. At high Reynolds, the  $k - \varepsilon$  increases the  $c_P$  more abruptly than the  $k - \omega$ , reaching higher  $c_P$ . This steeper increase in pressure (or higher pressure gradient), causes the flow to separate sooner on the  $k - \varepsilon$  simulation than in the  $k - \omega$  one, obtaining that a sudden depression on the  $c_P$ .

As can be observed, the lower flow characteristics obtained through the  $k - \varepsilon$  simulation, highly depends on the Reynolds number. This is the main cause for Reynolds dependency that showed the lift coefficient obtained with this model (figure 3.5).

Once these models have been compared to each other, it is now time to compare them directly to experimental results. Figures 3.22 and 3.23 shows a comparison between experimental and CFD results.

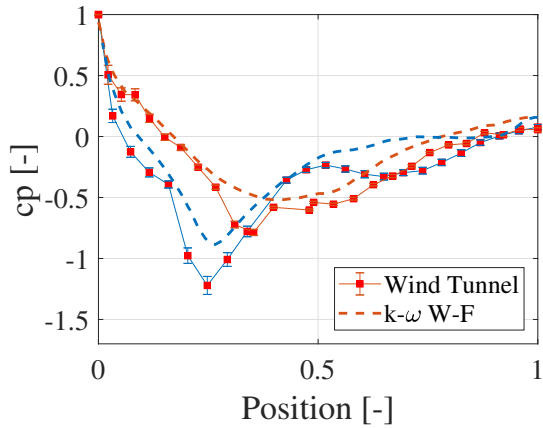


Figure 3.22:  $c_P$  plot at the symmetry plane of the car comparing experimental and CFD results. W-F stands for wall function model. Upper surface of the car in orange, lower surface in blue. Simulation performed with still road conditions and a  $Re_L = 13 \times 10^5$ . Position normalized such that 1 equals the car length.

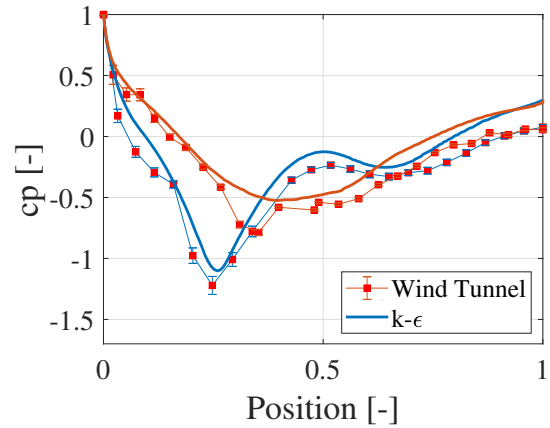


Figure 3.23:  $c_P$  plot at the symmetry plane of the car comparing experimental and CFD results. Upper surface of the car in orange, lower surface in blue. Simulation performed with still road conditions and a  $Re_L = 13 \times 10^5$ . Position normalized such that 1 equals the car length.

Analyzing figures 3.22 and 3.23, it is possible to observe how the upper surface pressure distribution is in general well captured by both methods. However it is worth mentioning the sudden decrease in the experimental  $c_P$  that is present around the normalized position 0.35. This sudden decrease in pressure could be due to a measurement error induced by a surface irregularity.

On the lower surface it is possible to see how the  $k - \varepsilon$  model surprisingly follows the experimental pressure distribution much better than the  $k - \omega$  model. The  $k - \omega$  model is not able to capture the low pressure found at the suction lower suction peak, or the pressure depression seen at the experimental tests.

In general, it was possible to observe how both models are capable of predicting the general flow properties of the car. One could conclude that the realizable  $k - \varepsilon$  model was capable of representing the flow more accurately than the  $k - \omega$ , however this should be further analysed. In figures 3.18, 3.19, 3.20 and 3.21, it was possible to observe how the depression found on the second half of the lower surface is highly modified at different Reynolds numbers, however, it will be shown later (section 3.2.2) that this depression does not vary significantly in the wind tunnel tests when the Reynolds is changed. This leads to the conclusion that the separation seen in the wind tunnel results are caused by surface irregularities (since the separation is triggered even at low speeds). These surface irregularities are not modelled on the CFD model, and therefore its effect should not be observed.

### Low Reynolds models

Now, this section will compare the low Reynolds version of the  $k - \omega$  SST and the  $\gamma Re_\theta$  model. As for the wall function models, a comparison to experimental results will also be made.

One of the main differences that will be observed in this comparison is the laminar to turbulent transition. This transition is easily observed through a pressure coefficient plot  $c_P$  as it shows a characteristic behaviour (figure 3.24) due to the flow characteristics (figure 3.25).

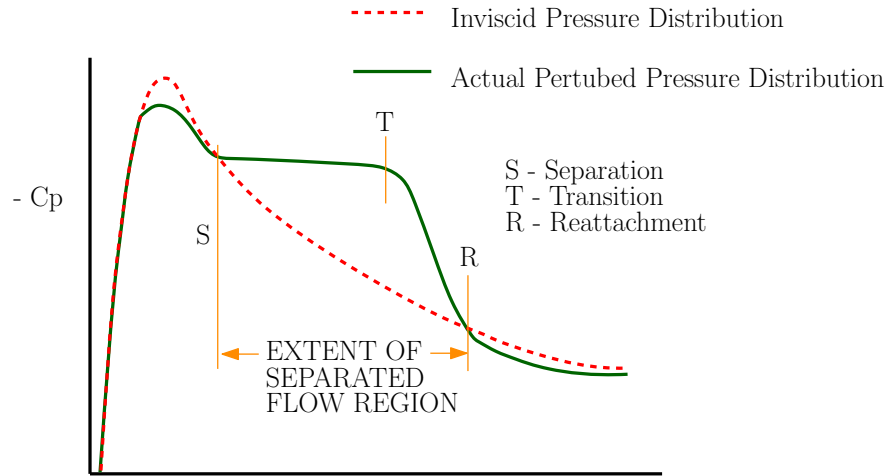


Figure 3.24: Schematic  $c_p$  behaviour when transition from laminar to turbulent occurs. (Adapted from [9])

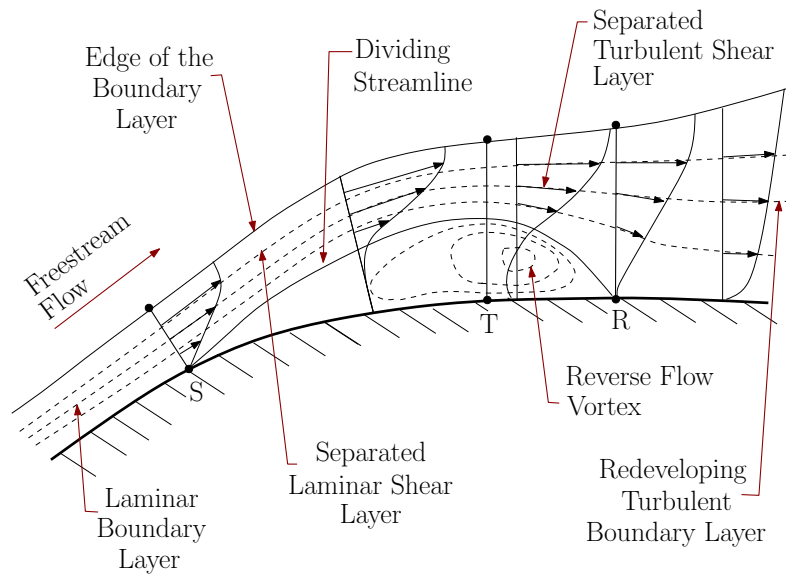


Figure 3.25: Flow in the vicinity of a transitional separation bubble. (Adapted from [10])

As can be seen in figures 3.24 and 3.25, when the transition from laminar to turbulent occurs due to the presence of a separation bubble, three different zones can be detected. When the flow commences to detach, the pressure coefficient stays almost constant, obtaining a plateau-like region. The length of this region gives an idea of the separation bubble size. Then a sudden increase in the  $c_p$  until it stabilizes again, following closely the inviscid pressure distribution. This effect can be clearly seen in figures 3.26, 3.27, 3.28 and 3.29.

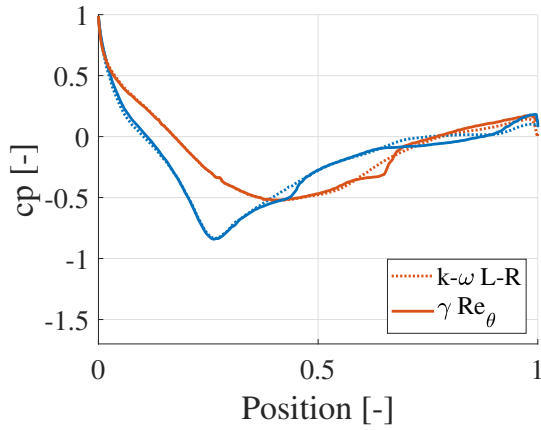


Figure 3.26:  $c_P$  plot at the symmetry plane of the car. L-R stands for low Reynolds. Upper surface of the car in orange, lower surface in blue. Simulation performed with still road conditions and a  $Re_L = 3.5 \times 10^5$ . Position normalized, 1 equals the car length.

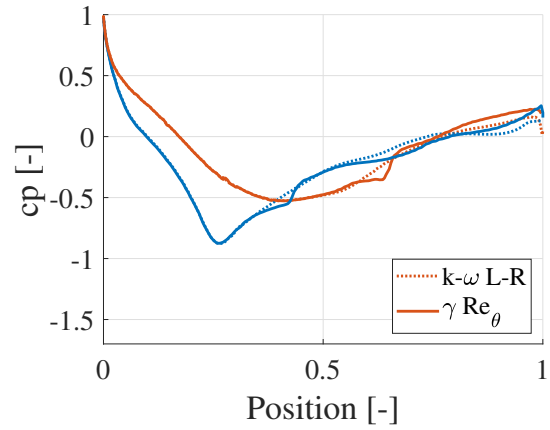


Figure 3.27:  $c_P$  plot at the symmetry plane of the car. L-R stands for low Reynolds. Upper surface of the car in orange, lower surface in blue. Simulation performed with still road conditions and a  $Re_L = 6.6 \times 10^5$ . Position normalized, 1 equals the car length.

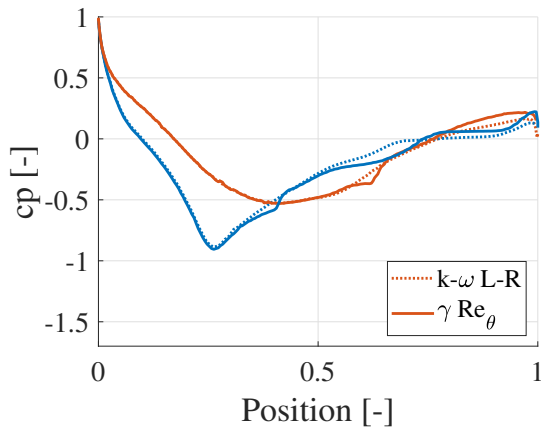


Figure 3.28:  $c_P$  plot at the symmetry plane of the car using low Reynolds models. L-R stands for low Reynolds model. Upper surface of the car in orange, lower surface in blue. Simulation performed with still road conditions and a  $Re_L = 9.8 \times 10^5$ . Position normalized such that 1 equals the car length.

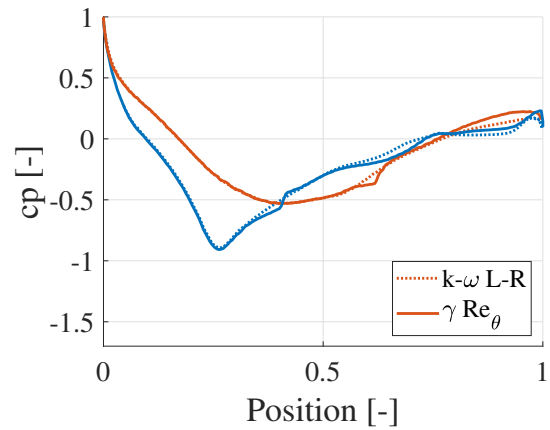


Figure 3.29:  $c_P$  plot at the symmetry plane of the car using low Reynolds models. L-R stands for low Reynolds model. Upper surface of the car in orange, lower surface in blue. Simulation performed with still road conditions and a  $Re_L = 13 \times 10^5$ . Position normalized such that 1 equals the car length.

As shown in the previous figures, both models present a good agreement in the pressure values, being the transition present in the  $\gamma Re_\theta$  simulations the main difference between both models. The pressure coefficient plots yields similar results for all the simulated Re. This is true also for the transition from laminar to turbulent shown by the  $\gamma Re_\theta$  simulations. Transition occurs before on the lower surface of the car, mainly due to the higher complexity of the car shape in this region. The transition from laminar to turbulent can be observed through an intermittency plot as shown in figures 3.30 and 3.31.

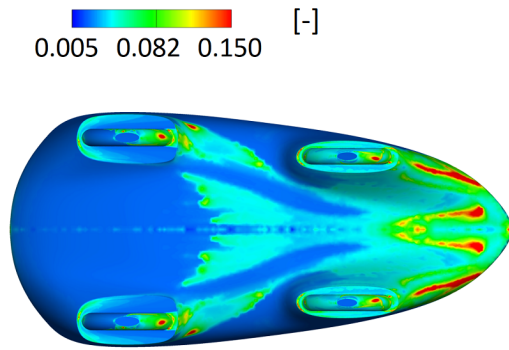


Figure 3.30: Intermittency contour plot over the Electra. Simulation performed with the  $\gamma Re_\theta$  model, still road conditions and a  $Re_L = 13 \times 10^5$ .

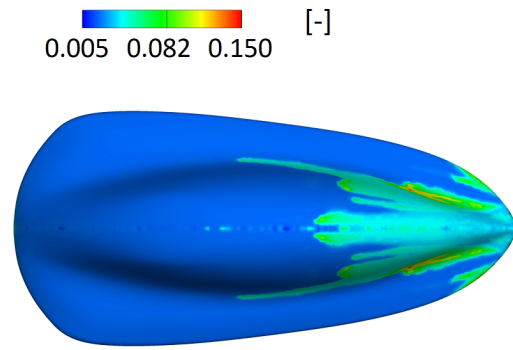


Figure 3.31: Intermittency contour plot over the Electra. Simulation performed with the  $\gamma Re_\theta$  model, still road conditions and a  $Re_L = 13 \times 10^5$ .

As already observed in the pressure coefficient graphs, due to the higher complexity of the lower surface of the Electra, which induces large 3D effects, the presence of turbulence on the lower region is higher and stronger.

Although a perfect agreement between both models can be seen on the first quart of figures 3.26, 3.27, 3.28 and 3.29, a slight disagreement between both models can be seen on the lower surface after the 0.5 mark.

After comparing both low Reynolds models, a direct comparison to the experimental results at different Reynolds numbers is shown in figures 3.32, 3.33, 3.34 and 3.35.

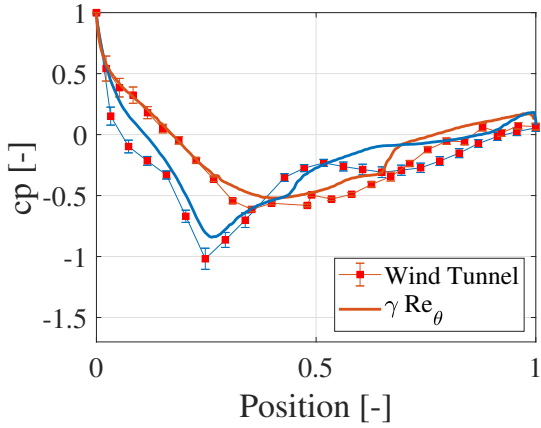


Figure 3.32:  $c_P$  plot at the symmetry plane of the car comparing experimental and low Reynolds results. Upper surface of the car in orange, lower surface in blue. Simulation performed with still road conditions and a  $Re_L = 3.5 \times 10^5$ . Position normalized, 1 equals the car length.

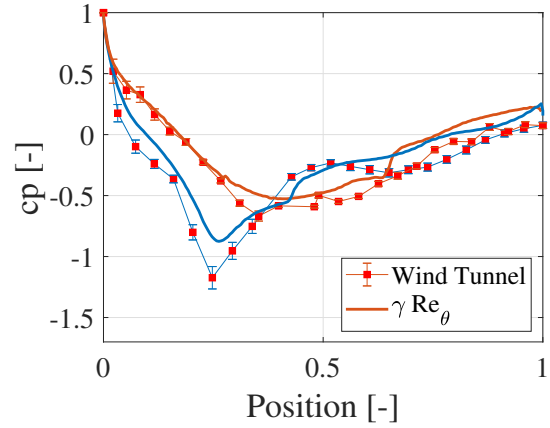


Figure 3.33:  $c_P$  plot at the symmetry plane of the car comparing experimental and low Reynolds results. Upper surface of the car in orange, lower surface in blue. Simulation performed with still road conditions and a  $Re_L = 6.6 \times 10^5$ . Position normalized, 1 equals the car length.

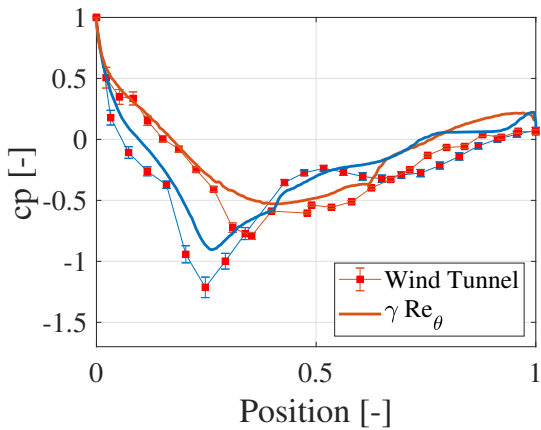


Figure 3.34:  $c_P$  plot at the symmetry plane of the car comparing experimental and CFD results. Upper surface of the car in orange, lower surface in blue. Simulation performed with still road conditions and a  $Re_L = 9.8 \times 10^5$ . Position normalized such that 1 equals the car length.

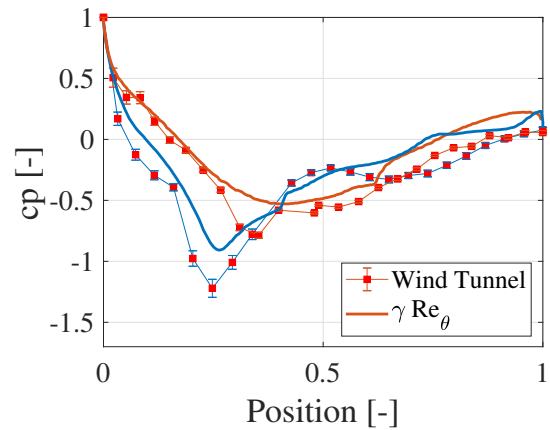


Figure 3.35:  $c_P$  plot at the symmetry plane of the car comparing experimental and CFD results. Upper surface of the car in orange, lower surface in blue. Simulation performed with still road conditions and a  $Re_L = 13 \times 10^5$ . Position normalized such that 1 equals the car length.

This comparison shown in figures 3.32, 3.33, 3.34 and 3.35 show how the transition from laminar to turbulent is not captured in the wind tunnel. This can be due to the high level of turbulence shown by the lower region of the experimental boundary layer, which mixed with the surface roughness of the Electra model compromises this transition.

The overall shape of the pressure coefficient distribution is well captured by the transition model, however some discrepancies are shown as could be expected. The largest discrepancies are shown at the second half of the Electra lower surface. Again, the high complexity of the flow in this region leads to some disagreement in the pressure coefficient values, yielding a lower value on the experimental results.

As could be seen, CFD simulations are capable of representing the middle plane pressure distribution, now the cross section plane pressure coefficient distribution of the  $\gamma Re_\theta$  solution will be compared to experimental results. The obtained plots are shown in figures 3.36, 3.37, 3.38 and 3.39.

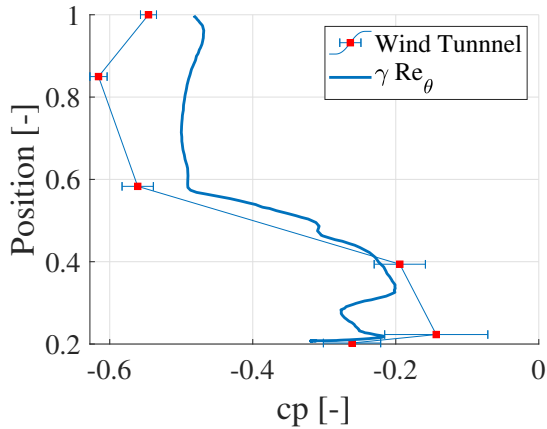


Figure 3.36:  $c_P$  plot at the cross section plane of the car passing through its highest point comparing experimental and CFD results. Simulation performed with still road conditions and a  $Re_L = 3.5 \times 10^5$ . Position normalized such that 1 equals the car height.

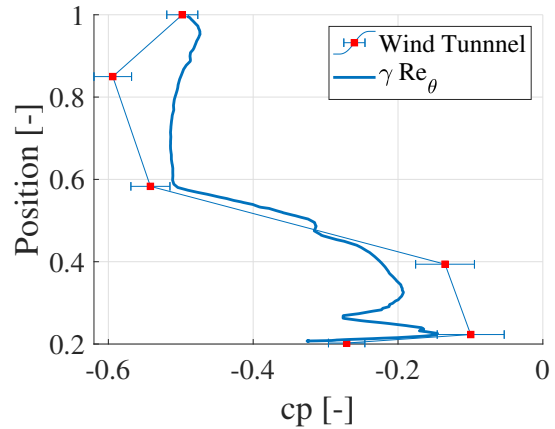


Figure 3.37:  $c_P$  plot at the cross section plane of the car passing through its highest point comparing experimental and CFD results. Simulation performed with still road conditions and a  $Re_L = 6.6 \times 10^5$ . Position normalized such that 1 equals the car height.

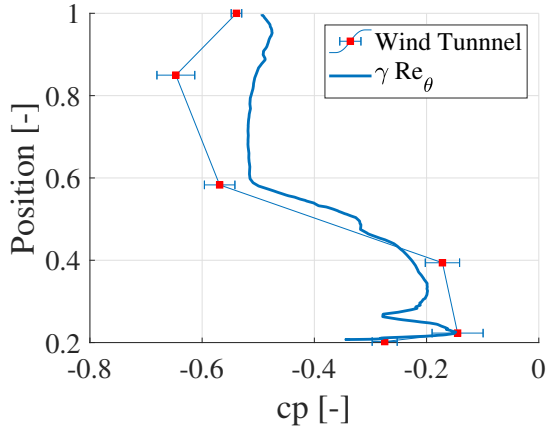


Figure 3.38:  $c_P$  plot at the cross section plane of the car passing through its highest point comparing experimental and CFD results. Simulation performed with still road conditions and a  $Re_L = 9.8 \times 10^5$ . Position normalized such that 1 equals the car height.

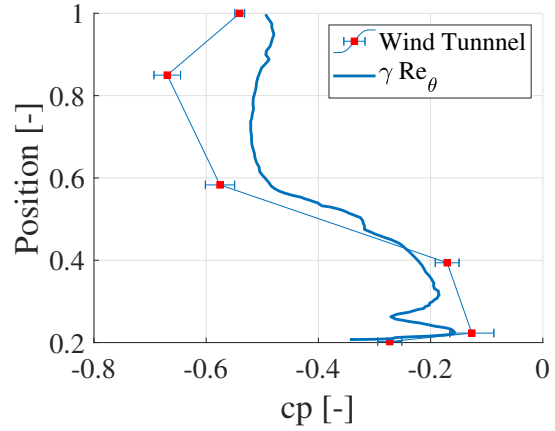


Figure 3.39:  $c_P$  plot at the cross section plane of the car passing through its highest point comparing experimental and CFD results. Simulation performed with still road conditions and a  $Re_L = 13 \times 10^5$ . Position normalized such that 1 equals the car height.

As for the symmetry plane plots, the  $\gamma Re_\theta$  is capable of capturing the pressure coefficient distribution shape over the entire height. The largest discrepancies are seen at the normalized heights ranging between 1 and 0.6, where the wind tunnel results show a much lower pressure coefficient than the one shown by the CFD simulation.

One could conclude that even though some discrepancies between the experimental and the numerical results are found, the general properties of the pressure distribution are well captured. It is also necessary to keep in mind the multiple factors playing a role in the experimental results, such as the turbulence level, the boundary layer, the surface quality and even the errors that the pressure taps imperfections could induce on the final measurements.

### Low Reynolds vs wall function models

After comparing wall function models and low Reynolds models to experimental results, it would be interesting to directly compare the low Reynolds and the wall function version of the  $k - \omega$  SST model. This comparison is shown in figures 3.40, 3.41, 3.42 and 3.43.



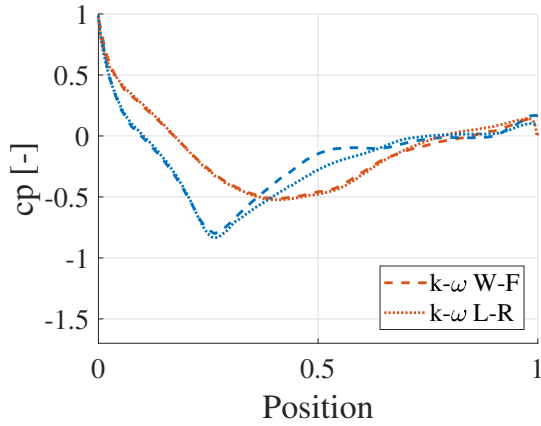


Figure 3.40:  $c_P$  plot at the symmetry plane of the car. W-F stands for wall function model and L-R stands for low Reynolds model. Upper surface of the car in orange, lower surface in blue. Still road conditions and a  $Re_L = 3.5 \times 10^5$ . Position normalized: 1 equals the car length.

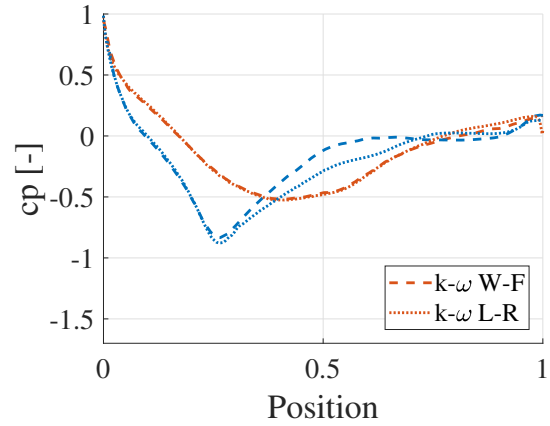


Figure 3.41:  $c_P$  plot at the symmetry plane of the car. W-F stands for wall function model and L-R stands for low Reynolds model. Upper surface of the car in orange, lower surface in blue. Still road conditions and a  $Re_L = 6.6 \times 10^5$ . Position normalized: 1 equals the car length.

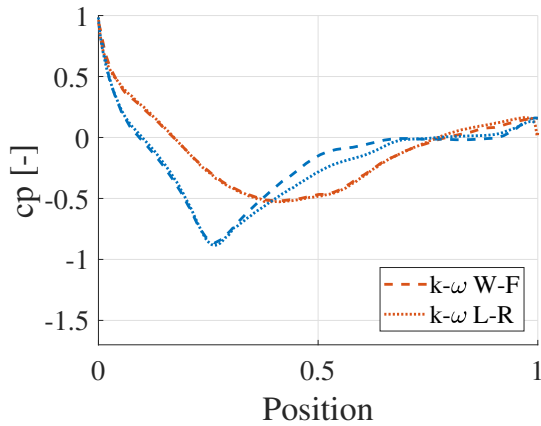


Figure 3.42:  $c_P$  at the symmetry plane comparing low Reynolds and wall function models. W-F stands for wall function and L-R stands for low Reynolds. Upper surface of the car in orange, lower surface in blue. Simulation performed with still road conditions and a  $Re_L = 9.8 \times 10^5$ . Position normalized, 1 equals the car length.

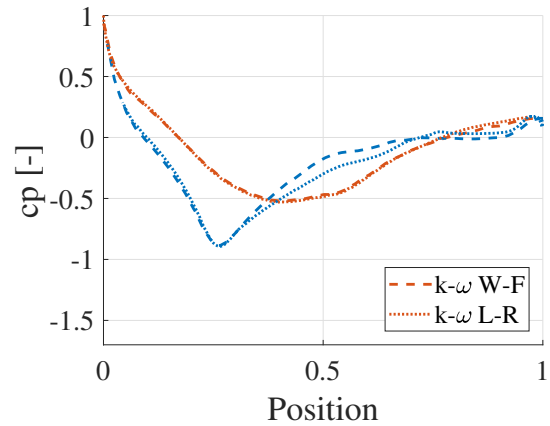


Figure 3.43:  $c_P$  at the symmetry plane comparing low Reynolds and wall function models. W-F stands for wall function and L-R stands for low Reynolds. Upper surface of the car in orange, lower surface in blue. Simulation performed with still road conditions and a  $Re_L = 13 \times 10^5$ . Position normalized such that 1 equals the car length.

It is possible to conclude that both versions of the model captures the same pressure distribution on the top surface of the car. This is not the case for its lower surface, where a higher difference is seen by both models on the central region. This higher increase on the pressure coefficient seen by the wall function version of the model creates a higher pressure gradient than in the low Reynolds version, causing the premature separation of the boundary layer already seen in the velocity contour plots of figures 3.15 and 3.16.

### 3.2.3 Boundary layer effect

As already seen in this report (figure 3.6), the boundary layer present in the wind tunnel differed from the one seen on the numerical simulations. This difference in the boundary layer induces some changes in the aerodynamic properties seen by the car. A brief study of the boundary layer effect is presented in this section.

In order to easily reproduce different boundary layers without the need to change the boundary conditions applied to the numerical simulations, the distance from the inlet to the Electra is modified. Due to the non-slip condition applied to the floor, the floor boundary layer grows as a function of the travelled distance, being therefore possible to vary the flow properties seen by the car.

The four different configurations that were studied in this section are shown in table 3.1.

Case	BL growth distance
BL1	Slip floor
BL2	0.5 L
BL3	5.5 L
BL4	8 L

Table 3.1: Nomenclature for each of the tested cases and non-slip floor distance in front of the car.

For the case BL1, a slip floor condition is applied to the floor, which directly eliminates the boundary layer from the equation. For the BL2 case, the non slip condition is applied just in the floor region that remains inside the box surrounding the car (the region where the unstructured mesh is used). This will increase the effect of the floor on the car, as the non-slip condition will apply a blockage effect on the flow passing below the car. For the BL3 and BL4 cases the non-slip condition is applied to the entire floor section and the distance from the inlet to the front of the car was modified in order to modify the boundary layer development.

The non dimensionalised boundary layer velocity profile found at a half car distance in front of the Electra is shown in figure 3.44.

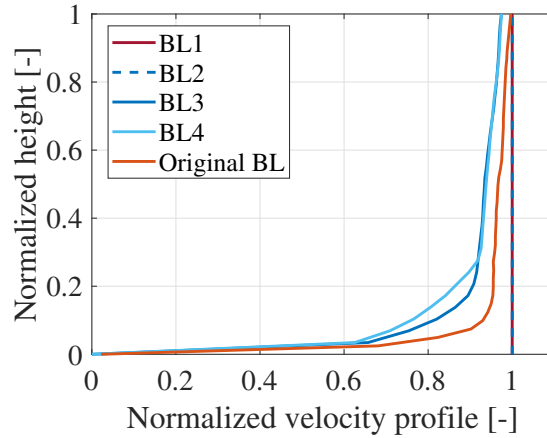


Figure 3.44: Comparison of the obtained numerical boundary layers at 0.5 car lengths in front of the car. Velocity normalized by dividing by the free-stream velocity and the height normalized in such a way that 1 represents the car height.

All simulations were performed by using the  $\gamma Re_\theta$  transition model. The force coefficients obtained for each of the cases are summarized in table 3.2.

Case	$Re_L$ [-]	$c_D$ [-]	Friction $c_D$ [-]	$c_L$ [-]	Friction $c_L$ [-]
Original	$13 \times 10E+5$	0.166	0.022	0.069	-3.6E-4
BL1	$13 \times 10E+5$	0.159	0.022	0.020	-4.5E-4
BL2	$13 \times 10E+5$	0.163	0.022	0.058	-2.8E-4
BL3	$13 \times 10E+5$	0.158	0.022	0.095	-1.6E-4
BL4	$13 \times 10E+5$	0.153	0.022	0.095	-7.5E-5
BL4	$3.5 \times 10E+5$	0.181	0.034	0.133	-2E-4

Table 3.2: Aerodynamic coefficients for each of the test cases at the specified length based Reynolds number.

As already discussed in section 3.2.1, the presence of the boundary layer decreases the force seen by the car, reducing its drag coefficient. The non-slip condition itself on the floor below the car has an important influence on the aerodynamic coefficients as can be observed in the comparison between cases BL1 and BL2. Finally, as expected, the lift coefficient increases with the presence of the boundary layer, as the higher velocity on the upper surface of Electra creates high suction while the suction on the lower surface is reduced due to the decrease in velocity. This can be seen in a pressure coefficient plot (figure 3.45).

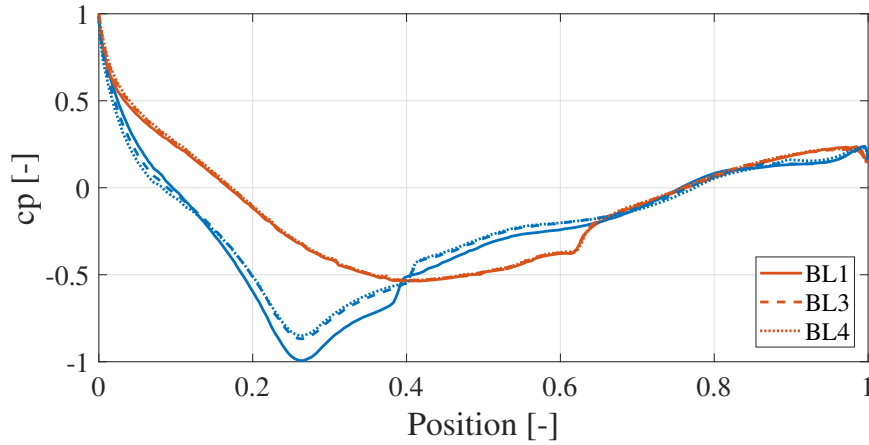


Figure 3.45:  $c_p$  plot comparing boundary layer effect. Simulations performed using the  $\gamma Re_\theta$  model at a  $Re_L = 13 \times 10^5$  with three of the different studied cases. Orange stands for upper surface and blue for lower surface.

As can be observed, the boundary layer does not have a big impact on the upper surface solution, which was expected in this study, due to the slight decrease of velocity shown by the boundary layer profile on the upper part of the car. This is not the case for the lower part, which is highly affected. The suction peak found on the lower surface around 20% the length of the car is highly affected by the lower flow velocity, and the transition from laminar to turbulent is slightly delayed. Another effect seen on the lower surface plot is the shape that shows the  $c_p$  before the suction peak. While the BL1  $c_p$  shows nearly a straight decrease in the  $c_p$ , this is not the case for the cases with more presence of the boundary layer such as cases BL3 and BL4. These cases show a more pronounced “S”-like shape, starting with a lower  $c_p$  than the BL1 case and finishing with a higher  $c_p$ . This “S” like shape was seen in the wind tunnel measurements, as could be seen in the comparisons shown in section 3.2.2.

### 3.3 Crosswind effect on Electra

In real life conditions, due to the outdoor nature of this competition, zero yaw angle conditions are rarely obtained. Curved path motion due to cornering, aerodynamic effects induced by other cars or windy conditions affect the incidence angle of the airflow, changing the forces distribution over the car and therefore affecting stability. This section will briefly study the effect of crosswind conditions on the forces and pressures seen on the car surface.

In order to simulate these conditions, the numerical and experimental car model will be rotated with respect to the flow. To estimate the angles of incidence that one could

find in real conditions, the June 2017 wind average speed present in London was taken into consideration. Obtaining the data from Meteoblue.com, a webpage that fills their databases with real data measurements and completes the missing information by simulations, an average of 15 m/s is obtained. Taking this value into consideration and a vehicle speed of 25 km/h, it is possible to compute the resultant incidence angle and relative speed seen by the car for different wind direction values, as shown in figure 3.46.

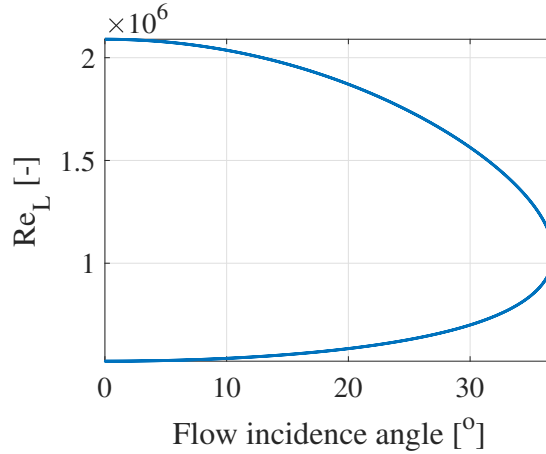


Figure 3.46: Resulting effective Reynolds seen by Electra and its respective flow incidence angle for different wind directions ranging from  $0^\circ$  to  $360^\circ$  at a speed of 15 km/h and a car rolling speed of 25 km/h.

As can be observed in figure 3.46, a maximum angle of incidence around  $36^\circ$  could be expected in competition conditions this time of the year at the selected reference speeds. Translating the obtained Reynolds numbers to wind tunnel speed, values over 50 m/s were obtained. Due to the low Reynolds dependency shown in preliminary crosswind tests, where speeds from 0 to 30 m/s were tested, a constant wind tunnel speed of 20 m/s was chosen to perform this study, a speed that yields a  $Re_L = 8.2 \times 10^5$ .

For the numerical simulations, a full domain with no symmetry condition due to the non-symmetric nature of the problem, and the  $\gamma Re_\theta$  transition model is used. The lateral walls of the domain are converted from slip walls to inlet and outlet regions, allowing the air to flow at the desired angle.

### 3.3.1 Force Tests

As a cause of the non-symmetric nature of this flow condition,  $x$  and  $y$  force values will vary as a function of the applied angle of incidence, serving as reference value for numerical validation and crosswind effect study. A comparison of numerical and experimental force results is shown in figures 3.47 and 3.48.

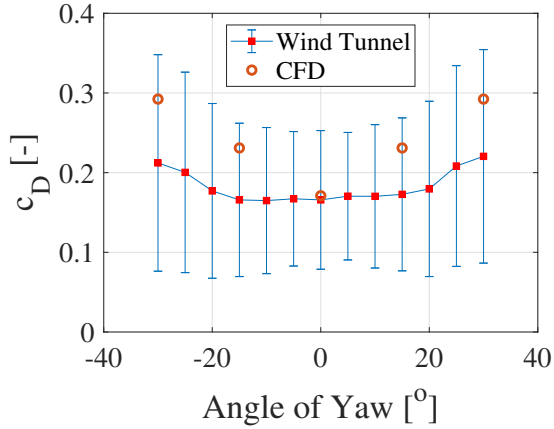


Figure 3.47: Experimental and numerical drag coefficient as a function of the wind angle of incidence for a  $Re_L = 8.2 \times 10^5$ . Simulations performed with the  $\gamma Re_\theta$  model at still conditions.

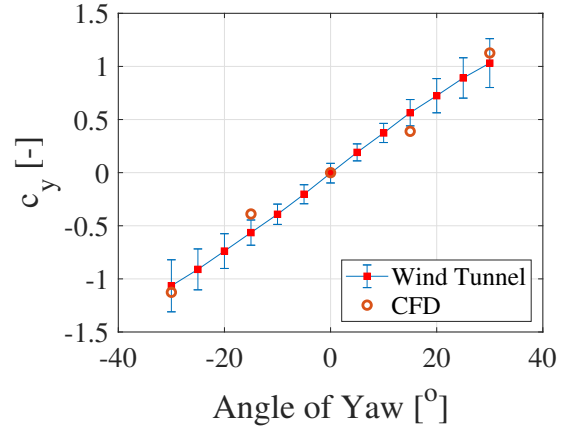


Figure 3.48: Experimental and numerical  $y$  force coefficient as a function of the wind angle of incidence for a  $Re_L = 8.2 \times 10^5$ . Simulations performed with the  $\gamma Re_\theta$  model at still conditions.

As could be observed in figures 3.47 and 3.48, the numerical simulations captures the zero angle of yaw properties accurately, however, once an incidence angle is applied, this is overestimated. Some discrepancies could also be observed in the  $c_y$  measurements at non-zero angles of incidence.

These discrepancies at non-zero angle of incidence were expected. This crosswind condition adds some extra complexity to the studied flow, showing in a clearer way the deficiencies of RANS models. Even though some discrepancies are found between numerical and experimental results, simulation results always stay inside the error bars of the experimental measurements and are capable of revealing the effect that the incidence angle has on both force measurements.

Once again, a study of the boundary layer effects, as well as the higher turbulence intensity seen on the near-floor region of the wind tunnel would be interesting in order to push this validation even further.

### 3.3.2 Pressure Tests

As in the Reynolds effect section, pressure measurements will give a clearer view of the flow properties around the car and will help pointing out some of the biggest differences between numerical and experimental results. A comparison of the pressure distribution at the symmetry line of both is shown in figures 3.49 and 3.50.

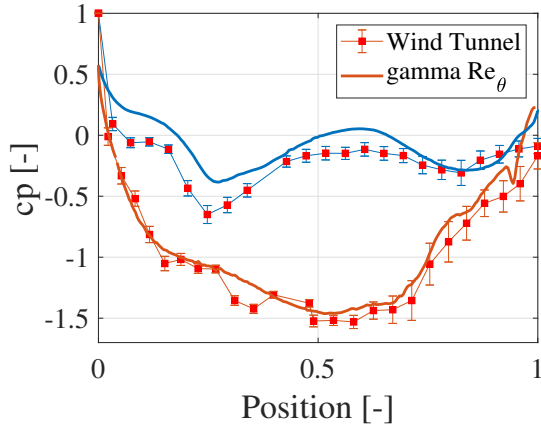


Figure 3.49: Experimental and numerical pressure coefficient distribution measured at Electra’s symmetry plane at an angle of incidence of  $30^\circ$  for a  $Re_L = 8.2 \times 10^5$ . Simulations performed with the  $\gamma Re_\theta$  model at still conditions. Lower surface in blue, upper surface in orange.

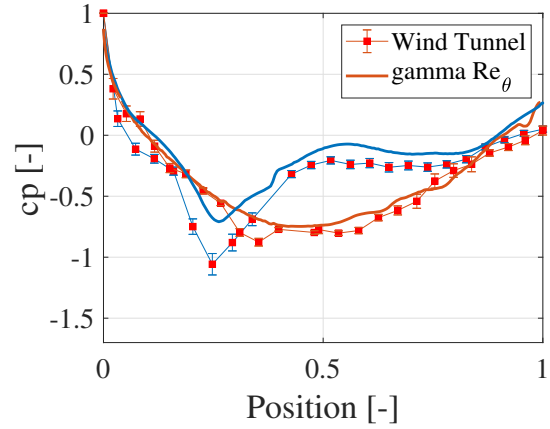


Figure 3.50: Experimental and numerical pressure coefficient distribution measured at Electra’s symmetry plane at an angle of incidence of  $15^\circ$  for a  $Re_L = 8.2 \times 10^5$ . Simulations performed with the  $\gamma Re_\theta$  model at still conditions. Lower surface in blue, upper surface in orange.

Figures 3.49 and 3.50 show a good matching between experimental and numerical results. It is interesting how the higher the angle of incidence the lower the pressure on the upper surface of the car. This is due to the higher acceleration that is induced on the upper part of the car. The opposite is found on the lower side of the car, which augments its pressure value and decreases the suction peak as the angle of incidence is increased. This is due to the higher blockage induced by the wheel fairings on the lower surface. Once again, as for the zero yaw angle case, the numerical simulation is able to capture the upper pressure distribution in a more accurate manner than the lower one. Once again, the higher flow complexity found on the lower side of the car put in evidence the numerical deficiencies shown by RANS models.

A good matching is also found for the cross section plane measurements as shown in figures 3.51 and 3.52.

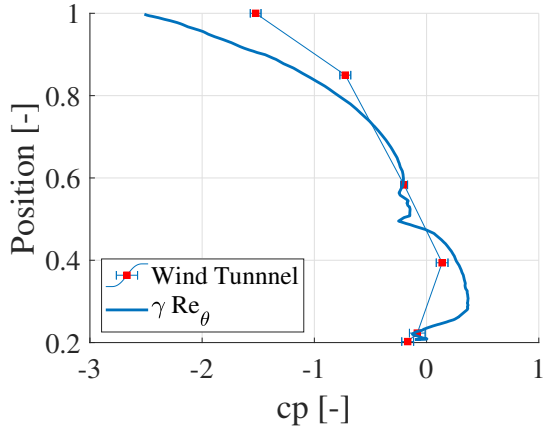


Figure 3.51: Experimental and numerical pressure coefficient distribution measured at Electra’s flow facing side of the cross section plane at an angle of incidence of  $30^\circ$  for a  $Re_L = 8.2 \times 10^5$ . Simulations performed with the  $\gamma Re_\theta$  model at still conditions.

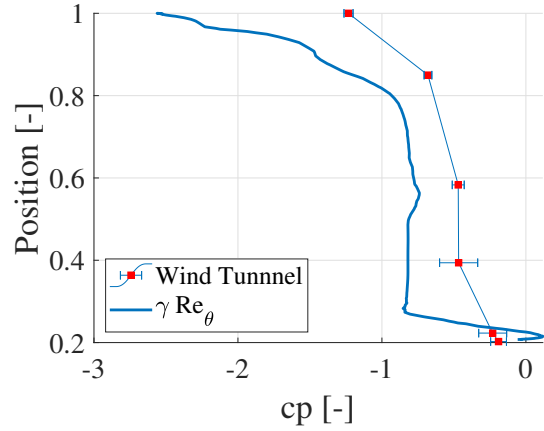


Figure 3.52: Experimental and numerical pressure coefficient distribution measured at Electra’s wake facing side of the cross section plane at an angle of incidence of  $30^\circ$  for a  $Re_L = 8.2 \times 10^5$ . Simulations performed with the  $\gamma Re_\theta$  model at still conditions.

These figures show the obtained results for the cross section plane of the car. The results are divided into flow facing side, which is the side that directly sees the free-stream flow, and wake facing side, which is the side that does not face the free-stream flow. As can be observed, the results obtained with the numerical simulations present a good representation of the flow properties found at the wind tunnel. The direct incidence of the flow on this side of the car helps the flow to remain attached to the car surface, however, this is not the case for the wake facing side. The flow traverses the upper surface of the car with high velocity. This high velocity mixed with the abrupt change in shape of the rotated car induces flow separation. Similarly, the increased complexity of the flow around the rotated low end of the car induces flow separation as well as complex 3D structures. However, even in this side the CFD simulations yielded good results, being possible to observe the effect of this crosswind on the pressure distribution.

It is possible to conclude that the numerical simulations are validated also for crosswind conditions. Some discrepancies were found on the drag coefficient values, where an overestimation of its value was observed on the numerical results. Nonetheless, good results were obtained on  $c_y$  measurements as well as the pressure coefficient distribution.



# Chapter 4

## Advanced aerodynamic studies of Electra

Up to now the still road conditions has been studied and compared to experimental results, however these conditions are not found once the real car hits the track. The car sees a moving track, which directly eliminates the presence of the floor boundary layer and affects the lower passing flow properties, and the wheels rotate, changing the aerodynamic properties of Electra. Moving road conditions will be therefore applied for all simulations present in this chapter. Also many simplifications and assumptions such as completely flawless and smooth surface has been taken into account, therefore a brief qualitative study of these simplifications will be made.

### 4.1 Moving car aerodynamics

As already stated, the effect of moving floor and wheels will directly affect the aerodynamic properties seen by the car. This ground effect will induce a different speed distribution that will affect the pressure seen by the Electra surface and that will directly affect other variables such as the laminar to turbulent transition.

After the numerical-experimental validation, it is possible to push the numerical study even further with confidence in the solution. Due to its good drag results, the robustness that it presented over the entire Reynolds range and the precious information it gives about the turbulence properties around the car, the  $\gamma Re_\theta$  is chosen to perform this study. Nevertheless, one has to bear in mind that the ideally smooth surface will lead to an underestimation of the drag coefficient. This will be taken into account in section 4.2.

#### 4.1.1 Zero yaw angle

The first studies are carried out at purely frontal wind. In order to better understand the aerodynamic properties of Electra, this will be divided into five parts: front, middle

and rear parts, front wheels and rear wheels. This break up of the car will allow to directly observe the contribution of each of the sections, being able to detect regions with optimization potential. A direct comparison between the still and moving road conditions will also be made.

Before studying the obtained results, it is necessary to check that any of the boundary conditions cause any problems. Due to the introduced rotation of the wheels, these could yield some local problems at the interfaces between sections with different boundary conditions.

Both, front and rear wheels turns at a rotation speed  $\omega = 24.5$  rad/s, which allows the wheel to simulate the rolling condition of the real car at its  $Re_{L_{ref}}$ . This rotation could induce some problems on its contact with the track, which uses a translating floor condition instead of a rotating wall boundary condition, and on the intersection between the wheel and the surface that closes the wheel well. This last intersection can be specially problematic, since the non slip condition of the wheel carries the air towards the non-slip wall of the wheel well closure. Figures 4.1 and 4.2 show these regions.

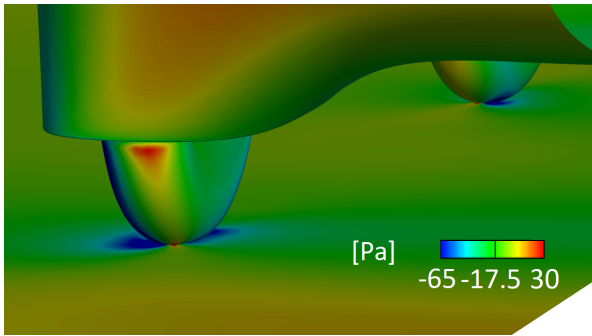


Figure 4.1: Pressure plot wheel detail for moving road conditions. Simulation performed using the  $\gamma Re_\theta$  model at a  $Re_L = 13 \times 10^5$ .

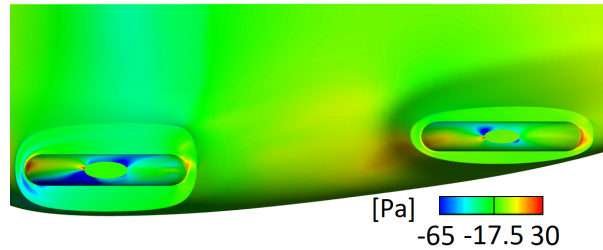


Figure 4.2: Pressure plot wheel detail for moving road conditions. Simulation performed using the  $\gamma Re_\theta$  model at a  $Re_L = 13 \times 10^5$ .

As can be seen in figure 4.1, the interface track-wheel does not causes any issue. Looking at figure 4.2, it is possible to observe how the rotation of the wheel induces some increase in the pressure seen at the rear of each of the wheels, however, this effect is minimal and do not represent any issue for the solution or the convergence of the simulation.

The main difference between moving and still road conditions is the lower section of the car. Due to the absence of the floor boundary layer, more quantity of air passes through the lower gap between the car and the road. This is clearly seen in the comparison shown in figures 4.3 and 4.4.

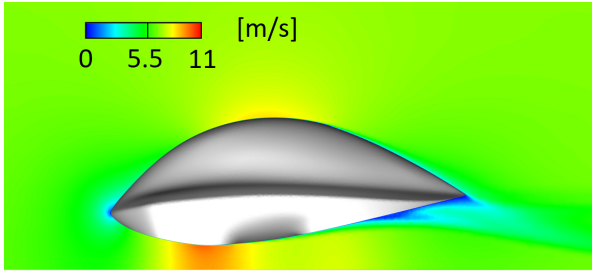


Figure 4.3: Velocity contour plot at the car symmetry plane with moving road conditions. Simulation performed using the  $\gamma Re_\theta$  model at a  $Re_L = 13 \times 10^5$ .

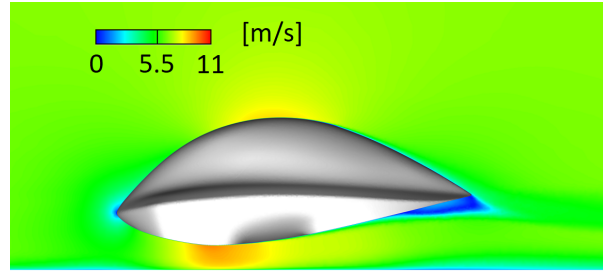


Figure 4.4: Velocity contour plot at the car symmetry plane with still road conditions. Simulation performed using the  $\gamma Re_\theta$  model at a  $Re_L = 13 \times 10^5$ .

In figures 4.3 and 4.4, a clear difference is found between the moving and the still road conditions. The lower narrower section of the gap between the car and the track shows a larger and more intense red region in the moving road conditions. This is due to the lower blockage effect that the moving road creates, allowing more air to pass through the lower section. The higher velocity and flow volume affects also the rear, which sees a sooner separation of the boundary layer. This boundary layer detachment presents a much different structure than the one found with still road conditions. This change is also quite perceptible when looking at the turbulent kinetic energy (figures 4.5 and 4.6).

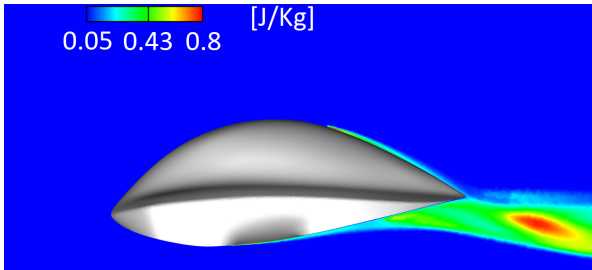


Figure 4.5: Turbulent kinetic energy contour plot at the car symmetry plane with moving road conditions. Simulation performed using the  $\gamma Re_\theta$  model at a  $Re_L = 13 \times 10^5$ .

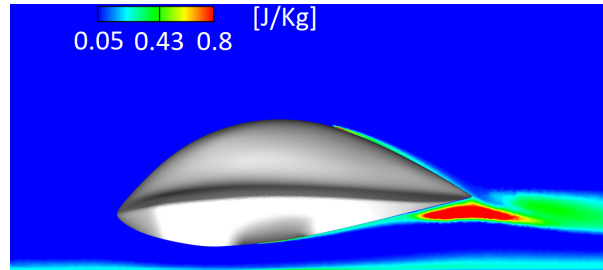


Figure 4.6: Turbulent kinetic energy contour plot at the car symmetry plane with still road conditions. Simulation performed using the  $\gamma Re_\theta$  model at a  $Re_L = 13 \times 10^5$ .

As shown in figures 4.5 and 4.6, the higher velocity of the flow near the floor lowers the pressure below the car, causing the flow to separate more easily on the diffuser zone of

the car. This separation yields a larger turbulent wake than in the still road case, however its intensity near the car is lower, as the high energy bubble that appears at the car tail in the still road conditions is pushed back. This new flow structure also influences the laminar to turbulent transition of the boundary layer as figures 4.7 and 4.8 show.

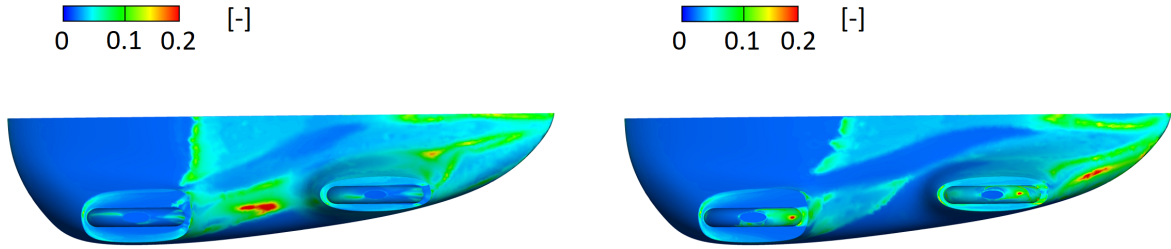


Figure 4.7: Intermittency contour plot at the car lower surface with moving road conditions. Simulation performed using the  $\gamma Re_\theta$  model at a  $Re_L = 13 \times 10^5$ .

Figure 4.8: Intermittency contour plot at the car lower surface with still road conditions. Simulation performed using the  $\gamma Re_\theta$  model at a  $Re_L = 13 \times 10^5$ .

The higher velocity seen by the lower section of Electra triggers turbulence sooner and increases its energy as can be seen comparing figures 4.7 and 4.8. It is also interesting to notice how the rotation of the wheel drastically reduces the presence of turbulence at the wheel. This is due to the lower relative velocity that the rotating wheel has with respect to the free-stream flow.

The obtained aerodynamic coefficients obtained for the moving floor simulation are compared to the ones obtained for the still road conditions in figure 4.9. Many differences in key variables have been observed between both simulation conditions, figure 4.10 shows how these differences impact the results for the total aerodynamic forces acting on the car.

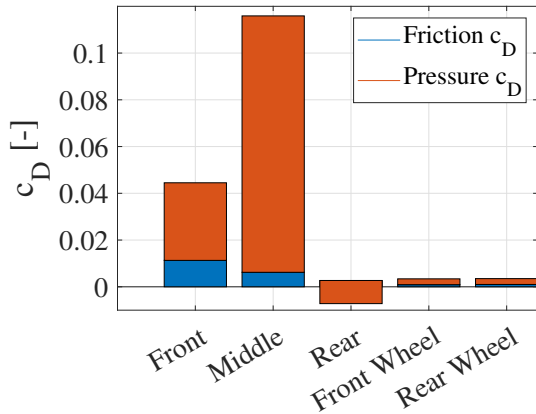


Figure 4.9: Histogram showing the distribution of pressure and friction drag on the different sections of Electra at still road conditions. Simulation performed using the  $\gamma Re_\theta$  model at a  $Re_L = 13 \times 10^5$ .

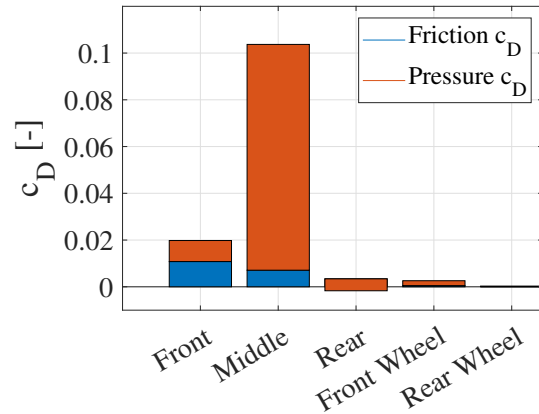


Figure 4.10: Histogram showing the distribution of pressure and friction drag on the different sections of Electra at moving road conditions. Simulation performed using the  $\gamma Re_\theta$  model at a  $Re_L = 13 \times 10^5$ .

As could be observed, the effect of the moving wall boundary condition of the track completely changes the flow properties around the car. On the optimization process, moving car conditions must be therefore taken into account due to the high impact that this has on the aerodynamic performance of the car.

In general, the lower blockage that the moving floor condition induces on the lower part of the car helps reducing drag, which sees a reduction of nearly 35% over the still road conditions. The higher velocity on the lower section of the car creates more suction on this section, making the car to create down-force instead of the lift seen on the still road conditions. This effect is known as ground effect. The ground effect is a well known phenomenon that if well exploited can contribute in a favourable way to the aerodynamic characteristics of a body. A clear example is racing car front wings, where the flow over the wing is highly affected by the distance with respect to the ground, which lowers dramatically the induced drag and increases its effective down-force. Multiple studies concentrate themselves into this phenomenon, allowing for a broad background knowledge.

In order to better understand the drag distribution over the Electra, the pressure distribution over the Electra surface is shown in figures 4.11, 4.12, 4.13 and 4.14.

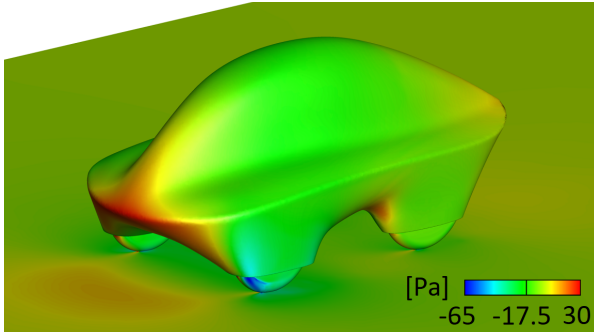


Figure 4.11: Pressure contour plot with moving road conditions. Simulation performed using the  $\gamma Re_\theta$  model at a  $Re_L = 13 \times 10^5$ .

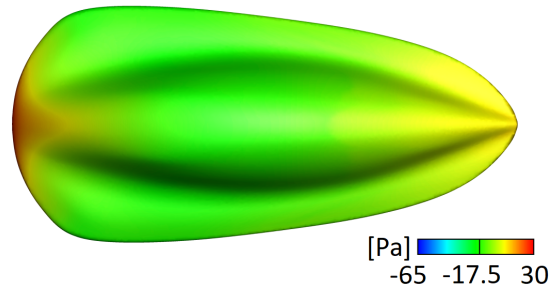


Figure 4.12: Pressure contour plot at Electra top surface with moving road conditions. Simulation performed using the  $\gamma Re_\theta$  model at a  $Re_L = 13 \times 10^5$ .

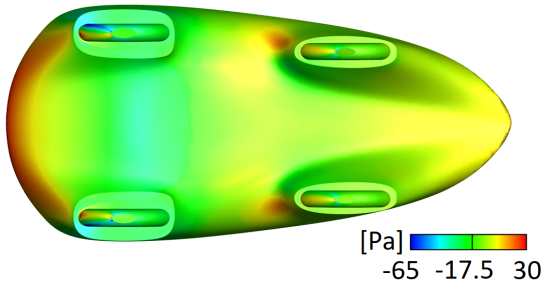


Figure 4.13: Pressure contour plot at Electra lower surface with moving road conditions. Simulation performed using the  $\gamma Re_\theta$  model at a  $Re_L = 13 \times 10^5$ .

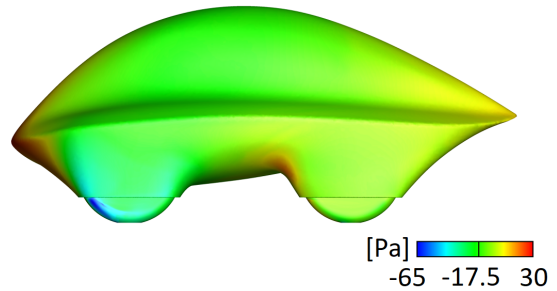


Figure 4.14: Pressure contour plot at Electra side surface with moving road conditions. Simulation performed using the  $\gamma Re_\theta$  model at a  $Re_L = 13 \times 10^5$ .

As can be observed, the frontal area sees a high pressure zone due to the direct impact of the free-stream flow. As a result of the car shape, this region of high pressure is minimized, resulting in a relatively low drag impact.

Focusing now on the middle part of the car, it is possible to observe how pressure decreases on the upper part. The volume of the body accelerates the flow around it, lowering the surface pressure. On the lower part, similar conclusions can be made, however it presents a much richer pressure range. As it was possible to see in section 3.2.2, a suction region is found between the frontal wheels. The stretching that the shape of the car induces on the flow and the effect created by the wheels accelerates the flow reducing the pressure. After this stretching, the lower surface of the car has a diffuser-like shape,

which reduces the flow velocity, yielding an increase in pressure. It is worth noticing how the part of the bodywork covering the rear wheels present high pressure spots. This is one of the main reasons why this middle section represents a high percentage of the total drag.

Thanks to the smooth and streamlined shape of the Electra upper part, the flow remains attached to the surface without presenting any A-pillar vortex as shown in figures 4.15 and 4.16.

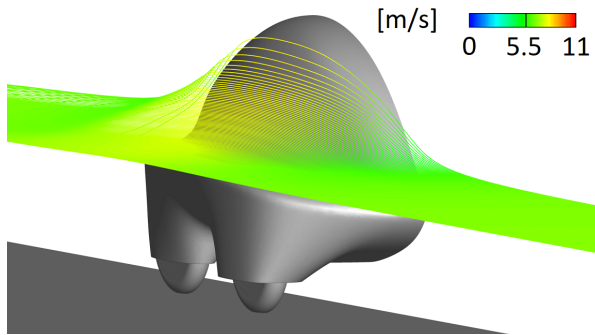


Figure 4.15: Flow streamlines over the Electra upper surface. Streamlines coloured by velocity magnitude. Simulation performed with moving road conditions using the  $\gamma Re_\theta$  model at a  $Re_L = 13 \times 10^5$ .

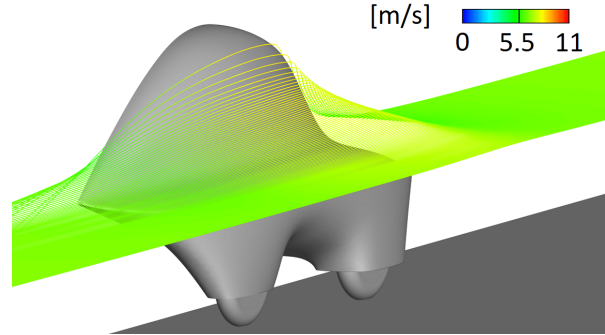


Figure 4.16: Flow streamlines over the Electra upper surface. Streamlines coloured by velocity magnitude. Simulation performed with moving road conditions using the  $\gamma Re_\theta$  model at a  $Re_L = 13 \times 10^5$ .

However, the lower section of the car does not present the same smooth flow pattern as in the upper surface. The shape between the front and rear wheels presents an unnecessary gap that not only causes the flow to impact two frontal surfaces, by also present complex instabilities that increases turbulence. This is clearly seen in figures 4.17 and 4.18, where the increase in flow complexity and turbulent kinetic energy is seen.

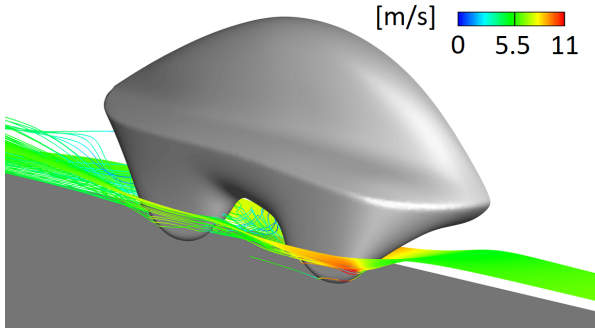


Figure 4.17: Flow streamlines over the Electra lower section. Streamlines coloured by velocity magnitude. Simulation performed with moving road conditions using the  $\gamma Re_\theta$  model at a  $Re_L = 13 \times 10^5$ .

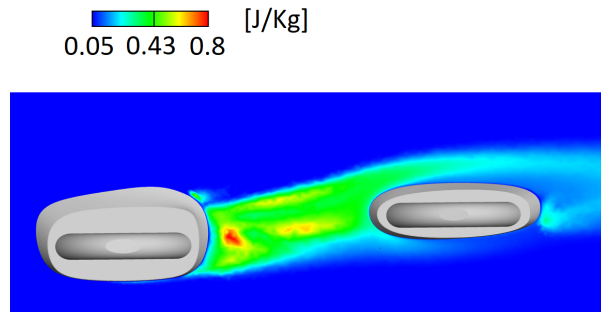


Figure 4.18: Turbulent kinetic energy contour plot at a  $x = 0.15$  m  $y - z$  plane. Simulation performed with moving road conditions using the  $\gamma Re_\theta$  model at a  $Re_L = 13 \times 10^5$ .

It becomes clear that this region of the car is the most critical, being also reflected in the resultant drag coefficient.

Finally, the rear part of the Electra present an increase in pressure, as the reduction in cross section decelerates the flow, increasing the pressure. This increase in pressure coupled with the shape of the car induces a small thrust, helping reducing the drag. Nevertheless, this section could be further improved by modifying the shape of the wheel fairing ending (figures 4.19 and 4.20).

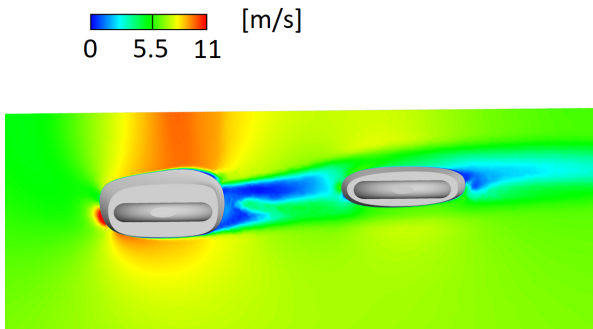


Figure 4.19: Velocity magnitude contour plot at a  $x = 0.15$  m  $y - z$  plane. Simulation performed with moving road conditions using the  $\gamma Re_\theta$  model at a  $Re_L = 13 \times 10^5$ .

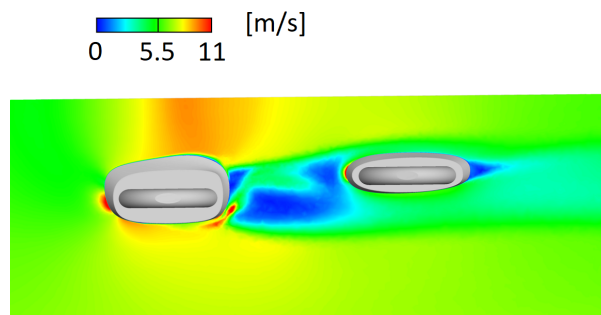


Figure 4.20: Velocity magnitude contour plot at a  $x = 0.15$  m  $y - z$  plane. Simulation performed with still road conditions using the  $\gamma Re_\theta$  model at a  $Re_L = 13 \times 10^5$ .

Figures 4.19 and 4.20 show a region of low speed at the rear of the wheel fairing for both, still and moving conditions. This region could be further improved by modifying the round shape of the wheel fairing.



### 4.1.2 Crosswind conditions

In car aerodynamics, all aerodynamic forces and moments can affect the stability of the vehicle. It is therefore interesting to observe the effect that non-zero angle of yaw conditions has on its aerodynamic properties.

Since the car is designed to travel at zero or low angles of yaw, high incidence angles induces many undesired phenomenons. As could be seen in section 3.3.1, these conditions not only causes the appearance of new force components, but also increases drag considerably. Due to the shape of the car, boundary separations as well as high energy vortices are created. Figures 4.21 and 4.22 show a cross sectional view of the flow velocity field as well as the turbulent kinetic energy.

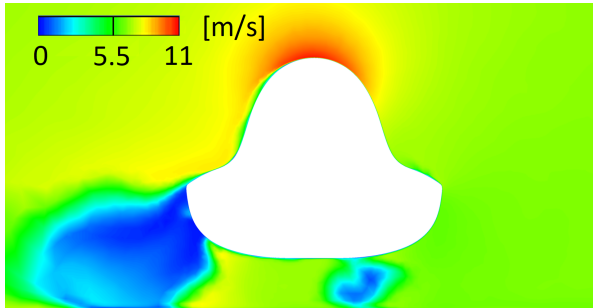


Figure 4.21: Velocity contour plot at the  $x$  plane passing through Electra's highest point. Moving road simulation performed with  $\gamma Re_\theta$  model at  $30^\circ$  crosswind and a  $Re_L = 8.2 \times 10^5$ .

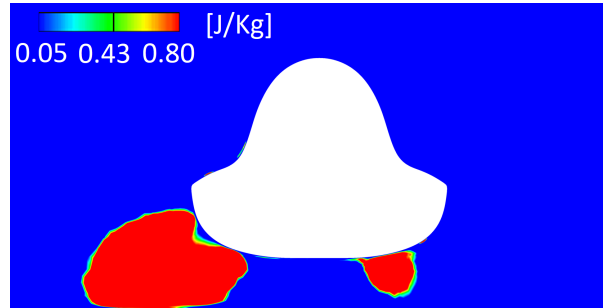


Figure 4.22: Turbulent kinetic energy contour plot at the  $x$  plane passing through Electra's highest point. Moving road simulation performed with  $\gamma Re_\theta$  model at  $30^\circ$  crosswind and a  $Re_L = 8.2 \times 10^5$ .

Figure 4.21 show how a a large low velocity region is found at the car wake. As shown by figure 4.22, this low velocity region presents a high increase in turbulent kinetic energy. These images clearly show that contrary to the zero angle of yaw case, once crosswind is found, Electra's aerodynamics do not perform in the expected way. It is important to bear in mind that these are only 2D plots, but the flow presents a complex 3D behaviour, as shown in figures 4.23, 4.24, 4.25 and 4.26.

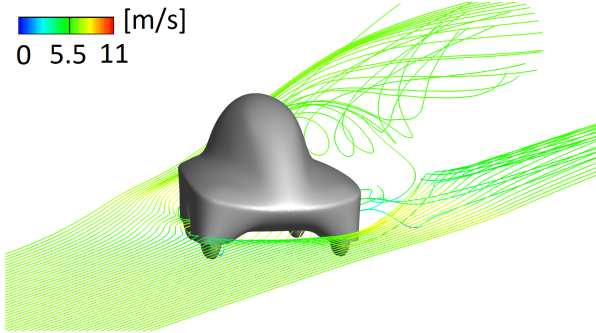


Figure 4.23: Flow streamlines over Electra lower section. Streamlines coloured by velocity magnitude. Moving road simulation performed with  $\gamma Re_\theta$  model at  $30^\circ$  crosswind and a  $Re_L = 8.2 \times 10^5$ .

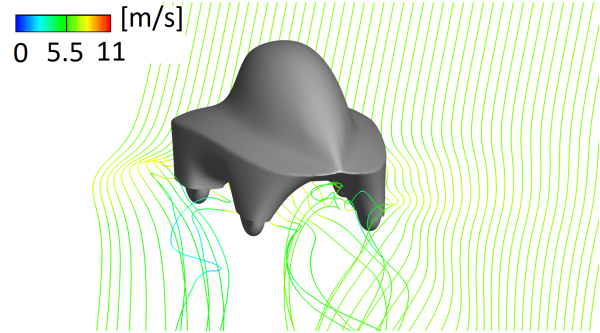


Figure 4.24: Flow streamlines over Electra lower section. Streamlines coloured by velocity magnitude. Moving road simulation performed with  $\gamma Re_\theta$  model at  $30^\circ$  crosswind and a  $Re_L = 8.2 \times 10^5$ .

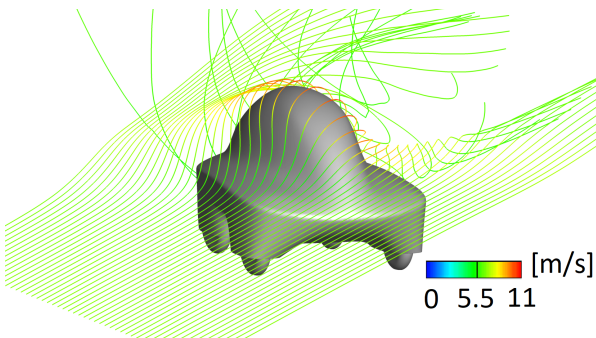


Figure 4.25: Flow streamlines over Electra upper section. Streamlines coloured by velocity magnitude. Moving road simulation performed with  $\gamma Re_\theta$  model at  $30^\circ$  crosswind and a  $Re_L = 8.2 \times 10^5$ .

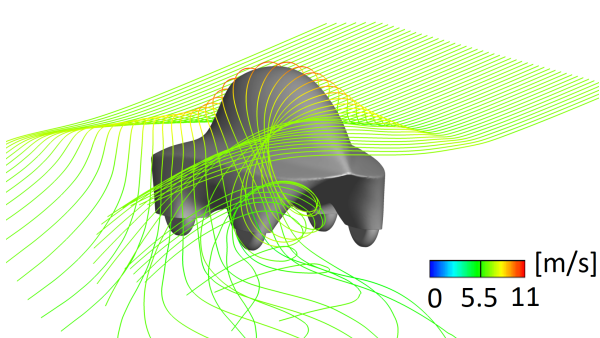


Figure 4.26: Flow streamlines over Electra upper section. Streamlines coloured by velocity magnitude. Moving road simulation performed with  $\gamma Re_\theta$  model at  $30^\circ$  crosswind and a  $Re_L = 8.2 \times 10^5$ .

With crosswind conditions, the car does not behave like a streamlined shape any more, and large vortices can be observed behind the vehicle. The lower passing streamlines (figures 4.23 and 4.24), show two vortex structures once the flow passes the vehicle. The angle of incidence of the wheel fairings mixed with the complexity of the lower surface makes these vortices to appear. Due to the diffuser present at the rear of the car, more flow is conducted through this cavity instead of passing in between the wheel fairings, that creates a blockage effect on the flow. This phenomenon makes the diffuser vortex much larger than the other one.

The upper surface flow shown in figures 4.25 and 4.26 see how due to the elongated

shape of the car, this acts like a vortex generator. While the streamlines passing through the front of the car follows the curvature of the car being deviated in the car direction, on the rear part of the car, the reduction in height makes the streamlines continue without deviating. Both streamlines meet each other behind the vehicle, creating a high energy vortex due to the difference in direction.

Crosswind conditions not only affects the flow structures, but also the transition from laminar to turbulence. The intermittency contour plots on Electra’s surface are shown in figures 4.27 and 4.28.

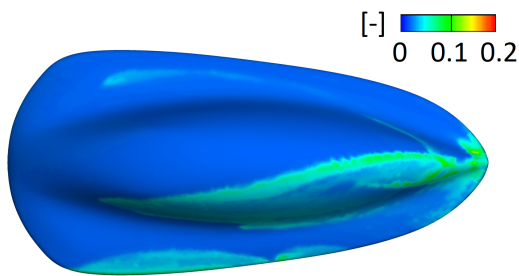


Figure 4.27: Intermittency contour plot at Electra’s upper surface. Moving road simulation performed with  $\gamma Re_\theta$  model at  $30^\circ$  crosswind and a  $Re_L = 8.2 \times 10^5$ .

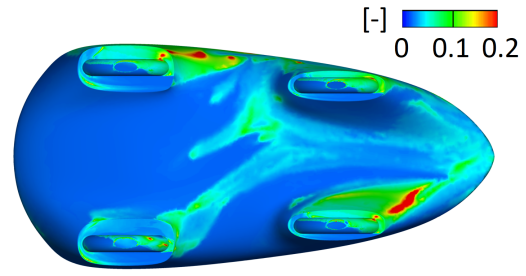


Figure 4.28: Intermittency contour plot at Electra’s lower surface. Moving road simulation performed with  $\gamma Re_\theta$  model at  $30^\circ$  crosswind and a  $Re_L = 8.2 \times 10^5$ .

As can be observed, the intermittency plots show a completely different behaviour of the turbulent transition. On the upper surface it is possible to observe how the direct incidence of the flow on the car side helps reducing drastically the presence of a turbulent boundary layer, however, this is not the case once the crest of the car is surpassed. The slight detachment seen at the canopy in figure 4.21 triggers the transition to turbulence. On the lower side, the two wheel fairings directly triggers turbulence. It is also important to notice how the turbulent region drastically augments on the wake side of the car. This is due to the huge detachment zone observed in figure 4.21.

These non-symmetric properties introduce new aerodynamic forces and moments that could affect the stability properties of the car. Figures 4.29 and 4.30 show the behaviour of these forces and moments as a function of the angle of incidence. All the presented moment coefficients are calculated at  $x=1.4$  m and with a reference length of 1 m.

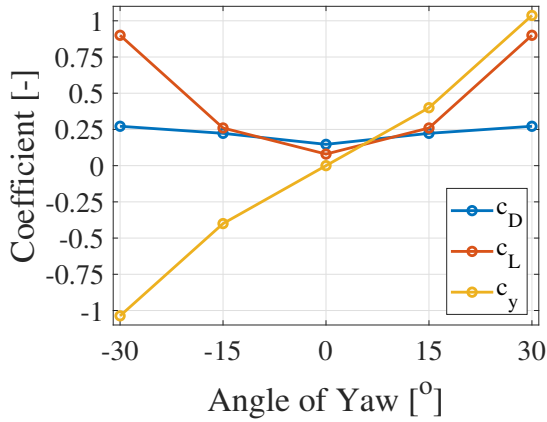


Figure 4.29: Drag, lift and  $y$  force coefficient as a function of the angle of yaw. Simulation performed with the  $\gamma Re_\theta$  model with moving conditions at a  $Re_L = 8.2 \times 10^5$ .

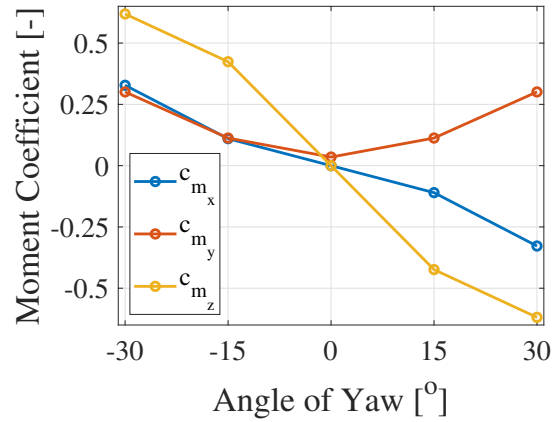


Figure 4.30:  $x$ ,  $y$  and  $z$  moment coefficient as a function of the angle of yaw. Simulation performed with the  $\gamma Re_\theta$  model with moving conditions at a  $Re_L = 8.2 \times 10^5$ .

As can be seen, the forces and moments acting on the car dramatically changes as a function of the angle of yaw. Due to the varying conditions that are given at the race, a dynamic behaviour of these coefficients would be observed, changing the driving characteristics of the car.

## 4.2 Effect of simplifications and surface irregularities

Previously, a simplified and idealized geometry has been used, however a real car is far from being perfect. Screws, rear-view mirrors, wipers and open wheel wells are some examples of the many imperfections that are not taken into account within the numerical model. What is the effect of these simplifications? Answering this question will be the goal of this section.

### 4.2.1 Wheel and well simplification

As already stated, the CAD model used in the simulations does not model the wheel well, and consequently the effect of the wheel that remains inside this cavity is not taken into account. What is the order of magnitude of the error introduced by this simplification?

Morelli [16] and Scibor-Rylski [11] concluded that if only the not covered part of the wheel is taken as reference projection area, the drag coefficient does not change significantly. This affirmation allows to study the drag coefficient of a fully exposed wheel and

then obtain an approximation of the drag that the partially plunged wheel would create. Figure 4.31 present the results obtained by A.J. Scibor-Rylski for multiple wheel plunging configurations.

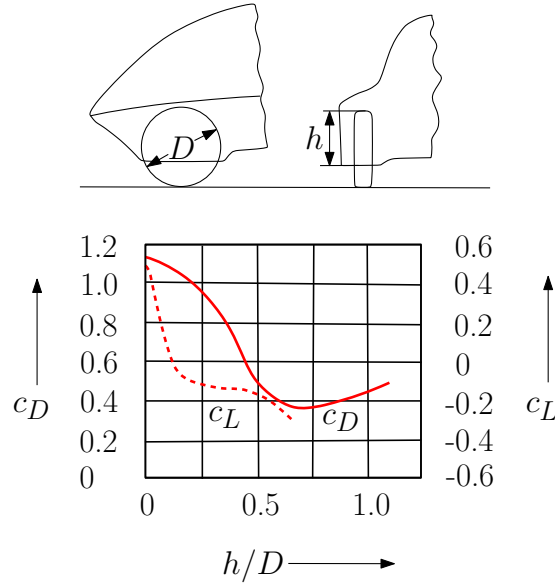


Figure 4.31: Effect of vertical position  $h$  on the wheel lift and drag coefficients. Adapted from [11]

The wheels used by Electra are 95/80 R16 tyres by Michelin. These tyres are much thinner than the ones used in commercial cars, allowing for a much reduced frontal area and better aerodynamic performance.

These wheels are mounted on carbon fibre disc shaped rims. These type of rims are widely used when drag is paramount, such as in time trial bikes or racing cars. This type of rim present two major inconvenient: stability issues in cycling and brake refrigeration issues for racing vehicles. None of these issues affect the Electra, becoming the perfect rim choice.

In order to carry out the estimation of the wheel drag, the aerodynamic properties of the exposed wheel will be studied. For these simulations, the  $\gamma Re_\theta$  model will be used. As for the applied conditions, all combinations of moving or fixed floor and rotating or fixed wheel will be taken into account in order to observe the effect that each element has on the final coefficients. As one could expect, moving road conditions will be used to estimate the real drag of the wheel, meaning that the rotation of the wheel and the movement of the floor will be taken into account. Table 4.1 shows the obtained resultant aerodynamic coefficients for the different cases of the wheel.

Set-up	$c_D$	$c_L$
Stationary set-up	0.348	0.165
Moving Wheel, still road	0.311	-0.146
Moving Road, still wheel	0.329	0.128
Moving Wheel and Road	0.311	-0.201

Table 4.1: Electra exposed wheel drag and lift coefficient for different combinations of road and wheel conditions. Simulations performed with the  $\gamma Re_\theta$  model and a  $Re_L = 13 \times 10^5$ .

As can be observed in table 4.1, the drag coefficient is slightly reduced when the rotation of the wheel is taken into account, while the lift coefficient drastically decreases. In order to understand the cause of this changes, figures 4.32, 4.33, 4.34 and 4.35 show the pressure and velocity magnitude distribution over the wheel.

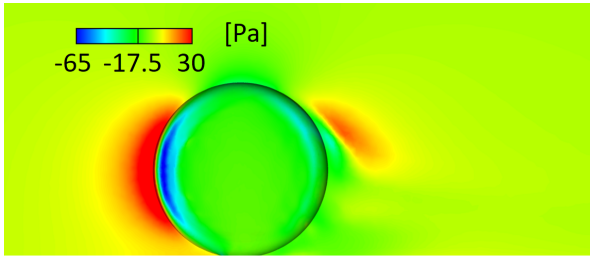


Figure 4.32: Pressure contour plot over a still wheel. Simulation performed with  $\gamma Re_\theta$  model and still road conditions with a  $Re_L = 13 \times 10^5$ .

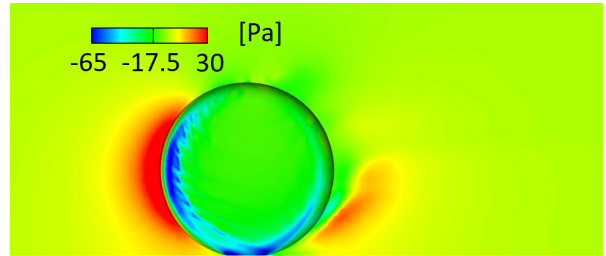


Figure 4.33: Pressure contour plot over a rotating wheel. Simulation performed with  $\gamma Re_\theta$  model and moving road conditions with a  $Re_L = 13 \times 10^5$ .

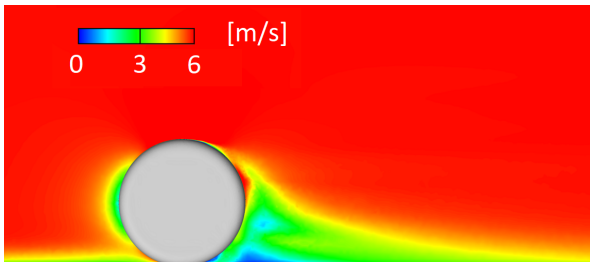


Figure 4.34: Velocity magnitude contour plot over a still wheel. Simulation performed with  $\gamma Re_\theta$  model and still road conditions with a  $Re_L = 13 \times 10^5$ .

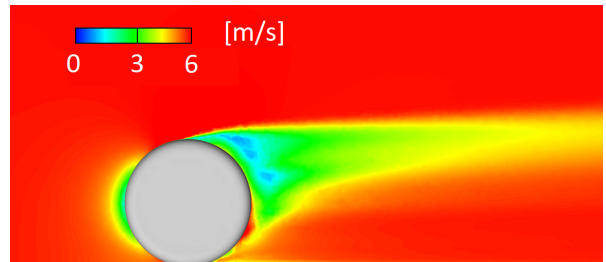


Figure 4.35: Velocity magnitude contour plot over a rotating wheel. Simulation performed with  $\gamma Re_\theta$  model and moving road conditions with a  $Re_L = 13 \times 10^5$ .

It is clear that the rotation speed applied to the wheel helps lowering the pressure seen by the front of the wheel, which causes a decrease in drag, however other 3D effects due to the rotation of the wheel (figure 4.36) prevent a drastic decrease of the lift. As can be seen on the velocity contour plots shown in figures 4.34 and 4.35, it is clear that an up-wash velocity is induced to the flow. This up wash velocity is the cause of the down-force created by the wheel.

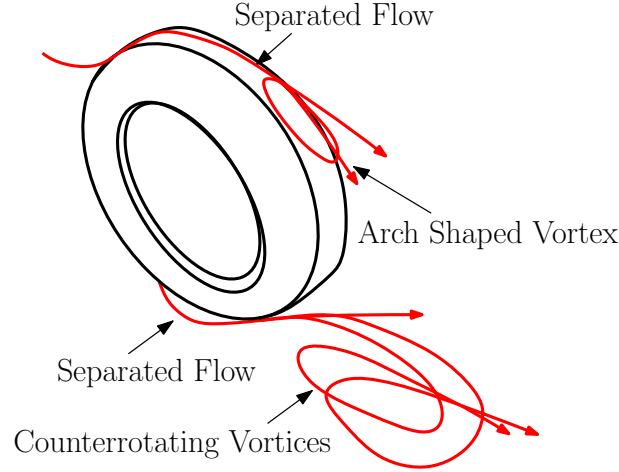


Figure 4.36: 3D flow structures induced by a rotating wheel.

It is now possible to estimate the new  $c_D$  of the wheel, this time taken into account the effect of the plunged wheel and the wheel housing. 77% of the Electra wheels are plunged inside the well, meaning that only 23% of the wheel is exposed. Bearing in mind that if one takes the exposed wheel area into account, the drag coefficient does not change, the drag of the plunged wheel can be corrected as follows:

$$c_D = \frac{D_{Exposed}}{1/2\rho v_{Exposed}^2} = \frac{D_{plunged}}{1/2\rho v_{Plunged}^2}; \quad (4.2.1)$$

$$D_{Plunged} = D_{Exposed} \frac{A_{Plunged}}{A_{Exposed}}. \quad (4.2.2)$$

Computing the wheel drag coefficient based on Electra's projection area, yields a  $c_D = 0.002$ . This contribution must be multiplied by four in order to take into account all the wheels. Table 4.2 shows a clear comparison of the wheel effect on the Electra aerodynamics.

<b>Configuration</b>	$c_D$	$c_L$
No Wheels	0.099	-0.123
With Fixed Wheels	0.166	0.069
With Rolling Wheels	0.146	-0.170
With Wheel Well Correction	0.151	-0.170

Table 4.2: Effect of wheels on the drag and lift coefficients of the car. Simulation performed with  $\gamma Re_\theta$  model and a  $Re_L = 13 \times 10^5$ .

This remains an estimation of the real effect that the wheel well cavity has on the aerodynamic properties of the car. Other effects 3D are still to be taken into account such as the effect of the wheel housing to wheel volume ratio, or the crosswind induced by the front shape of the car on the front wheels.

### 4.2.2 Rear-view mirrors

Many simplifications have been made to the original car shape. After the wheel well simplification, one of the most important simplifications is the absence of rear-view mirrors.

The rear-view mirrors are an essential part of the vehicle, but due to its shape, they are not aerodynamically efficient, and at high velocities, such as a car in a motorway, the vortex shedding created by the mirrors can be a large source of wind noise inside the cabin. In this section, an estimation of their aerodynamic properties will be performed, in order to correct the results obtained with the simplified model.

A simplified CAD geometry of the Electra rear-view mirror with the same key dimensions was performed in Catia (figures 4.37 and 4.38).

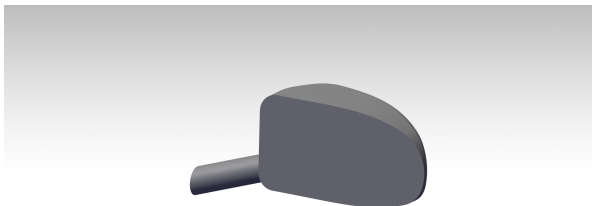


Figure 4.37: Catia 3D model of the rear-view mirror.

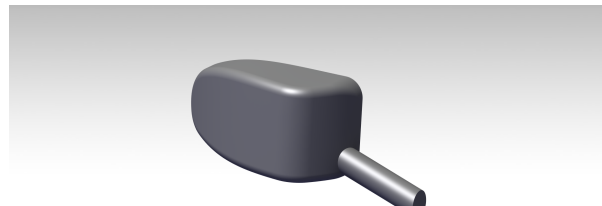


Figure 4.38: Catia 3D model of the rear-view mirror.

Due to the shape of the car, the flow speed seen by the mirrors is different from the free-stream velocity, being therefore necessary to compute this velocity. Using the simulation performed with the real scale Electra in moving road conditions, this flow



velocity magnitude seen by the rear-view mirror was found to be of 8.2 m/s when a free-stream velocity of 6.94 m/s (25 km/h, which represent the reference  $Re_{Lref}$ ) is used.

For this simulation the used domain was modified to fulfill the needs of this simulation. The main change over the car simulation is the absence of track inflation layer and the position of the mirror, which stays at the middle of the domain full height attached to the symmetry wall, in order to simulate the presence of the car. Slip wall condition was applied to all the domain walls excluding the mirror and the inlet-outlet sections. As already mentioned, the unsteady properties of the flow around a rear-view mirror makes the use of URANS simulations mandatory.

While the lift coefficient varied showing values that ranged between 0.05 and -0.05, the drag coefficient stabilized to a constant value. As expected, the rear-view mirror did not present good aerodynamic properties, showing a drag coefficient of  $c_D = 0.51^1$ . The cause of this elevated drag is the shape of the mirror. Figures 4.39 and 4.40 show some flow visualization around the mirror region.

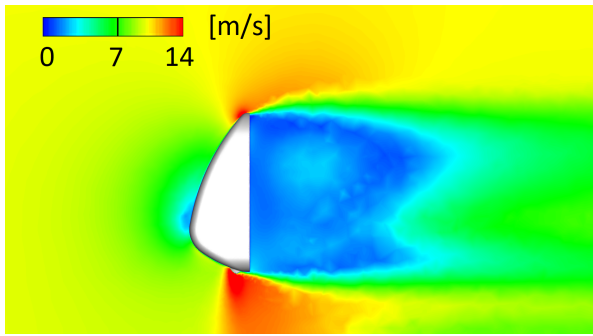


Figure 4.39: Velocity magnitude contour plot in a  $z$  plane crossing the rear-view mirror (Upper side seen). Simulation performed with the  $\gamma Re_\theta$  model with a free-stream velocity of 8.2 m/s.

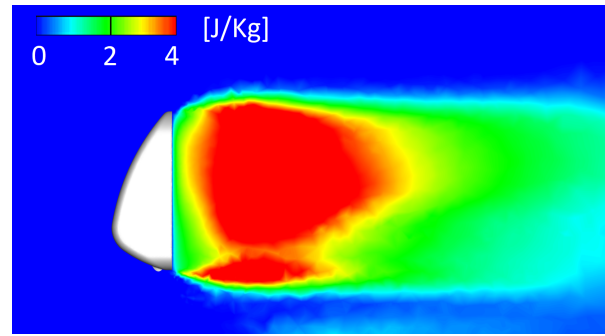


Figure 4.40: Turbulent kinetic energy contour plot in a  $z$  plane crossing the rear-view mirror (Upper side seen). Simulation performed with the  $\gamma Re_\theta$  model with a free-stream velocity of 8.2 m/s.

As can be observed, the shape of the mirror leading edge helps reducing the size of the low speed region, showing a small blue zone at its front. Then, due to the fast increase in width the flow is highly accelerated at its widest position, however, the flattened rear part of the rear-view mirror induces a large low-speed region. This sudden discontinuity that the rear-view mirror presents causes a big increase in the turbulence kinetic intensity behind it.

Then, how does the rear-view mirror affect Electra's aerodynamics? The two rear-view mirrors adds a drag coefficient contribution of  $c_{D_{Mirror}} = 0.012$ . Taking the correction

<sup>1</sup>Drag coefficient calculated with a reference speed  $v_{ref} = 8.2$  m/s and the rear-view mirror projection area as reference area  $A_{ref}$

of the wheel-well simplification into consideration, the total drag coefficient of Electra becomes  $c_D = 0.163$ .

As could be observed, the rear-view mirrors do represent a large source of drag and their shape optimization as well as its position should be further studied since could drastically reduce its effect.

### 4.2.3 Surface imperfections

A real car do not present an ideally smooth and continuous bodywork, instead, wholes, screws and other surface protuberances disrupt the flow around the car. This section will present the effect that these elements can have on the car drag and how they could be potentially improved.

One surface imperfection that is present in all vehicles is the joint between different pieces. The car door, the wheel lids or the rear cover are separate pieces that are not part of the bodywork structure. These joints are so thin that they could be assumed to be placed inside the car boundary layer. By taking this assumption, as explained by S.F. Hoerner [12], an independent drag coefficient based on the effective dynamic pressure can be derived. Depending on how these joints between pieces are made, the resultant drag introduce could vastly vary. Figure 4.41 shows the independent drag coefficient obtained for different joint configurations.

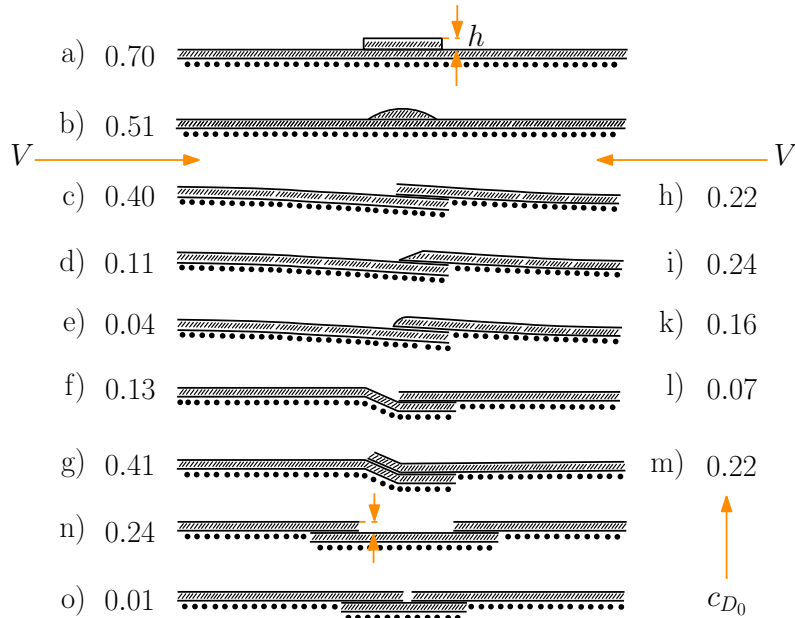


Figure 4.41: Independent drag coefficient of various joints configurations based on thickness “h”. Adapted from [12].

Electra uses *c)* type joints for the wheel covers. It is clear that the aerodynamic properties of these joints could be highly improved, as this configuration shows an elevated drag for both directions of the flow.

Another joint is seen on top of the bodywork-door gap. Even though this strip clearly lowers the aerodynamic effect of this gap, this joint could be considered an *a)* type joint. In order to improve this joint, the closing-gap strip could be mounted on the inside of the car instead than on the outside, turning this joint into an *n)* or *o)* type, improving its drag effect between 65% and 98%.

Finally, an *n)* or *o)* type joint is found at the rear cover. In order to reduce its drag effect even more, the distance between the bodywork and the cover could be minimized in order to reach closer values to the ones of the *o)* case.

Another important surface imperfection that can be found on Electra's surface is the presence of bolt heads. Figure 4.42 shows drag coefficient values for different types of bolts and rivets.

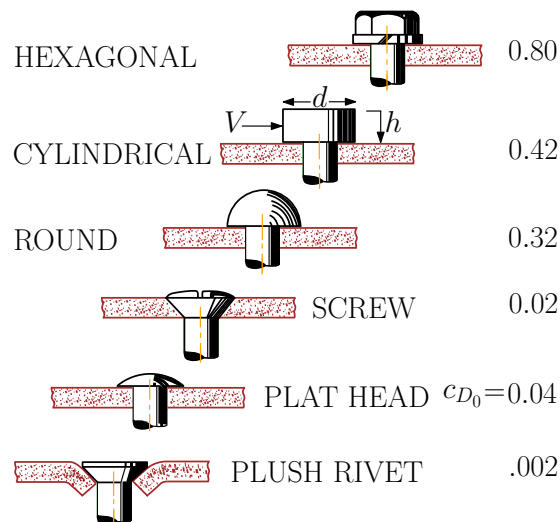


Figure 4.42: Independent drag coefficient of surface bolts and rivets. Adapted from [12].

Electra uses plat head bolts in the vast majority of its bodywork. These were used in order to disrupt in the slightest possible way the flow around the car, and it is confirmed by the results obtained by S.F. Hoerner [12]. As can be observed, there is a large difference between the round and plat head bolt, therefore, in order to improve even more the efficiency of the car, flatter bolts could be used.

Cylindrical bolts are used at the top of the door. Contrary to the plat head bolts, these type of bolt do not present an optimum shape, being therefore an improvement point for future projects.

Another point of interest of surface bolts is the big dependence of its drag coefficient on its elevation with respect to the surrounding surface. This effect is clearly seen in figure 4.43.

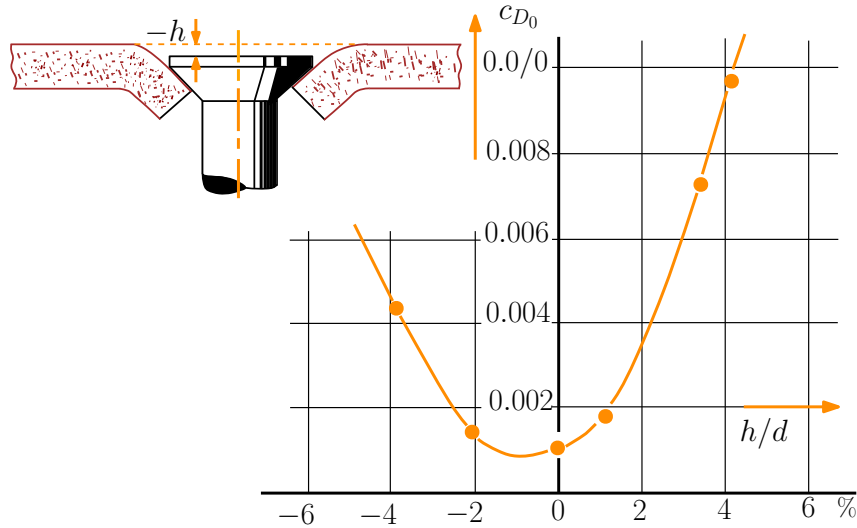


Figure 4.43: Rivet independent drag coefficient as a function of its relative elevation with respect to the surface. Adapted from [12].

As one can see, the height plays a major role in the aerodynamic properties of the bolt head, being clear that the lowest elevation with respect to the surface must be searched. Electra presents bolt washers between the car surface and the bolt itself, elevating artificially its height. Removing these washers could improve the bolts aerodynamic properties.

The last major protuberance present on Electra's surface is the wiper. Physical wipers are mandatory as part of the Shell Eco Marathon rules, since the pilot's vision could be severely affected by rainy conditions. Nonetheless, Electra's wiper idle position could be improved. At the moment, the wiper does not rest in a completely vertical position, inducing a barrier effect on the completely smooth flow circulating on Electra's front surface. This not only affects the pressure distribution seen by the car's surface, but also potentially triggers turbulence much sooner than in simulations. In order to minimize this effect, the wiper could yield in a fully vertical position, minimizing pressure drag and reducing the surface of turbulent boundary layer.

As well as the wiper, all other car protuberances feed the turbulent layer causing turbulence to appear sooner than in the transition simulations, therefore, the real drag coefficient of the car would yield a higher value than the  $c_D = 0.163$  obtained applying the wheel and rear-view mirror correction to the  $\gamma Re_\theta$  results. Figure 4.44 shows a summary of the obtained drag coefficients in this section.

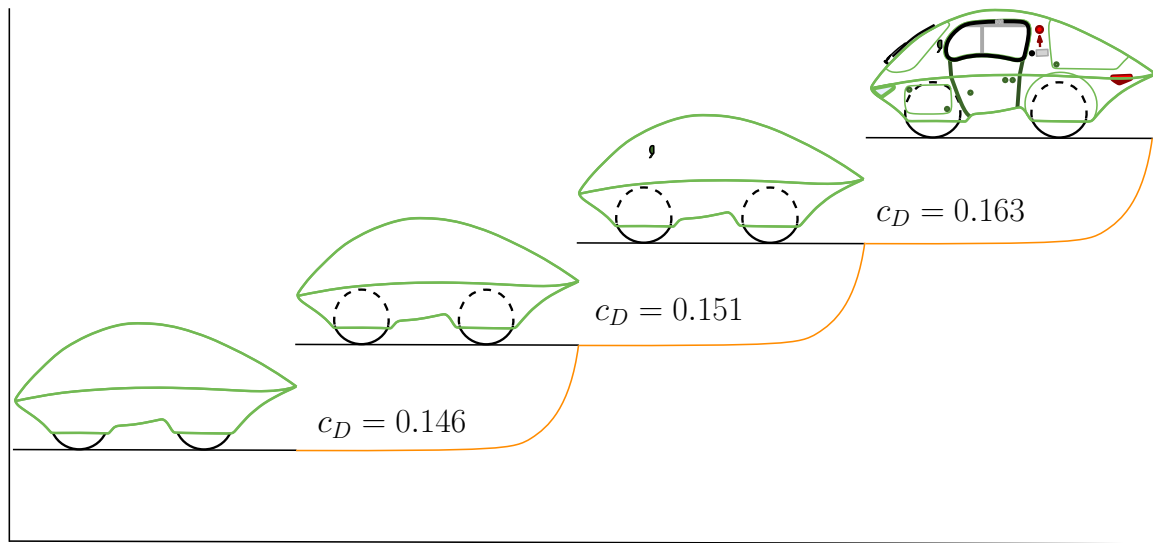


Figure 4.44: Electra drag coefficient and effect of the different simplifications. Simulation performed with the  $\gamma Re\theta$  model at moving road conditions and a  $Re_L = 13 \times 10^5$ .

# Chapter 5

## Aerodynamic modifications of the Electra

All previous sections allowed to have a deep understanding of the aerodynamic characteristics of Electra. These studies will permit to optimize its shape in order to reach lower drag values, improving Electra's efficiency. Later, the effect of a new chassis concept for future projects will also be studied. In order to not confuse the reader, the  $A_{ref}$  of the original Electra is used to calculate all drag coefficients.

### 5.1 Improving performance

This section will have as only purpose the drag reduction of the actual *A&M* car: the Electra. While Electra's upper surface showed up as a solid performing design that delays in a satisfactory manner the transition from laminar to turbulent and allows the flow to remain attached to its surface, it was not the case for the lower surface, where the gap between the wheels induced high energetic turbulent wakes and created 3D structures that triggered turbulence much sooner than the upper part. This section will concentrate on the effect that the car height can have on its drag values and shape modifications of the bodywork in order to solve some of the identified issues.

#### 5.1.1 Height effect

For bodies in ground effect, the height with respect to the ground can highly modify their aerodynamic characteristics, it is therefore important to study its effect. For this study multiple heights, starting from the original height and increasing it up to 45 mm in steps of 15 mm, were tested at still road and moving conditions, such that the influence of the ground effect is clearly visible. Table 5.1 shows the obtained results.

Height	Still conditions $c_D$	Moving conditions $c_D$
Original	0.166	0.146
+ 15 mm	0.168	0.121
+ 30 mm	0.165	0.128
+ 45 mm	0.163	0.112

Table 5.1: Electra drag coefficient comparison between still and moving road conditions for different car heights. Simulations performed with  $\gamma Re_\theta$  model and a  $Re_L = 13 \times 10^5$ .

As could be seen in table 5.1, in the still road case, there is a slight increase in the drag coefficient for the first height increase, however, after this +15 mm configuration, there is a decrease in the drag as the height increases. This decreasing drag effect is even more notorious in the case of the moving configuration which sees a steeper and monotonous decrease of the drag value as a function of the height, being this reduced up to nearly 25% compared to the original configuration drag. A comparison of the speed map at the Electra symmetry plane is shown in figures 5.1 and 5.2.

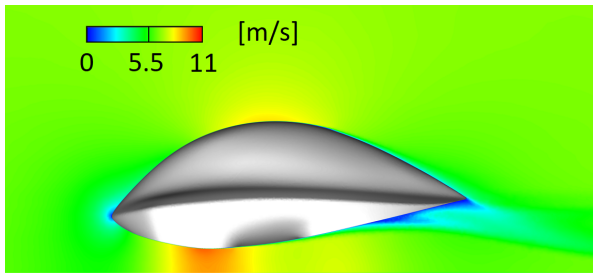


Figure 5.1: Velocity contour plot at the car symmetry plane with moving road conditions. Simulation performed using the original geometry and the  $\gamma Re_\theta$  model at a  $Re_L = 13 \times 10^5$ .

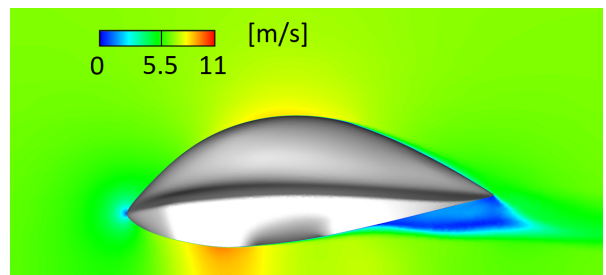


Figure 5.2: Velocity contour plot at the car symmetry plane with moving road conditions. Simulation performed using the original geometry with increased height of 45 mm and the  $\gamma Re_\theta$  model at a  $Re_L = 13 \times 10^5$ .

In figures 5.1 and 5.2, it is possible to observe how the lower flow properties are highly influenced by this height increase. The blockage effect at the lower part of the Electra is decreased and the increased distance from the ground to the tail induces a high separation region. This high difference between both cases are also caused by the difference of the 3D structures that takes part in the studied case.

One can therefore conclude that for this geometry, an increase in the height would help reducing the aerodynamic drag. This aerodynamic strategy is seen in other kind of competitions such as the solar challenge, in which high body cars are commonly used. A

car is a complex project in which other variables such as mechanics must be taken into account, being sometimes difficult to implement changes of this type.

### 5.1.2 Shape modifications

The main focus of this section will be the lower part of the car. As already seen in section 4.1.1, the middle part of the car is the section with the highest optimization potential. Its high drag contribution makes this section ideal to reduce drag in a significant manner.

As previously seen, the gap between the front and rear wheel fairings induces many undesired phenomena. In order to avoid these effects, the first modification will consist on adding a skirt type structure between both wheel fairings. The modified 3D model is shown in figures 5.3 and 5.4.

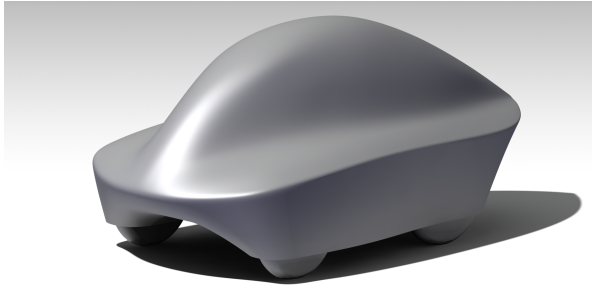


Figure 5.3: 3D model of the first modification based on performance.

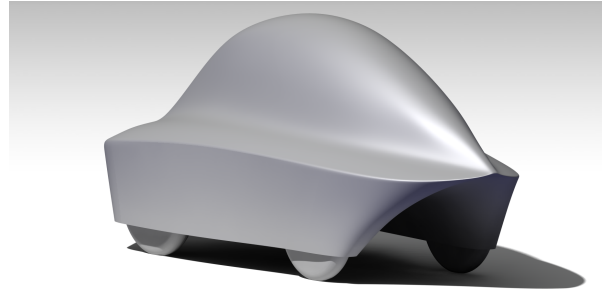


Figure 5.4: 3D model of the first modification based on performance.

The obtained drag coefficient, as well as a direct comparison to the original model in still and moving road conditions are shown in table 5.2.

3D Model	Condition	$c_D$	Viscous $c_D$
Original	Still	0.166	0.022
Original	Moving	0.146	0.036
1 <sup>st</sup> Modification	Still	0.119	0.023
1 <sup>st</sup> Modification	Moving	0.096	0.022

Table 5.2: Drag coefficient comparison between Electra and the first performance modification at still and moving road conditions. Simulations performed with  $\gamma Re_\theta$  model and a  $Re_L = 13 \times 10^5$ .

The drag coefficient sees an important decrease as shown in table 5.2 for both tested cases, obtaining a 28.3% reduction in the still road conditions and 33.4% for the moving



road conditions. A comparison of the turbulent kinetic as well as the velocity is made in figures 5.5, 5.6, 5.7 and 5.8.

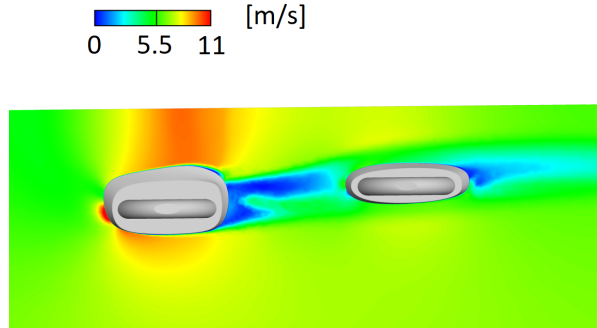


Figure 5.5: Velocity magnitude contour plot at a  $x = 0.15$  m  $y-z$  plane. Simulation performed with Electra at moving road conditions using the  $\gamma Re_\theta$  model at a  $Re_L = 13 \times 10^5$ .

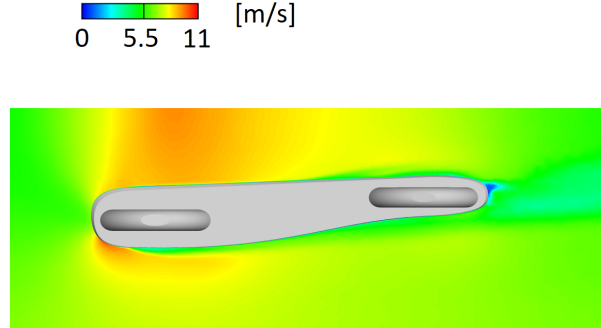


Figure 5.6: Velocity magnitude contour plot at a  $x = 0.15$  m  $y-z$  plane. Simulation performed with the first performance modification at moving road conditions using the  $\gamma Re_\theta$  model at a  $Re_L = 13 \times 10^5$ .

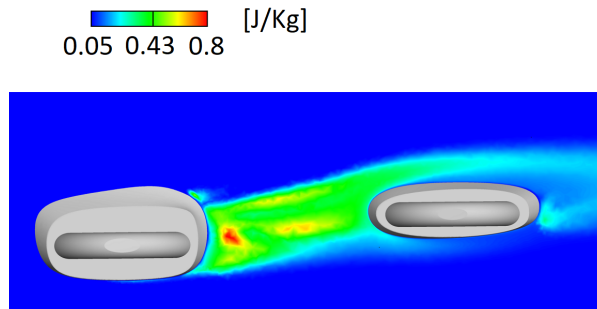


Figure 5.7: Turbulent kinetic energy contour plot at a  $x = 0.15$  m  $y-z$  plane. Simulation performed with Electra at moving road conditions using the  $\gamma Re_\theta$  model at a  $Re_L = 13 \times 10^5$ .

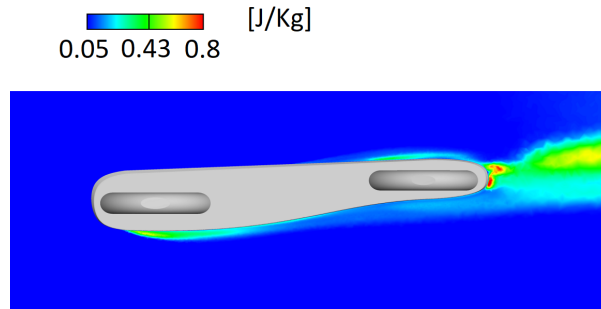


Figure 5.8: Turbulent kinetic energy contour plot at a  $x = 0.15$  m  $y-z$  plane. Simulation performed with the first performance modification at moving road conditions using the  $\gamma Re_\theta$  model at a  $Re_L = 13 \times 10^5$ .

As can be observed the turbulence found in the lower section of the car is highly reduced, as well as the high velocity gradients that were seen with the original configuration.

As can be observed, once the skirt zone ends, the rounded end shows a highly turbulent wake and a low speed zone. This zone could be further improved by changing the ending geometry.

The second geometry changed the shape of this rounded end as shown in figure 5.9. As already stated, this change tries to fill this low speed region in order to reduce the drag seen by the car.

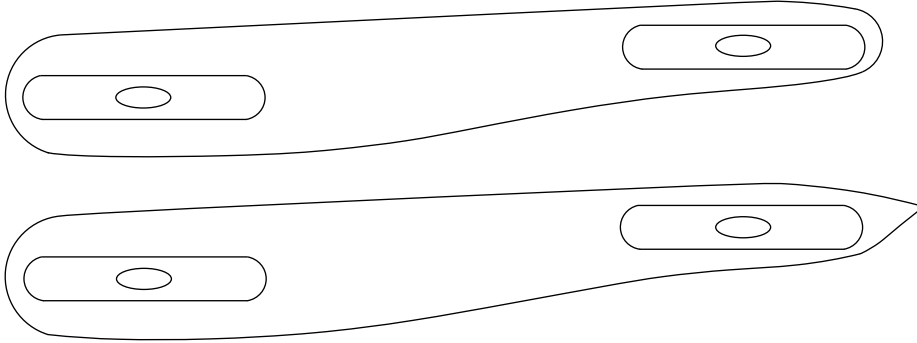


Figure 5.9: Skirt comparison between the first and second performance modifications.

The obtained drag coefficients for the still and moving floors are shown in table 5.3.

<b>3D Model</b>	<b>Condition</b>	$c_D$	<b>Viscous <math>c_D</math></b>
Original	Still	0.166	0.022
Original	Moving	0.146	0.036
2 <sup>nd</sup> Modification	Still	0.113	0.023
2 <sup>nd</sup> Modification	Moving	0.092	0.022

Table 5.3: Drag coefficient comparison between Electra and the second performance modification at still and moving road conditions. Simulations performed with  $\gamma Re_\theta$  model and a  $Re_L = 13 \times 10^5$ .

A drag reduction of 31.1% and 36.5% is found for the still and moving road conditions respectively. Figures 5.10, 5.11, 5.12 and 5.13 show a comparison between the first and second modifications.

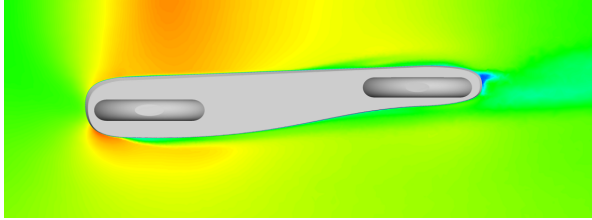
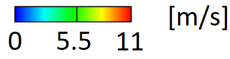


Figure 5.10: Velocity magnitude contour plot at a  $x = 0.15$  m  $y$ - $z$  plane. Simulation performed with the first performance modification at moving road conditions using the  $\gamma Re_\theta$  model at a  $Re_L = 13 \times 10^5$ .

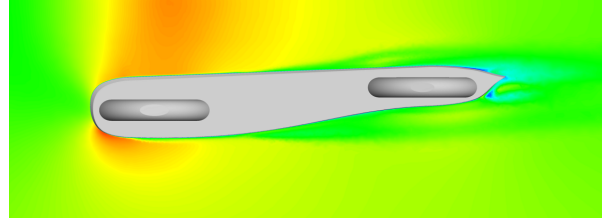


Figure 5.11: Velocity magnitude contour plot at a  $x = 0.15$  m  $y$ - $z$  plane. Simulation performed with the second performance modification at moving road conditions using the  $\gamma Re_\theta$  model at a  $Re_L = 13 \times 10^5$ .

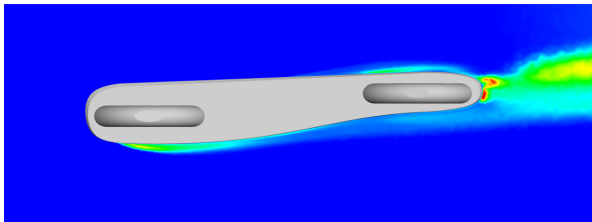
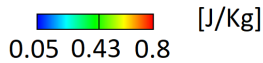


Figure 5.12: Turbulent kinetic energy contour plot at a  $x = 0.15$  m  $y$ - $z$  plane. Simulation performed with the first performance modification at moving road conditions using the  $\gamma Re_\theta$  model at a  $Re_L = 13 \times 10^5$ .

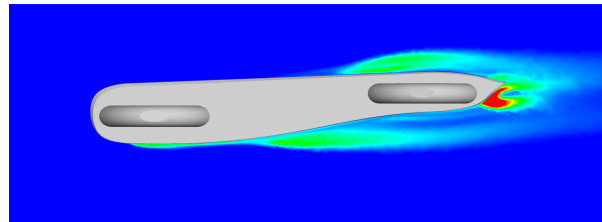
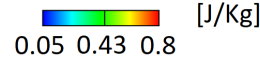


Figure 5.13: Turbulent kinetic energy contour plot at a  $x = 0.15$  m  $y$ - $z$  plane. Simulation performed with the second performance modification at moving road conditions using the  $\gamma Re_\theta$  model at a  $Re_L = 13 \times 10^5$ .

As can be observed the low speed region at the end of the wheel fairing has been reduced, however this is not the case of the turbulent kinetic energy that presents a much energetic end. This high energy end triggers turbulence upstream. This turbulent region could be further improved.

The third modification tries to improve this rear end geometry by elongating the skirt. This geometry is shown in figures 5.14 and 5.15.

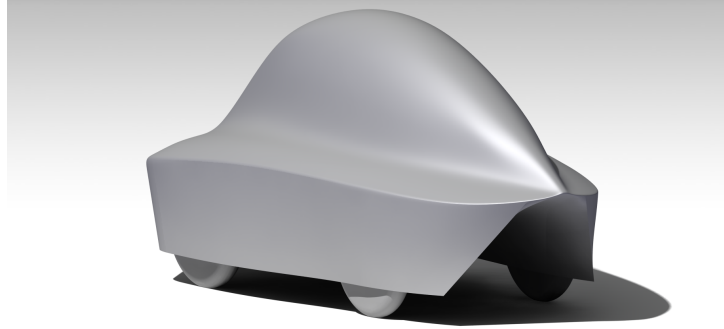


Figure 5.14: 3D model of the third modification based on performance.

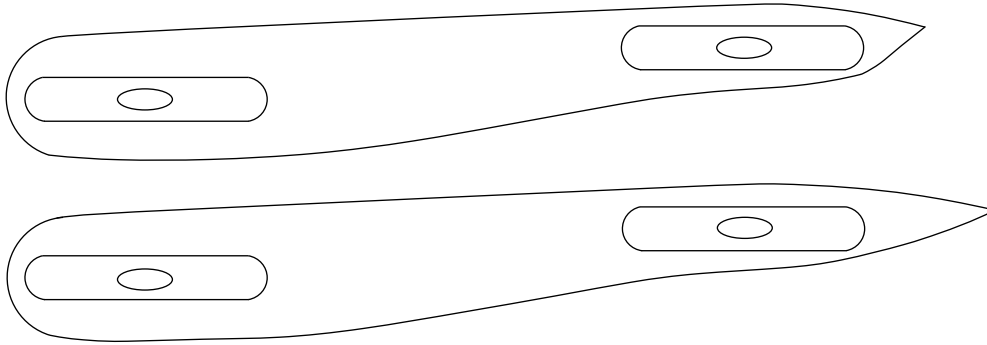


Figure 5.15: Skirt comparison between the second and third performance modifications.

As for the other geometries, this modification was tested with still and moving road conditions. The obtained drag coefficients are compared to the original geometry in table 5.4.

<b>3D Model</b>	<b>Condition</b>	$c_D$	<b>Viscous <math>c_D</math></b>
Original	Still	0.166	0.022
Original	Moving	0.146	0.036
3 <sup>rd</sup> Modification	Still	0.104	0.023
3 <sup>rd</sup> Modification	Moving	0.089	0.024

Table 5.4: Drag coefficient comparison between Electra and the third performance modification at still and moving road conditions. Simulations performed with  $\gamma Re_\theta$  model and a  $Re_L = 13 \times 10^5$ .

This time, a decrease of 37.6% and 38% is found for the still and moving road conditions

respectively. Figures 5.16, 5.17, 5.18 and 5.19 show some of the flow characteristics of this modification.

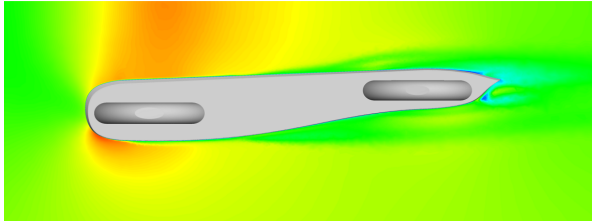
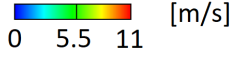


Figure 5.16: Velocity magnitude contour plot at a  $x = 0.15$  m  $y-z$  plane. Simulation performed with the second performance modification at moving road conditions using the  $\gamma Re_\theta$  model at a  $Re_L = 13 \times 10^5$ .

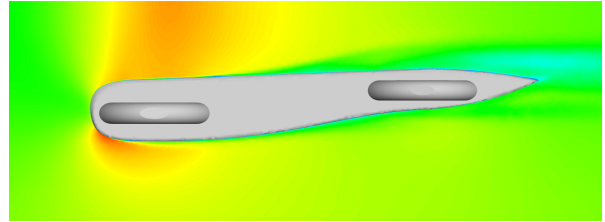
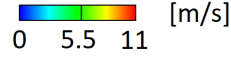


Figure 5.17: Velocity magnitude contour plot at a  $x = 0.15$  m  $y-z$  plane. Simulation performed with the third performance modification at moving road conditions using the  $\gamma Re_\theta$  model at a  $Re_L = 13 \times 10^5$ .

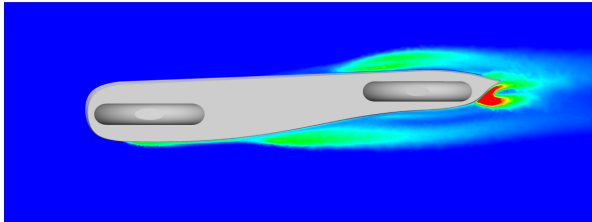
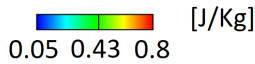


Figure 5.18: Turbulent kinetic energy contour plot at a  $x = 0.15$  m  $y-z$  plane. Simulation performed with the second performance modification at moving road conditions using the  $\gamma Re_\theta$  model at a  $Re_L = 13 \times 10^5$ .

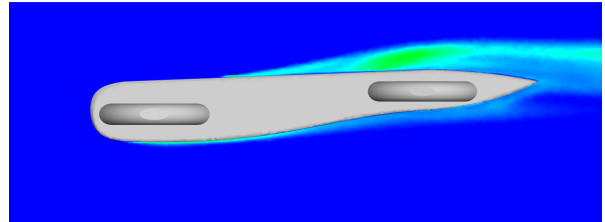
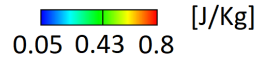


Figure 5.19: Turbulent kinetic energy contour plot at a  $x = 0.15$  m  $y-z$  plane. Simulation performed with the third performance modification at moving road conditions using the  $\gamma Re_\theta$  model at a  $Re_L = 13 \times 10^5$ .

It is possible to observe how the high turbulent kinetic energy was completely eliminated. Due to the absence of this high energetic region, the turbulent kinetic energy has been drastically reduced on the outer side of the skirt. This uniformity is also translated in terms of velocity magnitude that sees now an attached flow until reaching the rear end of the skirt. Due to the much elongated skirt tail, the tunnel effect on the lower side of

the car extends further downstream. This coupled with the fact that the central part of the car rise when reaching the tail causes an expanding cross section area that lowers the pressure at the car end. This decrease of the pressure is the cause of the slight separation of the boundary layer and increase in turbulent kinetic energy at the inner side of the skirt. This effect could be minimize by changing the inner geometry of the skirt, maintaining a more constant tunnel cross sectional area. In order to better understand the diffuser phenomenon, figures 5.20, and 5.21 show the path of the flow through a streamline plot.

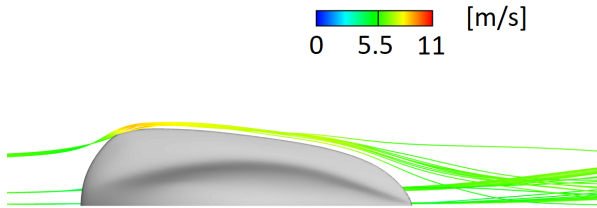


Figure 5.20: Flow streamlines over the third performance modification. Streamlines coloured by velocity magnitude. Simulation performed with moving road conditions using the  $\gamma Re_\theta$  model at a  $Re_L = 13 \times 10^5$ .

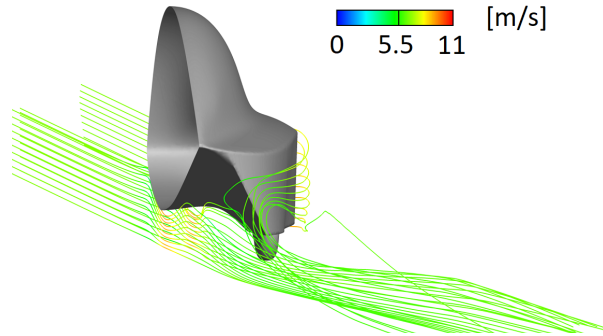


Figure 5.21: Flow streamlines over the third performance modification. Streamlines coloured by velocity magnitude. Simulation performed with moving road conditions using the  $\gamma Re_\theta$  model at a  $Re_L = 13 \times 10^5$ .

As it can be seen in figures 5.20 and 5.21, the lower tunnel of the car expands when reaching the car end. As observed this expansion causes the separation of the boundary layer, as the skirt does not allow the entry of any external feeding source. This separation creates a void that once the wheel fairing ends is filled by the flow coming from the external side of the skirt, causing the appearance of a vortex as shown in figure 5.21.

## 5.2 New concept

In order to take advantage of the new regulations that the new car will be subjected to, the Uliège's Shell Eco-marathon team is trying to restart the project from zero using its large experience in this competition. Due to some mechanical challenges that presented Electra, a new concept based on a platform type chassis is being studied. This kind of chassis allows to have a robust full operative mechanical frame, simplifying the integration of other parts and systems. This new idea would completely change the new car aerodynamics, as the presence of a lower section tunnel will not longer be possible. This section will try to observe the effect that a completely closed car floor would have on Electra in order to understand its new behaviours.

In order to perform a first study, the front of Electra was closed and the lower part of the tail was modified in order to be able to introduce a flat floor (figures 5.22 and 5.23). The tail modification tries to smoothly reduce its width, as it was made with the skirt rear end in the Improving performance section, in order to avoid the presence of detached flow or other undesired flow structures. This rear end technique is commonly known as boat trailing.

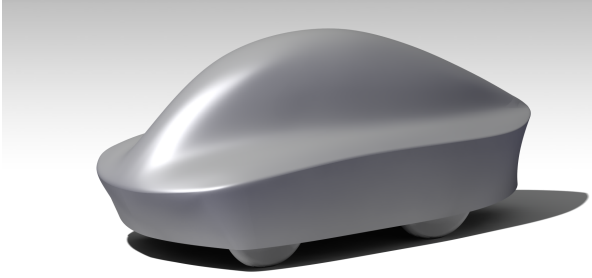


Figure 5.22: 3D model of the first modification based on new concept.

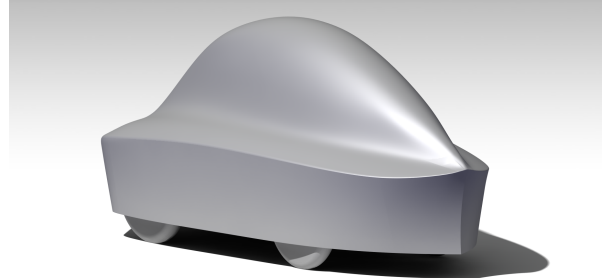


Figure 5.23: 3D model of the first modification based on new concept.

The obtained drag coefficients are shown in table 5.5.

3D Model	Condition	$c_D$	Viscous $c_D$
Original	Still	0.166	0.022
Original	Moving	0.146	0.036
1 <sup>st</sup> Modification	Still	0.164	0.023
1 <sup>st</sup> Modification	Moving	0.133	0.022

Table 5.5: Drag coefficient comparison between Electra and the first new concept modification at still and moving road conditions. Simulations performed with  $\gamma Re_\theta$  model and a  $Re_L = 13 \times 10^5$ .

This time, a slight decrease in drag is found, being this of 1.4% for the still road conditions and of 7.7% for the moving road condition. Even though this car presents better aerodynamics than the original Electra, one must not forget that it does represent a significant increase in drag with respect to the performance-based modification, whose drag presented a 38% drag decrease instead of 7.7%. Figures 5.24, 5.25, 5.26 and 5.27 show the general properties of the flow around this modification.

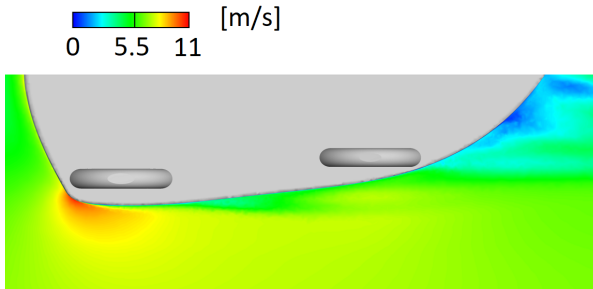


Figure 5.24: Velocity magnitude contour plot at a  $x = 0.15$  m  $y$ - $z$  plane. Simulation performed with the first new concept modification at moving road conditions using the  $\gamma Re_\theta$  model at a  $Re_L = 13 \times 10^5$ .

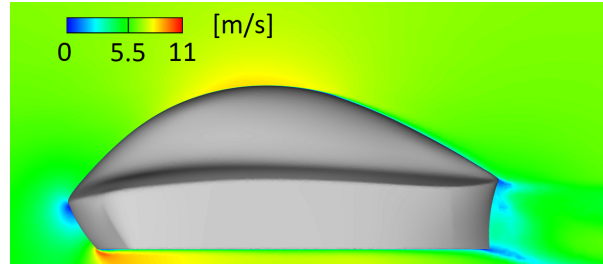


Figure 5.25: Velocity magnitude contour plot at the car middle plane. Simulation performed with the first new concept modification at moving road conditions using the  $\gamma Re_\theta$  model at a  $Re_L = 13 \times 10^5$ .

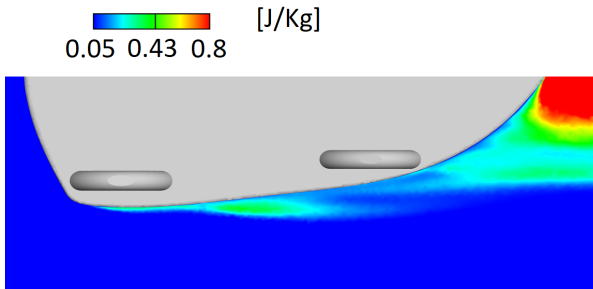


Figure 5.26: Turbulent kinetic energy contour plot at a  $x = 0.15$  m  $y - z$  plane. Simulation performed with first new concept modification at moving road conditions using the  $\gamma Re_\theta$  model at a  $Re_L = 13 \times 10^5$ .

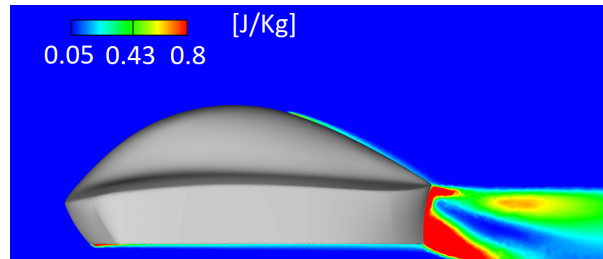


Figure 5.27: Turbulent kinetic energy contour plot at middle car plane. Simulation performed with first new concept modification at moving road conditions using the  $\gamma Re_\theta$  model at a  $Re_L = 13 \times 10^5$ .

Due to the absence of the lower tunnel cavity, the blockage on the lower side of the car is more prominent than in the other cases. The flow around the car side sees some gradients in speed that can also be observed in the turbulent kinetic energy plot. Even making use of the tail boating technique, the flow is not capable of remaining attached at the rear of the vehicle. It is also possible to observe how the hard edge present at the front part of the vehicle presents a high kinetic energy point. This could be avoided by rounding all lower edges.

The next modification concentrates in decreasing the rear surface area by performing a lower side diffuser. This diffuser will help distributing some of that separation-induced



suction to the vertical axis, reducing its direct effect on drag. Also all lower edges are rounded in order to obtain a smooth flow and avoid triggering high energetic turbulence. The modified geometry is shown in figures 5.28 and 5.29.

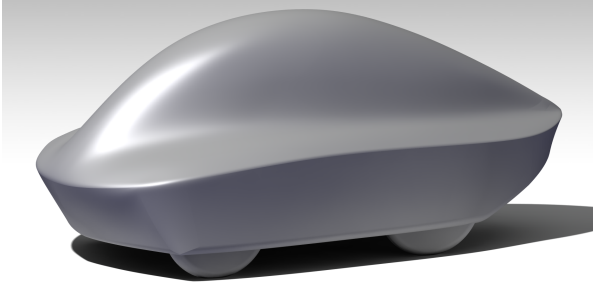


Figure 5.28: 3D model of the second modification based on new concept.

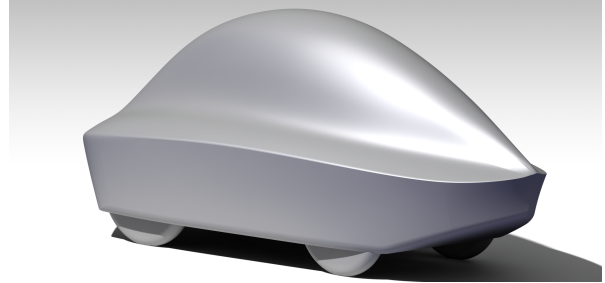


Figure 5.29: 3D model of the second modification based on new concept.

Promising results were obtained with this geometry as shown in table 5.6.

3D Model	Condition	$c_D$	Viscous $c_D$
Original	Still	0.166	0.022
Original	Moving	0.146	0.036
2 <sup>nd</sup> Modification	Still	0.132	0.021
2 <sup>nd</sup> Modification	Moving	0.111	0.022

Table 5.6: Drag coefficient comparison between Electra and the second new concept modification at still and moving road conditions. Simulations performed with  $\gamma Re_\theta$  model and a  $Re_L = 13 \times 10^5$ .

A total drag reduction of 20.4% is found for the still road conditions and 22.7% for the moving conditions. Even though it stays a lower improvement than the one found within section 5.1, the improvement of this model over the previous one shows the high optimization potential of this new concept. Figures 5.30, 5.31, 5.32 and 5.33 show some of the flow properties of this geometry.

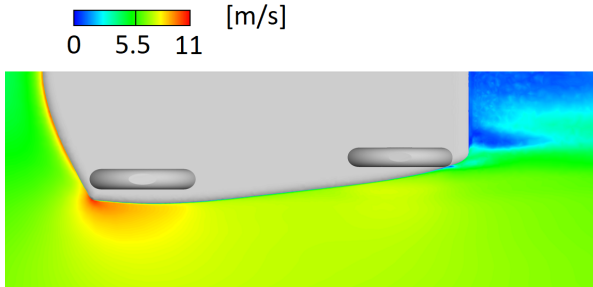


Figure 5.30: Velocity magnitude contour plot at a  $x = 0.15$  m  $y$ - $z$  plane. Simulation performed with the second new concept modification at moving road conditions using the  $\gamma Re_\theta$  model at a  $Re_L = 13 \times 10^5$ .

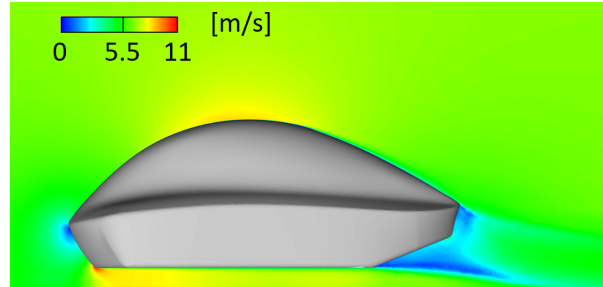


Figure 5.31: Velocity magnitude contour plot at the car middle plane. Simulation performed with the second new concept modification at moving road conditions using the  $\gamma Re_\theta$  model at a  $Re_L = 13 \times 10^5$ .

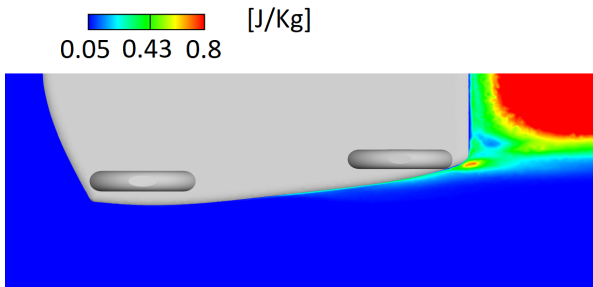


Figure 5.32: Turbulent kinetic energy contour plot at a  $x = 0.15$  m  $y - z$  plane. Simulation performed with second new concept modification at moving road conditions using the  $\gamma Re_\theta$  model at a  $Re_L = 13 \times 10^5$ .

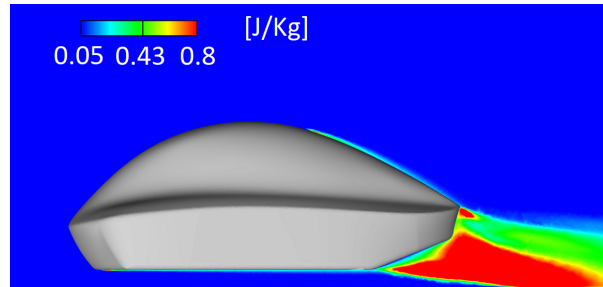


Figure 5.33: Turbulent kinetic energy contour plot at middle car plane. Simulation performed with second new concept modification at moving road conditions using the  $\gamma Re_\theta$  model at a  $Re_L = 13 \times 10^5$ .

As it was expected, the lower high energy kinetic energy point has completely disappeared from the front of the car. The diffuser induced the separation of the boundary layer creating a low speed zone behind the car, however this time this is desired. As it was already explained in the third performance modification, this separation has the same effect, as the low pressure that this expansion induces attracts the flow of the vehicle side and induces similar vortices as the ones shown on the other modification. This suction helps the lateral flow to remain more attached to the car surface (figures 5.34 and 5.35). However, it is possible to observe how this diffuser zone triggers a high energetic turbulent zone. The reduction of this phenomenon could be of interest for future works.

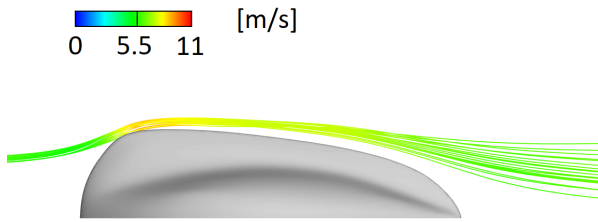


Figure 5.34: Turbulent kinetic energy contour plot at a  $x = 0.15$  m  $y - z$  plane. Simulation performed with second new concept modification at moving road conditions using the  $\gamma Re_\theta$  model at a  $Re_L = 13 \times 10^5$ .

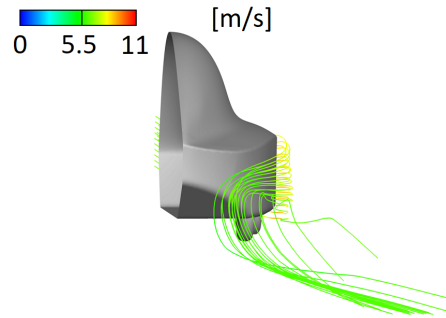


Figure 5.35: Turbulent kinetic energy contour plot at middle car plane. Simulation performed with second new concept modification at moving road conditions using the  $\gamma Re_\theta$  model at a  $Re_L = 13 \times 10^5$ .

# Chapter 6

## Conclusion

### 6.1 Results and critical overview

The objective of this thesis was to study the aerodynamic properties of Electra through numerical and experimental analysis.

In order to minimize the error introduced by the turbulence modelling of the RANS equations, multiple turbulence models were studied. The tested models were the wall function versions of the realizable  $k - \varepsilon$  and the  $k - \omega$  SST models, the low Reynolds version of the  $k - \omega$  SST model and the  $\gamma Re_\theta$  transition model. Taking the reference case<sup>1</sup>, it was possible to observe how the use of different turbulence models yielded very different results, obtaining differences of up to 26% in drag.

After thorough analysis of all parameters playing a role in the numerical simulations, the quality of the chosen set-up was validated through the study of the Ahmed body, a widespread benchmark geometry for CFD simulations. This test allowed to observe how the obtained results compare to other results found in the scientific community.

An extensive study of the wind tunnel set-up was also carried out, in which intermediate results allowed to successfully modify it and identify the flow characteristics in front of the car model. This flow characterization was of major importance due to its impact on the final conclusions.

In order to reduce simulation cost, the symmetry and steadiness of the studied case were verified through the use of a full domain URANS simulation, in which neither the symmetry nor the steadiness of the problem was taken into account. Both, experimental and numerical studies allowed to verify the steadiness and symmetry of the problem, allowing to confidently use half-domain RANS simulations.

In order to validate the numerical model of Electra, a comparison between simulations with still road conditions and wind tunnel data was accomplished. Wind tunnel force and

---

<sup>1</sup>Zero angle of yaw at the reference length based Reynolds number ( $Re_{L_{ref}}$ )

pressure measurements were compared to numerical results, being possible to carefully judge each of the turbulence models as well as an interesting comparison between the low Reynolds and wall function models. This comparison showed that even though wall-function models allow for faster and less CPU-intensive simulations, they could show some deficiencies when large separation regions are present in the studied case. After a deep analysis of the obtained results, the transition  $\gamma Re_\theta$  model was chosen as the most adequate for the studied case.

Once the numerical simulations were experimentally validated, it was possible to make use of the CFD advantages and push the Electra study even further, by taking closer to real life conditions into consideration. The first study consisted in taking moving floor conditions into account for zero angle of yaw as well as crosswind cases. The importance of the ground effect on close-to-ground bodies could be observed, noticing an important change in Electra's aerodynamic properties. Moving conditions showed a 12% reduction in drag when compared to still road conditions. Thanks to an extensive CFD analysis, it was also possible to visualize the flow characteristics around the car, finding potentially optimizable regions, information that was exploited while performing the aerodynamic modifications.

All these CFD simulations presented an idealized and simplified version of the real car. In order to get closer to reality, the effect of the flow inside the wheel well was estimated by taking into account the conclusions at which Morelli and Scibor-Rylski arrived, being possible to approximate this effect by using the aerodynamic properties of an exposed wheel. This correction yielded a 3.5% increase over the idealized and simplified model.

Then, the effect of the rear-view mirrors presence was considered. A CFD analysis showed the low aerodynamic performance of these devices, obtaining a  $c_D = 0.51$ . High energy turbulence and low speed regions were found on the wake of the mirror. This correction caused an increase in drag of 8%. Taking both corrections into consideration, the drag coefficient increased from 0.146 to 0.163, making clear the importance of bearing in mind the performed simplifications when judging the performance of a vehicle.

After these corrections, a brief analysis of the effect of the different surface protuberances and imperfections was performed. In this investigation, a practical guide of how to improve the aerodynamic properties of these protuberances was presented.

Once the aerodynamic properties of Electra were understood, it was possible to introduce some modifications. These modifications could be divided into two categories: performance, and new concept modifications.

In the performance modifications, the decrease of Electra's drag was the only objective. It was concluded that the height of the car, as well as closing the gap between the front and rear wheel fairings, could help reducing drag. A deep study of each of the modifications

allowed to enhance the aerodynamic properties arriving to a  $c_D = 0.089$ . This drag coefficient represents a 38% reduction with respect to Electra.

Finally, the aerodynamic effect that the possible introduction of a platform chassis type could have on Electra's aerodynamics was tested. This new chassis would not allow the presence of a tunnel on its lower surface, increasing the frontal area and changing its aerodynamic behaviour. In order to test this change, a first modification was performed, which was further optimized after analysing its aerodynamic properties. The results were satisfactory, obtaining a reduction of 22.7% in drag compared to the original Electra. However this aerodynamic enhancement was lower than the skirt modification tested in the performance modifications section.

## 6.2 Future work

This thesis only represents an introduction to the aerodynamic study of the *A&M Shell Eco Marathon* vehicle, opening multiple lines of investigation for future academic years. Some of these are presented hereafter.

### 6.2.1 Numerical simulations

- The numerical study could be improved by introducing the use of detached eddy simulation (DES), a hybrid model that models the wall regions as a RANS model, but treats the rest of the flow as a large eddy simulation (LES), being possible to capture finer details in the flow structures around the car.
- All modifications in this thesis were carried out by observation of results, however, it would also be interesting to perform a parametrization of the vehicle in order to obtain a more thorough optimization routine of the car aerodynamics. This parametrization would allow to accurately vary different shape parameters until arriving to an optimum solution.
- The crosswind case study could be further developed by adding more angles of incidence into consideration, as well as studying the dynamic stability of the car under unsteady free-stream conditions. This would allow to understand the flow properties around Electra in multiple situations such as overtaking or cornering.
- A deeper analysis of the surface irregularities could be done. A CFD analysis of the effect in transition from laminar to turbulent would allow to obtain a better understanding of the effect of these elements on the aerodynamic properties of the car.

### 6.2.2 Experimental tests

- Due to the sensor mounting, car and plate lift are measured at the same time, obtaining spurious results for lift and moment measurements. This set-up could be improved by trying new configurations, such as an sting mounted sensor.
- The pressure map over the car surface could be improved in order to obtain a better understanding of the 3D flow around the vehicle, and eventually being able to estimate the lift coefficient by integration of these pressures over the car surface.
- The study of the flow through visualization techniques would allow a better understanding of the vehicle aerodynamics. Smoke visualization or PIV<sup>2</sup> would help understanding the 3D structures present around the vehicle, while wall tracing method with pigment oil would help observing multiple phenomena such as laminar to turbulent transition or surface flow patterns.
- Experimental validation of the new prototypes would contribute to a better understanding of the aerodynamic properties of the vehicle, as well as a better understanding of the influence of each modification.

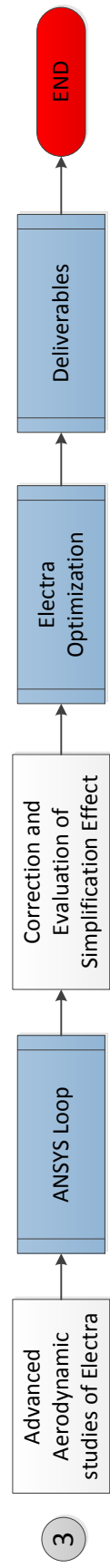
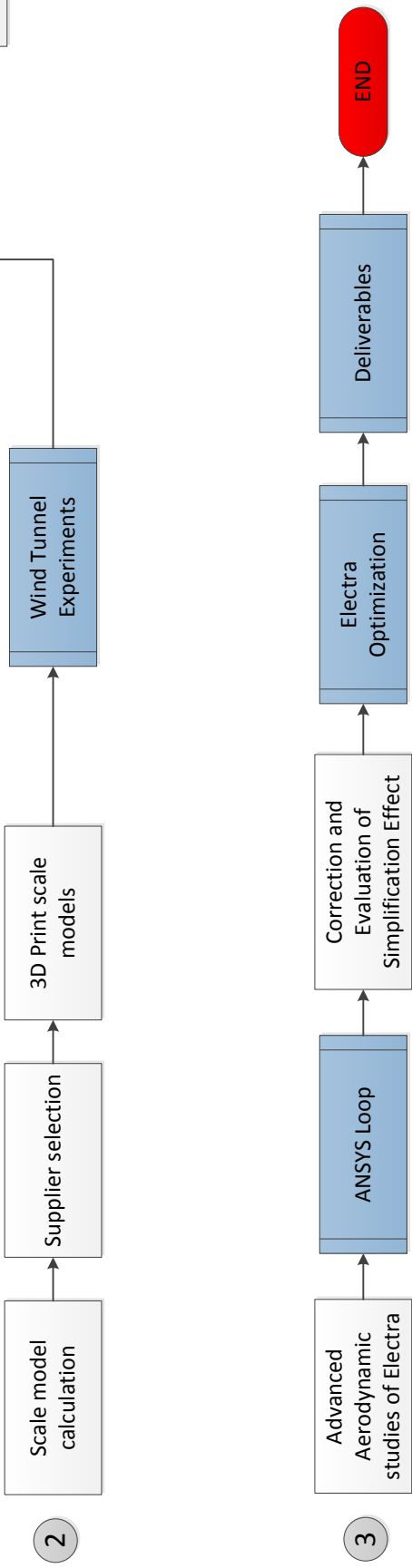
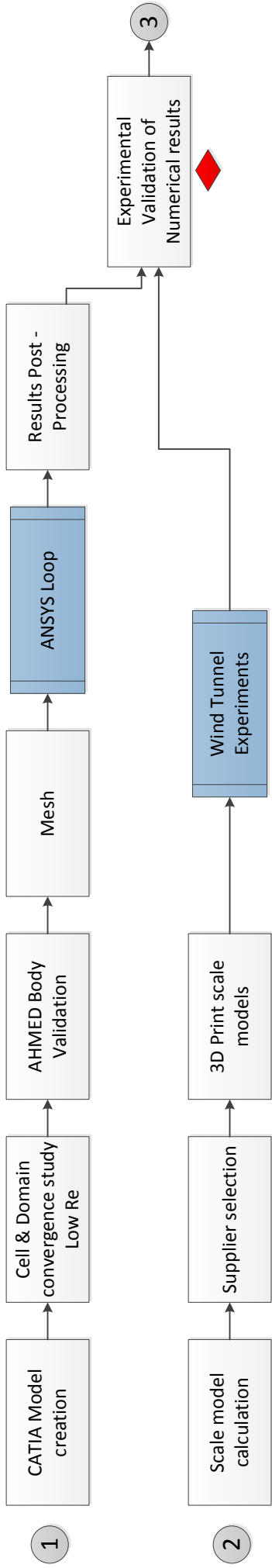
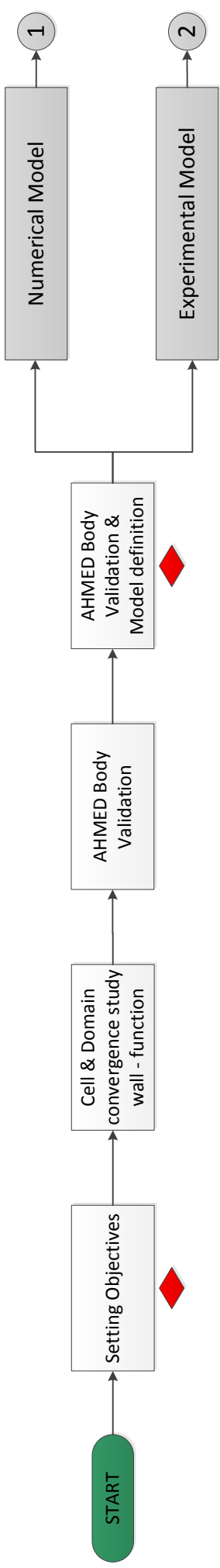
As can be seen, this thesis opened many investigation lines that could complete this aerodynamic study, as well as improving the car performance.

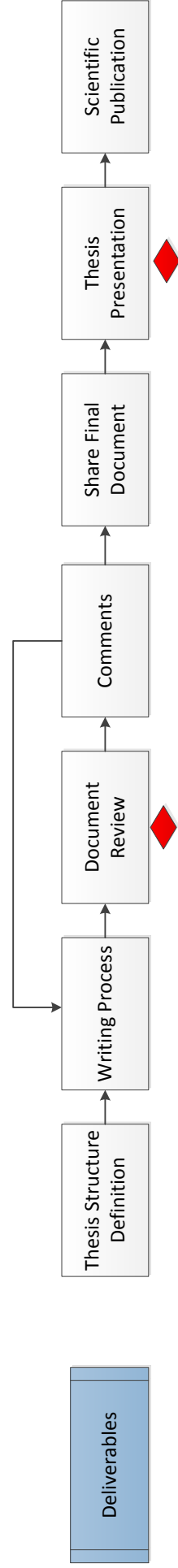
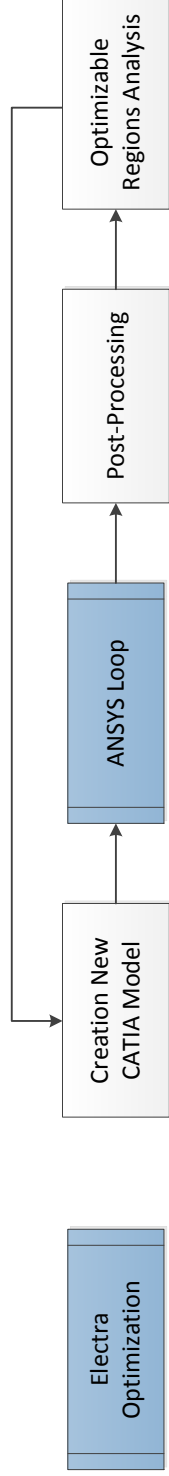
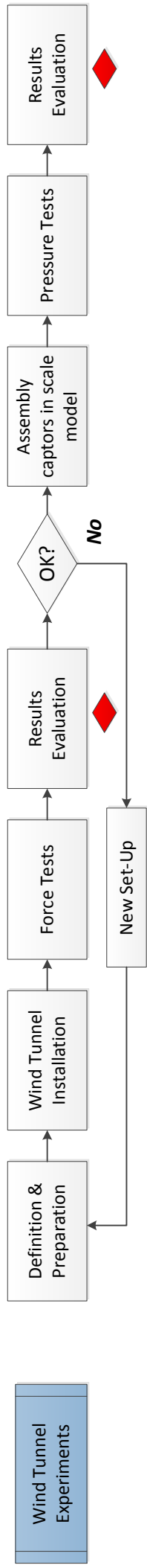
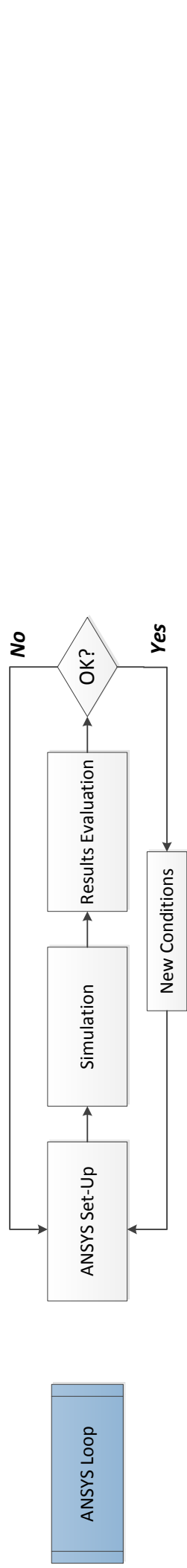
---

<sup>2</sup>Particle image velocimetry

# Annex I: Thesis workflow diagram







# Bibliography

- [1] C. Hirsch. *Numerical Computation of Internal and External Flows*. 2007.
- [2] G.Ramm, S.R Ahmed, and G.Faltin. *Some Salient Features Of The Time-Averaged Ground Vehicle Wake*. Detroit: Society of Automotive Engineers. 1984.
- [3] Liège Université. *The University of Liège Wind Tunnel Facility: Technical Description*. 2009.
- [4] W.H. Hucho. *Aerodynamics of Road Vehicles*. 1990.
- [5] W. Klemperer. Luftwiderstandsuntersuchungen an automodellen. *Zeitschrift für Flugtechnik und Motorluftschiffahrt*, 13:201 – 206, 1922.
- [6] W.H. Hucho, L.J. Janssen, and H.J. Emmelmann. The optimization of body details - a method for reducing the aerodynamic drag of road vehicles. *SAE Paper*, 1976.
- [7] A. Morelli, L. Fioravanti, and A. Cogotti. The body shape of minimum drag. *SAE Paper*, 1976.
- [8] A. Morelli. Low drag bodies moving in proximity of the ground. *Aerodynamics of Transportation*, (241 - 248), 1979.
- [9] J. Mohsen. Laminar separation bubble: Its structure, dynamics and control. 2011.
- [10] H.P. Horton. Laminar separation bubbles in two and three dimensional incompressible flow. 1968.
- [11] A.J. Scibor-Rylski. *Road Vehicle Aerodynamics, 2nd edition*. Pentech Press, London. 1984.
- [12] S.F. Hoerner. Fluid-dynamic drag: Theoretical, experimental and statistical information. 1965.
- [13] M. R. Ahmed, T. Takasaki, and Y. Kohama. Aerodynamics of a NACA4412 Airfoil in Ground Effect. *AIAA*, 45(1), 2007.
- [14] NASA. Global climate change: Vital signs of the planet. URL:<https://climate.nasa.gov/evidence/> (Visited on: 07/04/2018).

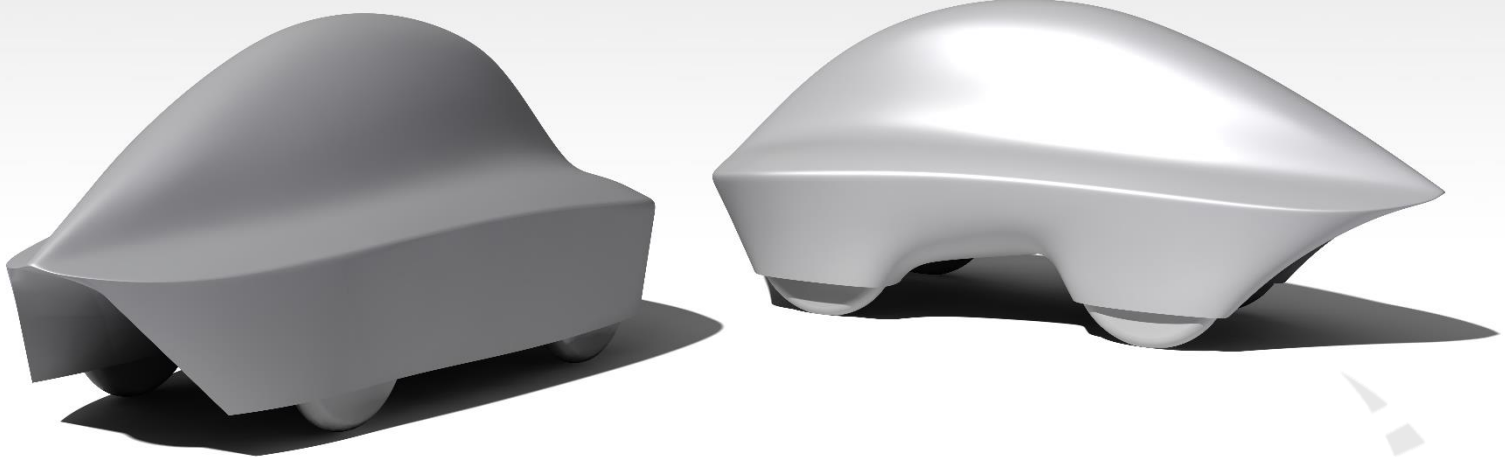
- [15] A. Adler et al. *Climate change 2014: Mitigation of climate change*, 2014.
- [16] A. Morelli. *Aerodynamic actions on an automobile wheel. Paper 5; Proc. 1st Symposium of Road Vehicle Aerodynamics, London*. 1969.
- [17] P.A. Durbin and B.A Pettersson-Reif. *Statistical Theory and Modeling for Turbulent Flows*. 2011.
- [18] W.P Jones and B.E Launder. A new k-epsilon eddy viscosity model for high reynolds number turbulent flows. *Computer and Fluids*, 24(3):227 – 238, 1995.
- [19] T.H. Shih, W.W. Liou, A. Shabbir, Z. Yang, and J. Zhu. The prediction of laminarization with a two-equation model of turbulence. *International Journal of Heat and Mass Transfer*, 15(2):301 – 314, 1972.
- [20] Marco Lanfrit. *Best practice guidelines for handling automotive external aerodynamics with fluent*, 2005.
- [21] Inc. ANSYS. *Ansys fluent 19.0 user’s guide*. 2018.
- [22] F.R. Menter, M. Kuntz, and R. Langtry. Ten years of industrial experience with the sst turbulence model. 2003.
- [23] Inc ANSYS. *ANSYS 18.1 User guide: 4.7.1 Transport Equations for the Transition SST Model*. Canonsburg, Pennsylvania, United States, 2017.
- [24] Robin B. Langtry; Florian R. Menter. Correlation-Based Transition Modeling for Unstructured Parallelized Computational Fluid Dynamics Codes. *AIAA Journal*, 47(12), 2009.
- [25] Karthik Duraisamy Aniket C. Aranake, Vinod K. Lakshminarayan. *Assessment of Transition Model and CFD Methodology for Wind Turbine Flows* . 2012.
- [26] K. Suluksna and E. Juntasaror. Assessment of intermittency transport equations for modeling transition in boundary layers subjected to freestream turbulence.
- [27] F.J. Kececy. Coupling momentum and continuity increases cfd robustness. 2:49–51, 01 2008.
- [28] V.E. Terrapon. Aero0030-1 - computational fluid dynamics. lecture 8. pages 31–36, 2017.
- [29] Y. Liu and A. Moser. Numerical modeling of airflow over the ahmed body. *Proceedings of the 11th Annual Conference of the CFD Society of Canada*, 2003.
- [30] M. Corallo, J. Sheridan, and M.C. Thompson. Effect of aspect ratio on the near-wake flow structure of an ahmed body. *Journal of Wind Engineering and Industrial Aerodynamics*, 147:95 – 103, 2015.

- [31] B. Conan., J. Anthoine, and Planquart. Experimental aerodynamic study of a car-type bluff body. *Experiments in Fluids*, 50:1273 – 1284, 2011.
- [32] X.W. Wang, Y. Zhou, and Y.F. Pin. Turbulent near wake of an ahmed vehicle model. *Experiments in Fluids*, 95, 2013.
- [33] A. Brunn, E. Wassen, D. Sperber, W. Nitsche, and F. Thiele. Experimental aerodynamic study of a car-type bluff body. *Notes on Numerical Fluid Mechanics and Multidisciplinary Design*, 95:247 – 259, 2007.
- [34] V.E. Terrapon and T. Andrienne. Aero0001-1 - aerodynamics. aerodynamics project statement. page 9, 2018.
- [35] J.M. Lucas, O. Cadot, V. Herbert, S. Parpais, and J. Delery. A numerical investigation of the asymmetric wake mode of a squareback ahmed body - effect of a base cavity. 831:675 – 697, 2017.

**Graduation Studies Supervised by**

**Promoter: V.E. Terrapon**

**Jury Members: T. Andrianne, P. Duysinx**



**“Once something  
is a passion, the  
motivation is there”**

**Michael Schumacher**



**Shell  
Eco-marathon®  
EUROPE**